

A comprehensive study on the processing of Co:ZnO ceramics: defect chemistry engineering and grain growth kinetics

R. T. da Silva^a, J. M. Morbec^{b‡}, G. Rahman^{c†}, and H. B. de Carvalho^{d*}

^a *Universidade Federal de Ouro Preto – UFOP, 35400-000 Ouro Preto, MG, Brazil.*

^b *School of Chemical and Physical Sciences, Keele University, Keele ST5 5BG, United Kingdom*

^c *Department of Physics, Quaid-i-Azam University, 45320 Islamabad, Pakistan.*

^d *Universidade Federal de Alfenas - UNIFAL, 37130-000 Alfenas, Brazil.*

Corresponding Authors:

‡ j.morbec@keele.ac.uk

† gulrahman@qau.edu.pk.

* hugo.carvalho@unifal-mg.edu.br.

ABSTRACT: In this report we present a systematic study on the preparation of Co:ZnO ceramics via standard solid-state route from different Co precursors (Co₃O₄, CoO and metallic Co) and atmospheres (O₂ and Ar). Particular emphasis was done on the defect chemistry engineering and on the sintering growth kinetics. First-principles calculations based on density functional theory were employed to determine the formation energy of the main point defects in ZnO and Co:ZnO systems. Based on the theoretical results a set of chemical reactions was proposed. A detailed microstructural characterization was performed in order to determine the degree of Co incorporation into the ZnO lattice. The samples prepared in Ar atmosphere and from metallic Co presents the highest Co solubility limit (lower apparent Co incorporation activation energy) due to the incongruent ZnO decomposition. The determination of the parameters of the sintering growth kinetics reveals that Co₃O₄ is the best sintering additive in order to achieve higher densities in both sintering atmospheres. The results give evidences that the sintering in O₂ is effective in promoting zinc vacancies in the ZnO structure, while the sintering in Ar promotes zinc interstitial defects. Our findings give valuable contribution to the understanding of the preparation of Co-doped ZnO ceramics and the sintering growth kinetics, what would allow to improve the state of the art on the processing of the material at both bulk and nanometric scales.

KEYWORDS: Multifunctionality, Zinc oxide, Defect engineering, Growth kinetics.

1 INTRODUCTION

ZnO is one of the truly multifunctional material due to its extensive and interesting physical and electrochemical properties. The optimization of the ZnO properties for a particular application, the ZnO functionalization, takes place mainly via defect engineering, by doping or even by the introduction of defects into the structural lattice in a well-controlled manner [1]. Specifically, transition metal (TM) doped ZnO has been explored as a dilute magnetic semiconductor (DMS)

to be used as spin injection layer into spintronic semiconductor devices. Spintronics is attracting considerable attention in the last decades by potentially implement new data storage and quantum computing devices [2-5]. However, the obtained results, regarding the nature of the usual observed room temperature ferromagnetism (RTFM), are very controversial. In addition to the trivial extrinsic origins of the RTFM that result from the ferromagnetic secondary phases, the main theoretical models that are currently available for describing the origins and properties of the observed RTFM are all linked to structural defects [6-11]. This linkage explains why the ferromagnetic properties are rarely reproducible. Before elucidating the mechanisms of intrinsic FM, the measured magnetic hysteresis loops must be classified as intrinsic or extrinsic. Contamination by magnetic elements [12], measurement errors [13] and segregated secondary phases [14, 15] can all cause ferromagnetic signals.

From the theoretical point of view, different models have been proposed to explain the usual observed RTFM in DMS's. Here, the main accepted model for insulating systems is the bound magnetic polaron (BMP) theory [16] where the ferromagnetic exchange coupling among the TM doping elements is mediated by shallow donor electrons. These defects form bound magnetic polarons, which overlap to create a spin-split impurity band. For the particular case of the Co-doped ZnO, the Co^{2+} ions can hybridize effectively with shallow-donor impurity bands in ZnO because the states related to the complex $\text{Co}^+ (\text{Co}^{2+} + e^-_{\text{donor}})$ are also of shallow-donor character [17]. Considering the question about the nature of the necessary shallow-donor defect, several experimental reports argue that the RTFM in the TM-doped ZnO system, explained in terms of the BMP model, is associated to oxygen vacancies (V_{O}) [18-21]. In fact, the defect state related to V_{O} in the wurtzite ZnO structure has a donor character, however it is a deep-donor state [22, 23]. Although states of deeper-donors can hybridize to magnetic dopants, their smaller Bohr radius would require relatively higher dopant and defect concentrations to achieve a necessary spatial overlapping, however at such short-range antiferromagnetic superexchange interactions would take place. Instead, the most promising shallow-donor defect in the ZnO structure is the zinc

interstitials (Zn_i) [22, 24]. From the experimental point of view, there are a growing number of reports in the literature giving clear evidences of the relation between the observed RTFM and defects at the zinc sites [11, 25-27].

Nanostructured TM-doped ZnO has also been considered for biomedical applications due to its low-toxicity in bioimaging and drug delivery systems [28], and as antibacterial agent [29]. However, it is a well-known fact that the incorporation of dopant at nanoscale is a very difficult task [30], even for highly soluble dopants, the incorporation of a significant amount of dopant atoms during synthesis is not straightforward. Even when dopants are incorporated, their concentration is typically an order of magnitude less than in the growth solution [31]. These results have led to theoretical efforts to understand the mechanisms that control the doping process [32]. An interesting strategy to overcome this problem is the top-down approach, where the preparation of nanostructured materials is performed via, for example, mechanical milling of bulk materials [33, 34]. At the bulk scale a homogeneous distribution of the dopants can be achieved before the subsequent reduction in the dimensionality. The grinding would lead also to surfaces of the nanoparticles with a high degree of defects, that can enhance particular desired properties, like the necessary visible fluorescence in bioimaging [35, 36].

Therefore, the study and determination of the phase diagram of ZnO and TM oxides is important to assure the synthesis of TM-doped ZnO ($Zn_{1-x}TM_xO$) magnetic semiconductor. Besides, the controlling of the presence and the density of specific point defects is necessary in order to tune the desired properties and functionalities in the development of the aforementioned technologies. Also, the knowledge of the sintering kinetics parameters and its correlations are fundamental in the processing of bulk material, and in its eventual reduction of dimensionality down to the nanoscale. In this context, the aim of the present report is to give further contribution in the understanding of the Co incorporation process into the wurtzite ZnO (*w*-ZnO) lattice, and how it can affect some important properties of the material, such as their sintering kinetics. Here Co:ZnO samples were prepared from different Co precursor (Co_3O_4 , CoO, and metallic Co) in

different sintering atmosphere (oxygen and argon). First-principles calculations were performed to give support to the defect chemical analysis and insight into the mechanisms of the Co incorporation in the ZnO. A detailed structural characterization was employed by conjugating several different techniques to determine the structures of the samples, the Co apparent incorporation activation energy, and the grain growth kinetic parameters.

2 EXPERIMENTAL AND THEORETICAL METHODS

Polycrystalline Co:ZnO samples were prepared via solid-state reaction method. Stoichiometric amounts of high purity powders of ZnO (Alfa Aesar 99.99% purity), and different Co precursor sources: Co₃O₄ (Alfa Aesar, 99.7% purity), CoO (Sigma Aldrich 99.99% purity), metallic Co (Sigma Aldrich, 99.9% purity). The samples prepared with Co₃O₄, CoO, and metallic Co was labeled as Co₃O₄:ZnO, CoO:ZnO, and *m*Co:ZnO, respectively. All the samples were prepared with Co atomic concentration of 8 at.% in respect of the cationic sites of a potential single phase Zn_{1-x}Co_xO (Co-doped *w*-ZnO), it means $x = N_{\text{Co}} / (N_{\text{Co}} + N_{\text{Zn}}) = 0.08$ (N is the number of atoms). The precursors were manually mixed and ground in a planetary ball mill (Retsch PM 100) using tungsten carbide jar and spheres at rotation speed of 500 RPM for 4 h, the ratio between the masses of the spheres and the powder was kept at 13:1. Isopropyl alcohol was also added to the samples in order to optimize a grinding process. The resulting powder was dried and sintered in oxygen (O₂) or argon (Ar) atmospheres in the temperature range of 600 to 1200 °C for 4 h with heat/cooling rate of 10 °C/min. Flowchart in Figure 1 illustrates the procedure employed in the preparation of the samples.

The crystal structures of the Co:ZnO powders were investigated by X-ray diffraction (XRD) performed in the range of $2\theta = 15^\circ - 120^\circ$ in steps of 0.02° at 7 s/step using Cu-K α radiation ($\lambda = 1.542 \text{ \AA}$) in a Rigaku Ultima IV diffractometer. The determination of the lattice parameters and the occupation factor over the structure were evaluated using the Rietveld method as implemented by the General Structure Analysis System (GSAS) software package with the graphical user interface EXPGUI [37, 38]. Raman spectroscopy was also used to add information

about the Co doping and the resulting lattice disorder, as well as to analyze the formation of segregated secondary phases. Photoluminescence (PL) measurements were performed in order to directly check the Co incorporation into the *w*-ZnO lattice. Both Raman and PL measurements were carried out at room temperature on a modular spectrometer consisting of an Olympus B-X41 microscope and a Horiba iHR550 monochromator at the backscattered photon detection geometry. A 532 nm B&W Tek solid-state laser was used as source of excitation. The morphology and the grain size distribution of the sintered samples were evaluated via scanning electron microscope (SEM) in a Hitachi S-4800 FEG-SEM.

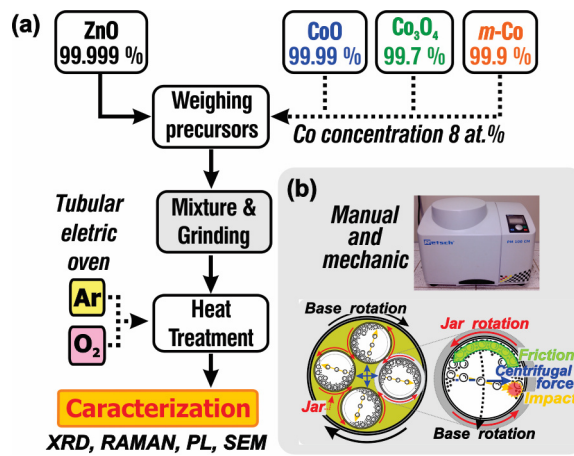


Figure 1. (a) Flowchart of the preparation of the Co:ZnO samples. (b) Schematic representation of the rotating ball milling showing impact milling actions.

The defects formation energies in the Co:ZnO system were also investigated by means of first-principles calculations based on density functional theory (DFT) [39]. We used the Siesta code [40], which employs norm-conserving Troullier–Martins pseudopotentials and linear combinations of atomic orbitals [41]. We used norm-conserving Troullier–Marting pseudopotentials and a double-zet set with polarization functions (DZP) for all atoms with a real-space energy cutoff of 200 Ry. We considered *w*-ZnO cluster with 80 atoms (40 Zn and 40 O), simulated within the supercell approach with a vacuum of ~ 10 Å between the cluster and its image. The dangling bonds at the surface were kept unsaturated and the atoms were allowed to relax to their minimum energy configurations. All atomic positions were fully relaxed until the forces on each atom were smaller than $0.02 \text{ eV } \text{Å}^{-1}$.

3 RESULTS AND DISCUSSION

3.1 First principles calculations and defect chemistry

The defect chemistry is a powerful tool in the understanding of the properties of materials and in their development, especially for ceramics. Nevertheless, it is a difficult task to determine which exact reaction occurs during a specific processing. The case of ZnO is not different. Considering the cobalt doping of the *w*-ZnO lattice using different precursors and different temperatures of sintering and atmospheres, several different possible defect chemical reactions are possible. To get the right direction and reach the right chemical reaction set of equations, some theoretical and experimental considerations have to be taken into account.

Figure 2(a) presents the calculated formation energies (E_f) for the main point defects in *w*-ZnO (most common reported): oxygen vacancy (V_O), zinc interstitial (Zn_i), zinc vacancy (V_{Zn}) [42, 43], for the cobalt incorporation into the *w*-ZnO lattice (Co_{Zn}), and the same point defects in the presence of cobalt already incorporated in the *w*-ZnO (V_O+Co , Zn_i+Co and $V_{Zn}+Co$). Zinc oxide is an unintentional *n*-type semiconductor, and its conductivity was considered for a long time to be due to zinc excess in the non-stoichiometric compound $Zn_{1+\delta}O$, with zinc interstitials (Zn_i) been the dominating lattice defects [44]. However, Zn_i , in spite of been a shallow-donor defect [11, 23], has a relatively high E_f in the pristine *w*-ZnO lattice in both zinc- and oxygen-rich conditions. Further theoretical results also demonstrate Zn_i has a low migration barrier of 0.57 eV [23]. Besides, V_O have a relatively low E_f , but it is still high in Zn-rich condition (Figure 2). Different from Zn_i , V_O is a deep-donor defect [11, 23], and as a consequence it cannot provide electrons to the conduction-band by thermal excitation. Consequently, the observed *n*-type conductivity cannot be attributed to the V_O . In fact, the nature of the *n*-type conductivity in ZnO is still a matter of debate. However, unintentional hydrogen doping in ZnO has been considered a more likely electron source [45]. The E_f of V_{Zn} is relatively higher as compared to that of the V_O . V_{Zn} are deep-acceptor defects [11, 23], and thus it is unlikely that V_{Zn} can play any role in *p*-type conductivity. Our results also demonstrate that the Co incorporation into the *w*-ZnO are

energetically favorable in both zinc- and oxygen-rich conditions, what explains the achieved relatively high Co solubility limit in the *w*-ZnO lattice [46]. Considering the Co-doped *w*-ZnO, the obtained E_f for the analyzed point defects (Zn_i , V_O , and V_{Zn}) changes drastically, all of them are now energetically favorable. To address more properly the changes Figure 2(b) presents the difference in the E_f for each point defect between the pristine and the Co-doped *w*-ZnO systems. We observe that the main differences are related to the O-rich condition, and that V_{Zn} is the most affected defect by the Co-doping in both conditions. These results indicate that the processing of the Co:ZnO system would be quite different from that of pure *w*-ZnO, and it would lead to a quite different defect structure and physical-chemical properties that could be engineered in order to achieve functionalities that cannot be possible, or at least difficult, in the undoped *w*-ZnO.

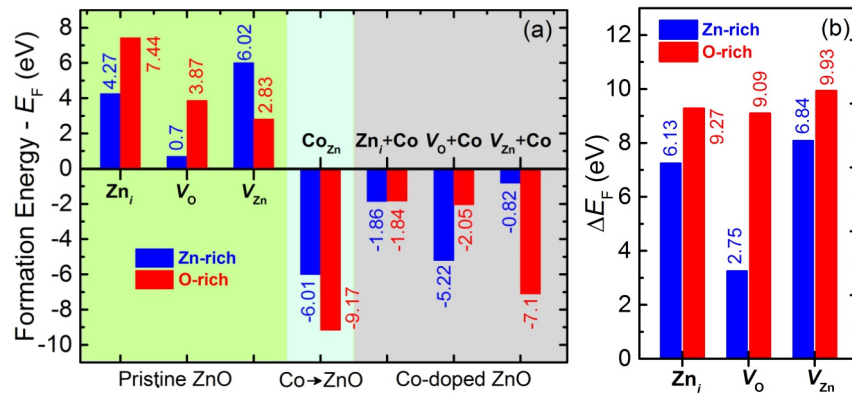


Figure 2. (a) Calculated formation energies (E_f) in Zn-rich and O-rich conditions for native point defects in pristine ZnO (Zn_i , V_O , V_{Zn} and Co_{Zn}) and Co-doped *w*-ZnO (Zn_i+Co , V_O+Co , and $V_{Zn}+Co$). (b) Difference between the defect formation energy for pristine ZnO and the Co-doped ZnO ($\Delta E_f = E_{f,ZnO} - E_{f,Co:ZnO}$).

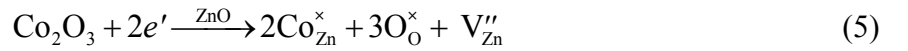
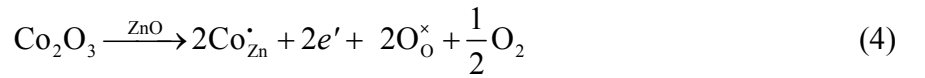
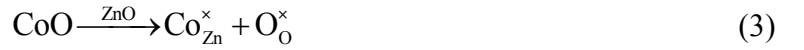
Facing these results, we proceed into defining the set of more plausible chemical reactions for our set of Co-doped *w*-ZnO samples. In spite of the calculated high E_f for Zn_i in both conditions (4.27 and 7.44 eV at Zn-rich and O-rich conditions, respectively), experimentally it was observed that under heat treatment between 300–800 °C and at lower oxygen partial pressures, *w*-ZnO decomposes incongruently by first formatting V_O , that has a lower E_f of only 0.7 eV at Zn-rich condition, on the surfaces of the material. Once the zinc atoms become mobile (Zn_i are much more mobile than V_O [23]), the zinc can be dissolved into the ZnO lattice as Zn_i according to Equation (1) [47, 48]. With the presence of the Co, both defects, Zn_i and V_O , are energetically feasible, and

the ZnO incongruent decomposition (Equation (1)) become more intense. Our previous report on the Co-doped ZnO samples confirms, via photoluminescence and *dc*-electrical measurements, an increase of the Zn_i concentration under heat treatment performed in reducing atmosphere [11]. The *w*-ZnO incongruent decomposition ends up leading to Zn-rich environment, allowing us to consider the sintering performed in Ar in this work comparable to the Zn-rich condition in our theoretical DFT calculations presented above. On the other hand, the sintering in O₂ may lead to the oxygen adsorption and the formation of mainly V_{Zn} as described in Equation (2). Our calculated E_f of the V_{Zn} is relatively high, 2.83 eV, which makes the process described in Equation (2) unprobeable. In fact, this process would lead to the creation of holes (h^*) in the valence band decreasing the *w*-ZnO *n*-type conductivity, which has not yet reported. However, with the Co the E_f of the V_{Zn} changes drastically, assuming the value of -7.1 eV. Thus, we consider the reaction described in Equation (2) in support to the following analysis.

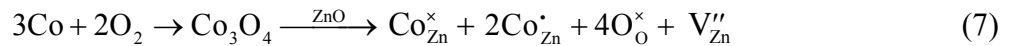


The CoO-ZnO solid solution is described in Equation (3). Once the CoO has the same *w*-ZnO stoichiometry, the reaction is independent on the processing atmosphere and on the *w*-ZnO previous defect structure. The Co incorporation into the *w*-ZnO via CoO as a precursor also does not promote any additional specific point defects. In turn, for the Co₃O₄-ZnO solid solution one has to take into account the sintering atmosphere. The Co₃O₄ crystallize in a normal spinel structure with Co²⁺ and Co³⁺ located at tetrahedral and octahedral sites, respectively [49]; and for a defect chemistry analysis it can be thought as a composition of CoO and Co₂O₃, $Co_3O_4 \leftrightarrow CoO + Co_2O_3$ [50]. In Ar (low oxygen pressure) with relatively high Zn_i concentration (Equation (1)), the Co incorporation (from Co₃O₄) is properly described via Equations (3) and (4). Here the Co incorporation into the *w*-ZnO lattice leads to the increase of the electron concentration (*n*). Besides, in O₂ atmosphere the main process is related to the oxygen incorporation with the Co

taking the Zn sites leading to formation of V_{Zn} . However, we have also to consider that experimentally it is observed in Co-doped w -ZnO samples prepared from Co_3O_4 in O-rich condition that the Co^{3+} , taking the place of the Zn^{2+} in the w -ZnO lattice, undergoes a reduction process assuming the +2 oxidation state by taking a free electron from conduction-band, reducing the w -ZnO n -type conductivity [6, 8, 11, 46]. In such case, the entire process is described by Equations (2), (3) and (5).



Considering the metallic Co insertion into the w -ZnO lattice the scenario is quite different, the process involves the oxidation of the Co atom. In Ar atmosphere, the Co incorporation takes place by sitting in the Zn site and forming V_O . Here, we have to consider a probable oxidation of the metallic Co once placed in an oxide matrix, and that, as pointed before, V_O is a deep-donor defect, its ionization is quite unlikely. In such situation, the Co-doping of the w -ZnO lattice can be described by Equation (6) with no changes in the w -ZnO n -type conductivity. In the O_2 atmosphere we infer that the main process corresponds to the oxygen adsorption described in Equation (2), followed for the Co filling the zinc vacant site, with the holes compensated by the electrons related to the Co oxidation process. These processes are simply described by Equation (7).



In summary, the defect chemistry of the Co-doped w -ZnO is very rich and diverse, depending on the precursor, CoO , Co_3O_4 or metallic Co, and on the atmosphere. Besides the total Co incorporation into the w -ZnO lattice, different point defects are introduced, leading to changes of the electron band structure, corresponding to changes in the w -ZnO electrical transport, optical and magnetic properties.

3.2 Studies on the Co incorporation into the *w*-ZnO lattice:

Figure 3 presents the XRD patterns for the *m*Co:ZnO set of samples prepared in O₂ (Figure 3(a)) and in Ar (Figure 3(b)) up to 1000 °C. The XRD data for all the Co:ZnO set of samples are presented in the supplementary file (Figures S1, S2, and S3). The observed diffraction pattern for all the samples sintered in O₂ and Ar at 1000 °C and at higher temperatures reveals, within the detection limit of the technique, only the characteristic diffraction peaks corresponding to those for *w*-ZnO lattice (ICDD crystal chart no. 36-1451). No segregated phases were detected, indicating that at around 1000 °C and higher temperatures the Co atoms are taking the place of the Zn in the *w*-ZnO lattice forming the ternary compound Zn_{1-x}Co_xO (substitutive doping). For samples sintered at temperatures below 1000 °C, in both atmospheres, it is observed, besides the *w*-ZnO diffraction pattern, the presence of diffraction peaks associated with metallic Co and Co oxides (CoO and Co₃O₄). Qualitatively, it is observed that the diffraction peaks related to the secondary phases decreases in intensity with increasing temperature of sintering. However, the dynamics of the Co incorporation into the *w*-ZnO lattice is distinct as considering the atmosphere of sintering and the different precursors, thus indicating that the incorporation is quite sensitive to these parameters.

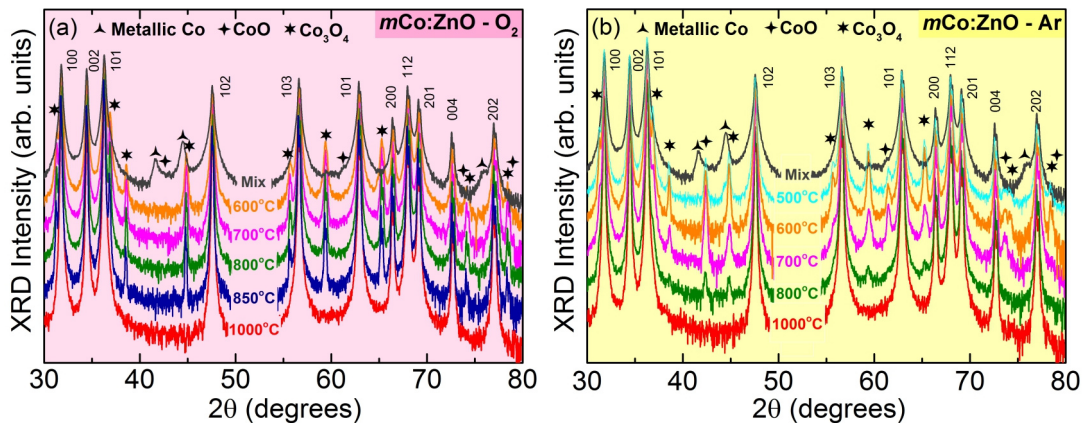


Figure 3. X-Ray diffraction pattern for the *m*Co-ZnO set of samples prepared in (a) oxygen (O₂) and (b) argon (Ar) atmospheres up to 1000 °C.

Rietveld refinement of the XRD data was performed to quantify the lattice parameters, the phase percentages (*w*-ZnO, metallic Co, CoO and Co₃O₄) and the elemental occupation factors

into the w -ZnO structure for the elements Zn, Co and O for each set of samples. The obtained results are presented in Table S1–S6 in the supplementary file. We observe that the occupation factor for the Co into the w -ZnO lattice, which is assumed as the effective concentration of cobalt incorporated into the ZnO matrix (x_E), increases as the temperature of sintering increases. It reaches the maximum nominal concentration of 8 at.% for temperatures around 900–1000 °C. Figure 4 shows the calculated unit cell volume (V in Table S2, S4 and S6) as a function of the obtained effective Co concentration incorporated in the w -ZnO lattice in our samples (x_E in Table S1, S3 and S5). We observe a slight linear increase of V as a function of x_E , as expected by the Vegard's law for solid state solutions, indicating the Co incorporation into the w -ZnO lattice. Nevertheless, the increase in the cell volume is not expected, since the ionic radii of tetrahedrally coordinated Co^{2+} ($r_{\text{Co}} = 0.58 \text{ \AA}$) is slightly smaller than that for Zn^{2+} in the w -ZnO structure ($r_{\text{Zn}} = 0.60 \text{ \AA}$) [51]. Such kind of behavior was already reported by Kolesnik *et al.* [52]. Here we attribute this unexpected result to the induced structural defects promoted by the Co incorporation. However, further studies are necessary to address this point.

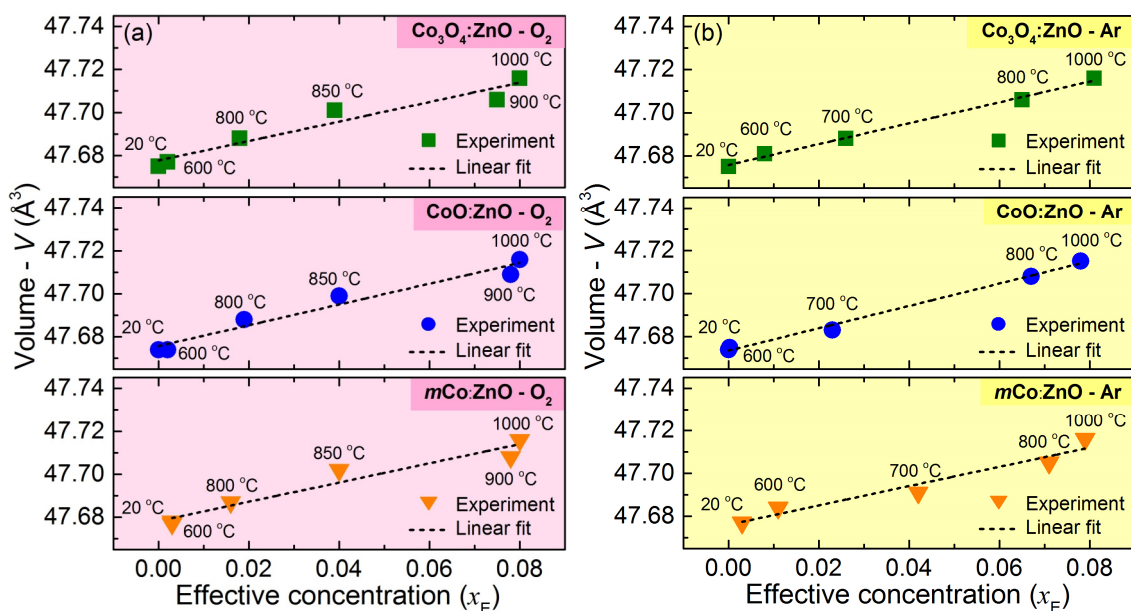


Figure 4. Variation of the w -ZnO lattice volume (V) as a function of the Co effective concentration (x_E) incorporated into the w -ZnO lattice for the set of samples prepared in (a) oxygen (O_2) and (b) argon (Ar) atmospheres. The linear behavior of $V \times x_E$ is consistent with the Vegard's law.

In order to complement the structural characterization of the samples we performed Raman

scattering spectroscopy measurements. Figure 5 presents the obtained spectra for the $m\text{Co}:\text{ZnO}$ set of samples prepared in O_2 (Figure 5(a)) and in Ar (Figure 5(b)) up to 1000 °C. Figure S4 in the supplementary file present the measured spectra for the $\text{CoO}:\text{ZnO}$ and $\text{Co}_3\text{O}_4:\text{ZnO}$ set of samples. The modes at 98, 330, 384 and 435 cm^{-1} are associated with first and second order modes characteristic of the $w\text{-ZnO}$ and correspond to the modes E_{2L} , $2E_{2L}$ at the M-point of the Brillouin zone (BZ), $A_1(\text{TO})$ e E_{2H} , respectively [46, 53]. The modes related to cobalt oxides are also shown in Figure 5. The indexation of the cobalt oxide modes was performed after measure the spectrum for the raw precursors (Figure S5). An important observed feature is the presence of modes above 700 cm^{-1} and the relative high intensity of the mode at $\sim 522 \text{ cm}^{-1}$ (open stars in Figure 5). As can be seen in Figure S5, these features are not present in the raw cobalt oxide precursors, instead, they are clearly observed in the spectra for Zn-doped cobalt oxides, indicating an interdiffusion of the cations between the $w\text{-ZnO}$ and cobalt oxides (CoO and Co_3O_4) during sample processing.

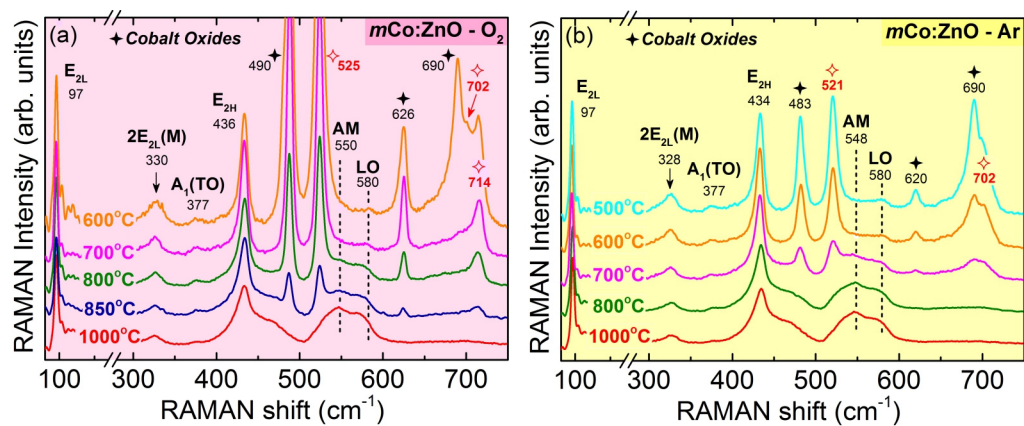


Figure 5. Raman scattering spectra for the $m\text{Co}:\text{ZnO}$ set of samples prepared in (a) oxygen (O_2) and (b) argon (Ar) atmospheres up to 1000 °C. The spectra were acquired at room temperature and are normalized by integrated area of the E_{2H} vibrational mode obtained by gaussian fit of the spectra. The stars (symbols) indicate the cobalt oxide related modes. The modes marked with the open stars indicate the Zn-doping of the CoO and Co_3O_4 .

As the temperature of sintering increases the modes related to the cobalt oxides decreases indicating a progressive Co incorporation into the $w\text{-ZnO}$ lattice. It is also important to note the emergence of a broadband between 500 and 600 cm^{-1} as the temperature of sintering increases. This broadband consists of the convolution of several modes, but the main ones are centered ~ 550 and $\sim 580 \text{ cm}^{-1}$. The peak in 580 cm^{-1} is assigned to the overlapping between the $A_1(\text{LO})$ and $E_1(\text{LO})$

modes, however the peak in 550 cm^{-1} cannot be attributed in any of the w -ZnO vibrational modes, it is indexed as AM (additional mode) in the spectra. The observation of this broad band and its dependence on the dopant concentration is well report on the literature for doped w -ZnO with different elements, including Mn [7, 9, 54] and Co [6, 32, 46], and its nature is correlate to structural disorder/distortions induced by the incorporation of dopants into the w -ZnO lattice [55]. Consequently, the observation of the broadband for our samples and its increase as the temperature of sintering is raised is an indication that a growing fraction of the Co atoms is successively incorporated into the w -ZnO lattice as the temperature of sintering increases.

Figure 6 presents the PL spectra of the $m\text{Co}:\text{ZnO}$ set of samples prepared in O_2 (Figure 6(a)) and in Ar (Figure 6(b)) up to $1000\text{ }^\circ\text{C}$ obtained at room temperature and excited with a 532 nm (2.33 eV) laser light. The spectra for the other set of samples, $\text{Co}_3\text{O}_4:\text{ZnO}$ and $\text{CoO}:\text{ZnO}$, are presented if Figures S6 and S7, respectively. The emission band at 1.8 eV (690 nm) is associated with relaxations from excited states to ${}^2\text{E}({}^2\text{G})$ state, followed by a transition from ${}^2\text{E}({}^2\text{G})$ to the ${}^4\text{A}_2({}^4\text{F})$ ground state of Co^{2+} in the $3d^7$ high-spin configuration in a tetrahedral crystalline field formed by the O^{2-} ions in its neighborhood [56, 57]. The identification of the PL spectra related to the Co^{2+} inner transitions is an evidence that the Co ions in our samples are undoubtedly incorporated into the w -ZnO lattice. As the temperature of sintering increases the amount of the Co ions incorporated the Zn tetrahedral site of the w -ZnO lattice increases, leading to the increase of the PL intensity as function of the temperature of sintering observed in Figure 6(a) and 6(b). The calculated integrated area under the PL spectrum for each temperature plotted as a function of x_E obtained from the Rietveld structural refinement is presented in Figure 6(c) and 6(d). It is observed a linear behavior, this result support and validates the calculated values for x_E for the different temperatures of sintering. We can also observe a redshift of the maximum of the PL spectrum as function of the temperature of sintering. Since this emission is related to the structural crystalline field, the redshift can be understood in terms of the structural disorder/distortions introduced by the increasing of the Co concentration incorporated into the w -ZnO lattice, in

concordance with the Raman results, and the calculated changes in the cell parameters obtained via the Rietveld structural refinement.

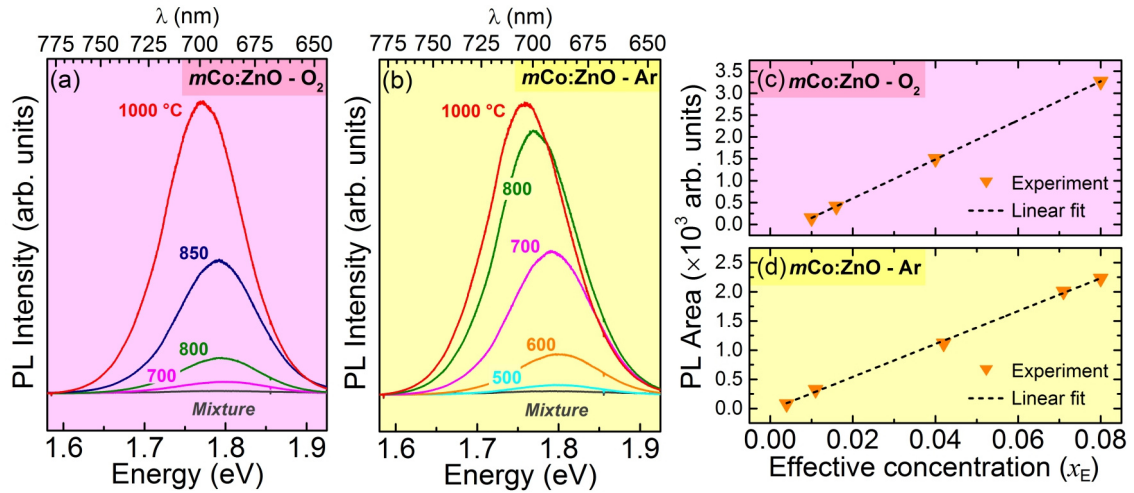


Figure 6. Room temperature PL spectra for part of the set of samples $m\text{Co}:\text{ZnO}$ prepared in (a) oxygen (O_2) and (b) argon (Ar) atmospheres. It was used a 532 nm laser for excitation with optical power density of $50 \text{ kW}/\text{cm}^2$. Integrated area underneath the spectra plotted as a function of the calculated effective cobalt concentration (x_E) for the samples prepared in (c) O_2 and in (d) Ar.

As previously highlighted, the fraction of incorporated Co into the w -ZnO lattice depends on the temperature of sintering, on the atmosphere, and on the Co precursor source, which indicates different chemical dynamics for each set of parameters as discussed in the previous section. Here, a very important factor that can be extracted from our results is the apparent activation energy (Q_i) for the Co incorporation into the w -ZnO lattice. Figure 7 present the Arrhenius plot of the x_E versus the absolute temperature of sintering for each used atmosphere. The obtained Q_i for each sample is presented also in Figure 7. These results show a substantial difference between the samples sintered in Ar and O_2 . The Q_i for samples sintered in Ar are relatively low as compared to the values obtained for the set of samples processed in O_2 . Considering the precursors, metallic Co stands out among the three used ones presenting the lowest Q_i in both atmospheres.

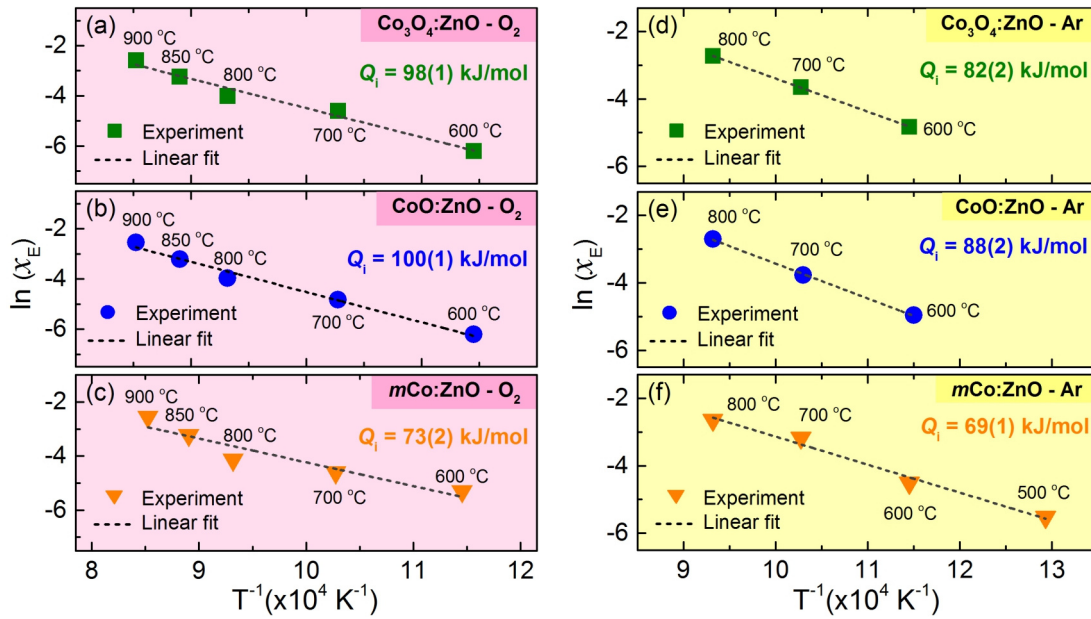


Figure 7. Arrhenius plot. Logarithm of the effective Co concentration (x_E) versus the inverse of the temperature of sintering for the set of samples prepared in (a) oxygen (O₂) and (b) argon (Ar) atmospheres. In the inset it is presented the apparent activation energy (Q_i) for the Co incorporation into the *w*-ZnO lattice for each case.

From the Rietveld refinement we can extract information to understand the obtained Q_i values. First, at low temperature (600 °C) and under O₂ atmosphere, the CoO oxidize almost completely to Co₃O₄. These explain why the Q_i for the CoO:ZnO and Co₃O₄:ZnO set of samples sintered in O₂ are quite similar. Besides, at Ar atmosphere, in a lesser extent as compared to the O₂ atmosphere, the CoO (CoO:ZnO set of samples) and the metallic Co (mCo:ZnO) also oxidizes, CoO to Co₃O₄ and metallic Co to CoO and to Co₃O₄ (Table S3 and S5). The oxidation of the Co precursors in Ar indicates that the ZnO decomposes, most probably via the chemical defect reaction described by Equation (1). Therefore, we can infer that the decomposition of the ZnO in Ar atmosphere favors the Co incorporation into the *w*-ZnO lattice, leading to the relatively lower Q_i for these set of samples. Among the samples sintered at the same atmosphere the CoO:ZnO set of samples presents the higher Q_i as compared with the others precursor sources. This behavior can be addressed to the CoO higher melting point (1930 °C) as compared to that of the Co₃O₄ (895 °C) and the metallic Co (1495 °C). It is noteworthy that the fraction of CoO remains in the powder mixture even at higher temperature (800 °C) due to the reduction of the formed Co₃O₄ again into CoO in Ar atmosphere at this temperature range (Table S3) [58]. Finally, as mentioned before, the

mCo:ZnO set of samples presents the lowest Q_i for both O₂ and Ar atmospheres. For instance, at 700 °C in Ar atmosphere the Co solubility limit achieved with metallic Co is 4.2 at.%, while for CoO and Co₃O₄ it is 2.3 and 2.6 at.%, respectively (Tables S1, S3 and S5). Taking again into account the difference between the melting temperatures for the Co₃O₄ (895 °C) and for the metallic Co (1495 °C), and considering the entire process of the material dissociation, changing of oxidation state, and lattice incorporation, we can conclude that the oxidation of the metallic Co is considerably less energetically expensive than the reduction of the cobalt in the Co₃O₄ during the Co incorporation into the *w*-ZnO lattice.

3.3 Studies on the Grain Growth Kinetics of the Co:ZnO Ceramics

In this section we present the studies concerning the grain growth kinetics for the Co:ZnO set of samples prepared with the different precursors: Co₃O₄ (Co₃O₄:ZnO), CoO (CoO:ZnO) and metallic Co (*mCo:ZnO*). As a reference, a pure ZnO (ZnO) set of samples were processed at the same condition as the Co:ZnO samples. Figure S8 presents representative SEM images acquired over the surface of the compacted resulted powder mixtures (ZnO, Co₃O₄:ZnO, CoO:ZnO and *mCo:ZnO*) after the high-energy ball milling process, and before the sintering for comparison. Representative SEM images of the set of sintered samples at different temperatures (600–1200 °C) in O₂ and Ar for 4 hours are presented in Figures S9, S11, S13 and S15 for the ZnO, Co₃O₄:ZnO, CoO:ZnO and *mCo:ZnO*, respectively. The histograms concerning the distribution of the main particle diameters are presented in Figures S10, S12, S14 and S16, and the parameters obtained after a statistical analysis performed via log-normal fit of the histograms are presented in Tables S7, S8, S9 and S10 also for the ZnO, Co₃O₄:ZnO, CoO:ZnO and *mCo:ZnO*, respectively. The statistical analysis gives us the main diameter (L) of the particles and the geometric standard deviation (σ_g) of the distributions. Grain sizes (G) is obtained directly from the L as described by Mendelson [59]:

$$G = 1.56 L. \quad (8)$$

The grain size statistical analysis for each mixture presented in Figure S8 reveals a sharp

distribution with a mean diameter (L) around 100 nm, confirming the nanostructured nature of the starting powders and the efficiency of the high-energy ball milling process in reduce the dimensionality of the grain powder mixtures down to the nanoscale. The obtained statistical numbers are quite similar, revealing a homogeneous starting point for the entire set of studied samples. This condition is very important in order to compare the grain growth parameters for each studied cobalt precursor (Co_3O_4 , CoO and $m\text{Co}$). Figure 8 present the grain size (G) for the set of samples sintered in (a) O_2 and (b) Ar for 4 hours. It is observed that the increase of the grain size with temperature has an exponential character, and that the $\text{Co}_3\text{O}_4:\text{ZnO}/\text{ZnO}$ set of samples present the highest/lowest growth rate in both O_2 and Ar atmospheres. This result indicates that the Co_3O_4 is a good additive for the ZnO sintering in order to achieve larger grains and densities.

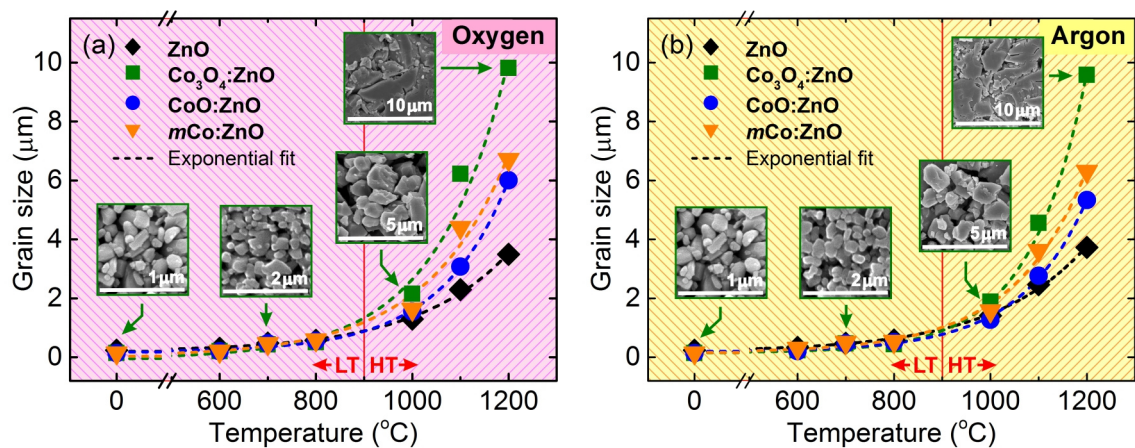


Figure 8. Grain size (G) of the samples sintered in (a) oxygen (O_2) and (b) argon (Ar). The grain size corresponds to the main diameter obtained after a statistical analysis performed via log-normal fit of the size distribution histograms. The data was fit via an exponential function to highlight the exponential character of the grain growth. In the inset is presented representative electron micrographs of the $\text{Co}_3\text{O}_4:\text{ZnO}$ set of samples showing the evolution of the grains size as a function of the sintering temperature. The vertical red line at 900 °C separates the low temperature (LT) from the high temperature (HT) grain growth regimes.

Assuming a negligible initial grain size, the grain growth kinetics can be determined using the simplified phenomenological kinetics proposed by T. Senda and R. C. Bradt through the Equation (9) [60]. It can be rewriting as in Equation (10) and (11).

$$G^n = K_0 t \exp(-Q_g / RT). \quad (9)$$

$$\log G = \left(\frac{1}{n}\right) \log t + \left(\frac{1}{n}\right) \left[\log K_0 - 0.434 \left(\frac{Q_g}{RT} \right) \right]. \quad (10)$$

$$\log \left(\frac{G^n}{t} \right) = \log K_0 - 0.434 \left(\frac{Q_g}{RT} \right). \quad (11)$$

Here the main parameters are the grain growth kinetic exponent (n), and the grain growth apparent activation energy (Q_g). K_0 is a pre-exponential constant, t is the time in hours, R is the gas constant (8.31 J/mol·K), and T is the absolute temperature. n can be determined by the inverse of slope of the curve as defined in Equation (10) for a set of samples processed at the same T and different t . In turn, with the value of n in hands, Q_g can be calculated from the slope of the Arrhenius plot of the $\log(G^n/t)$ versus $1/T$ for a set of samples processed at the same t and different T (Equation (10)). Higher n -values and lower Q_g leads to higher grain growth rates, n is related to the mass transport mechanism, while Q_g holds its standard meaning [61].

The sintering, and the consequent grain growth, of a starting nanostructured powder has to be analysed carefully [48]. Figure S17 and S18 present representative micrographs for the pure ZnO and for the $m\text{Co}:\text{ZnO}$ samples, respectively. The micrographs show the samples before and after sintering in the O_2 and Ar atmospheres in the temperatures of 700 °C and 1200 °C. We observe for the samples sintered at 700 °C a relatively small shrinkage of the powder after the sintering, besides, for the samples sintered at 1200 °C the shrinkage is quite considerably. From this result we can infer that for the starting nanostructured powders at lower temperatures the coarsening dominates the grain growth process (rearrangement of the particles and formation of necks), while at high temperatures, with grains already of the size of the order of micrometres, the densification process takes place. Consequently, we can state, as it is expected, that the growth mechanism at low temperatures is distinct from that at higher temperatures. For small particles and material of high vapor pressure the evaporation-condensation sintering process is favourable, and at low temperatures the relatively low activation energy process, like the surface diffusion, dominates, what leads to coarsening [62]. At high temperatures, process of high activation energy, like grain boundary and bulk diffusion, dominates [60]. Nevertheless, sintering involves several mechanisms operating simultaneously over overlapping stages. In fact, there are numerous studies

on the grain growth kinetics of ZnO, these studies have revealed that the rate controlling mechanism is the Zn^{2+} diffusion, which proceeds via surface at the LT regime [62] and via bulk at the HT regime [60, 63]. Therefore, here the grain growth process is analysed in two different regimes, one below around 900 °C, referred as low temperature regime (LT), and other above 900 °C, referred as high temperature regime (HT).

Figure 9 shows the plot of the $\log(G)$ versus $\log(t)$ (Equation (10)) for the entire set of samples obtained at the 700 °C (LT) and 1200 °C (HT). Representative SEM images of the entire set of samples sintered at different times (1, 1.5, 2, 2.5 and 3h), and the histograms concerning the distribution of the main particle diameters are presented in Figures S19 to S34. The correspondent obtained statistical parameters are presented in Tables S11 to S18 of the supplementary file. Figure 10 shows the Arrhenius plot of $\log(G^n/t)$ versus $(1/T)$ (Equation (11)) for pure ZnO and Co:ZnO set of samples sintered for 4h in O₂ and Ar.

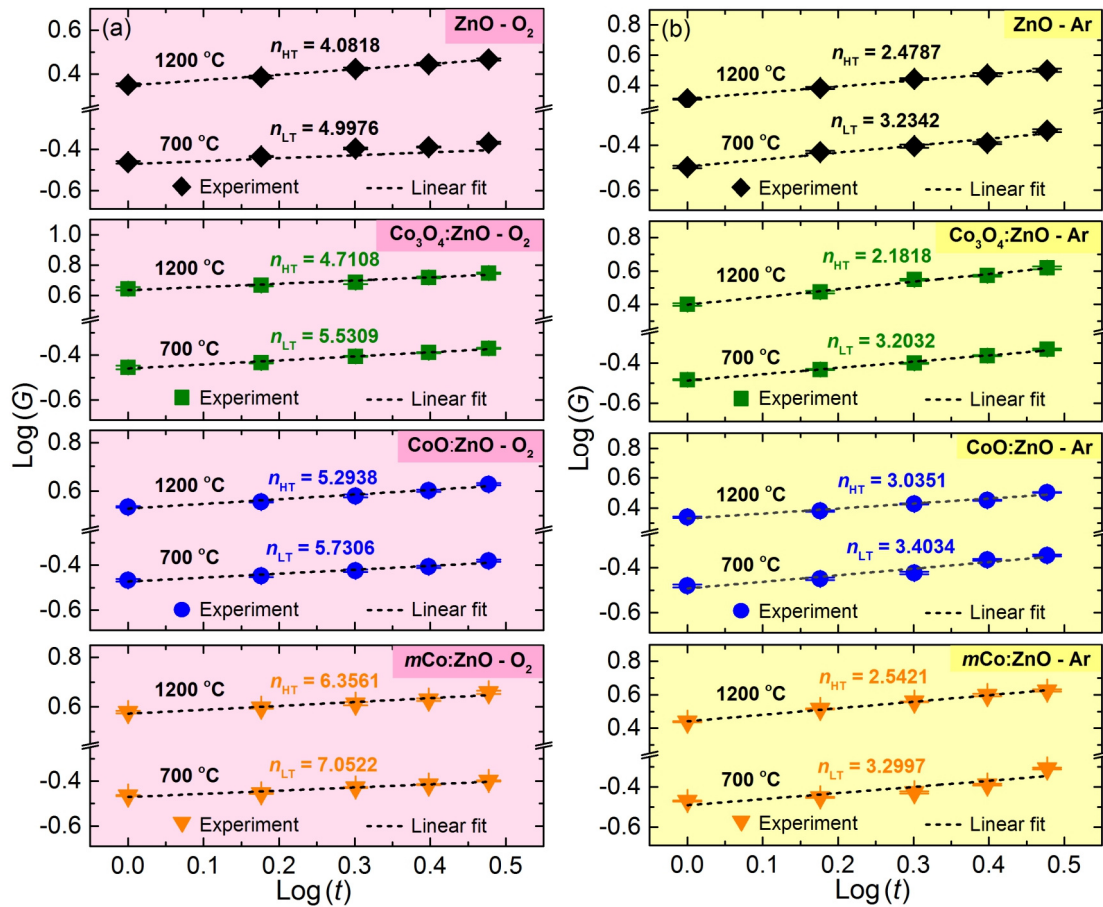


Figure 9. Isothermal grain growth of ZnO and Co:ZnO set of samples sintered in (a) oxygen (O₂) and (b) argon (Ar).

The obtained n -values and the grain growth apparent activation energy (Q_g) after a linear fit of the experimental points are presented in Table 1 and Table 2. First, we call attention to that the n -values for samples processed at 700 °C is quite different from those for samples processed at 1200 °C in all cases, and it is evident from Figure 10 the difference between the slope of the curves in the different temperature ranges, confirming the statement of the LT and HT grain growth regimes associated to different grain growth mechanisms. Comparing the n and Q_g values at the LT and HT regime for the same atmosphere we note that Q_g is larger at HT regime, as we would expect, while n is larger at the LT regime. Besides, both parameters n and Q_g are larger for the Co:ZnO set of samples are higher than those for the pure ZnO sintered in O₂ and Ar atmospheres. Both parameters are also larger for samples sintered in O₂ as compared to those for samples sintered in Ar.

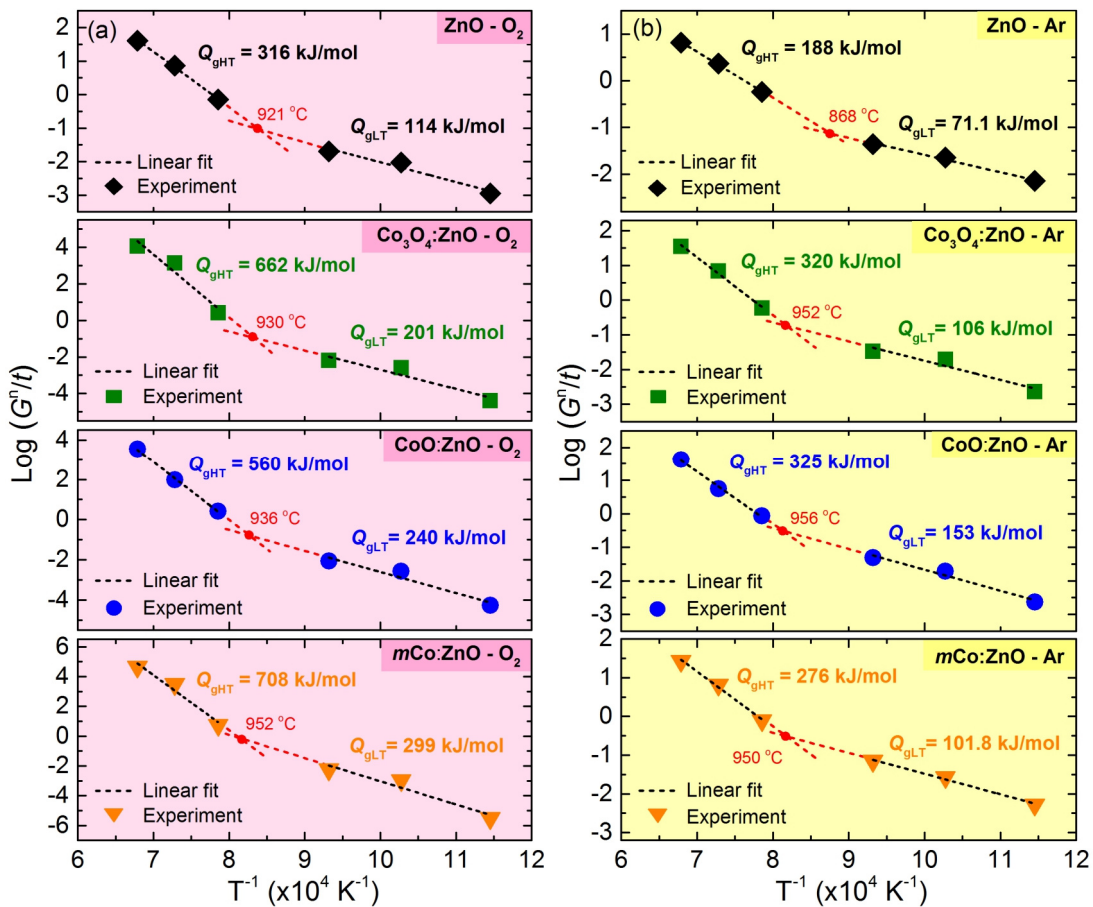


Figure 10. Arrhenius plots for the grain growth of ZnO and Co:ZnO set of samples sintered in (a) oxygen (O₂) and (b) argon (Ar).

First, it is important to point that the obtained n and Q_g for the pure ZnO system is relatively close to those reported in the literature [60, 64-66]. The differences in n and Q_g at LT and HT ranges are quite understood in terms of the change of the main growth process in the different temperature ranges. As stated before, n is related to mass transport process, and at high temperature processes corresponding to higher Q_g are activated. For the Co:ZnO it is plausible to infer that the Co incorporation into the w -ZnO lattice takes place mainly at the surface of the w -ZnO grains, changing drastically the diffusion and subsequent grain boundary mobility, what leads to the increasing of the Q_g for those samples. Besides, the samples sintered in O_2 present higher n -values due probably to the promoted higher density of V_{Zn} , in the same way, the addition of Co to the system favor the formation of both V_{Zn} and Zn_i defects (full analysis presented in section 3.1) increasing Zn^{2+} diffusion, and leading to a faster growth rate. Finally, both n and Q_g is lower for the samples sintered in Ar. The relative decrease in n can be interpreted by the suppression of the V_{Zn} , while the decrease in Q_g can be attributed to a higher Co solubility into the w -ZnO lattice (full analysis presented in section 3.2), what would lead to more homogeneous distribution into the w -ZnO grain and not to a higher concentration at grain surface. The lower Q_g for the $mCo:ZnO$ set of samples, which presents the lower Q_i (Figure 7), corroborates this statement.

Table 1. Grain growth kinetic parameters obtained in the range of temperatures below 900 °C (LT regime): grain growth kinetic exponent (n), grain growth apparent activation energy (Q_{gLT}), and log K_0 (for completeness).

	Sample	log K_0	n	Q_{gLT} (kJ/mol)
<i>Oxygen</i>	ZnO	4(1)	4.9976	114(3)
	CoO:ZnO	8(3)	5.7306	240(2)
	Co ₃ O ₄ :ZnO	7(3)	5.5309	201(1)
	<i>mCo</i> :ZnO	13(4)	7.0522	299(2)
<i>Argon</i>	ZnO	2.1(4)	3.2342	71.1(7)
	CoO:ZnO	5(1)	3.4034	153(2)
	Co ₃ O ₄ :ZnO	4(2)	3.2032	106(2)
	<i>mCo</i> :ZnO	4(1)	3.2997	101.8(5)

Table 2. Grain growth kinetic parameters obtained in the range of temperatures above 900 °C (HT regime): grain growth kinetic exponent (n), grain growth apparent activation energy (Q_{gHT}), and $\log K_0$ (for completeness).

	Sample	$\log K_0$	n	Q_{gHT} (kJ/mol)
<i>Oxygen</i>	ZnO	12.8(6)	4.0665	316(2)
	CoO:ZnO	23(1)	5.2938	560(3)
	Co ₃ O ₄ :ZnO	27(6)	4.7108	662(5)
	<i>m</i> Co:ZnO	30(5)	6.3561	708(3)
<i>Argon</i>	ZnO	7.5(3)	2.4787	188(1)
	CoO:ZnO	12.4(8)	3.0351	325(2)
	Co ₃ O ₄ :ZnO	13(1)	2.1818	320(2)
	<i>m</i> Co:ZnO	11(1)	2.5421	276(1)

Returning to the results concerning the obtained final grain sizes presented in Figure 8. Remember that for a given T and t , the grain size (G) depends on both n and Q_g (Equation (9)), larger n leads to larger G , and larger Q_g leads to smaller G . Our results indicate a competition between these parameters. For samples sintered in O₂, adding Co to the system increases Q_g , however n is also increased, with a final effect corresponding to a higher G in comparison to the pure ZnO set of samples. For the samples sintered in Ar, Q_g decreases in comparison to values for the O₂ atmosphere, however n also decreases, in such a way that the final G remains almost the same as for the samples sintered in O₂. Among the samples sintered in Ar, the addition of Co also increases n and Q_g .

4 CONCLUSION

In summary, in this report we presented a systematic study concerning the processing of Co:ZnO ceramics. Different Co precursors (Co₃O₄, CoO and metallic Co) and sintering atmospheres (O₂ and Ar) was analyzed from the theoretical and experimental point of view. The theoretical calculation showed that the main point defects (Zn_i , V_O and V_{Zn}) became energetically favorable in the presence of cobalt. Based on the theoretical finds a set of defect chemical reaction was proposed. The studies on the Co incorporation into the w -ZnO was conducted carefully in

order to properly address the Co-doping of the *w*-ZnO. The analysis showed that the Ar sintering atmosphere promotes an incongruent decomposition of the ZnO, leading to a higher Zn_i density and a higher Co solubility. Among the Co precursors the metallic Co proved to be the one with higher solubility into the *w*-ZnO (lower Q_i). The evaluation of the grain growth kinetics revealed a very rich dynamic. In order to achieve high grain growth and densities the Co_3O_4 demonstrated to be a good additive for the *w*-ZnO sintering. It was observed that due to the competition between different mass transport mechanism (n) and the different Co incorporation degrees (Q_g) the final grain size is almost independent of the sintering atmosphere. Evidences showed that in the Ar sintering atmosphere the metallic Co precursor, due to its higher solubility into the *w*-ZnO lattice, leads to a high Co homogeneous distribution over the volume of the *w*-ZnO grain. Besides, CoO precursor present the lowest solubility into *w*-ZnO lattice and final grain size, being the CoO the best precursor for top-down approach in processing of Co-doped *w*-ZnO nanopowders. Our findings give valuable contribution to the understanding of the preparation of Co-doped *w*-ZnO ceramics and the sintering growth kinetics, what would allow to improve the state of the art on the processing of the material at both bulk and nanometric scales.

ACKNOWLEDGMENTS

Support from agencies CAPES and FAPEMIG is gratefully acknowledged. The authors also acknowledge Prof. Dr. A. C. Doriguetto coordinator of the Laboratório de Cristalografia of the Universidade Federal de Alfenas where the XRD measurements were performed.

REFERENCES

- [1] H.L. Tuller, S.R. Bishop, Point Defects in Oxides: Tailoring Materials Through Defect Engineering, Annual Review of Materials Research, Vol 41 41 (2011) 369-398.
- [2] I. Zutic, J. Fabian, S. Das Sarma, Spintronics: Fundamentals and applications, Reviews of Modern Physics 76(2) (2004) 323-410.
- [3] M. Knobel, J.C. Denardin, H.B. De Carvalho, M. Brasil, A.B. Pakhomov, F.P. Missell, Magnetic and magnetotransport properties of Co thin films on Si, Physica Status Solidi a-Applied Research 187(1) (2001) 177-188.
- [4] H.B. de Carvalho, M. Brasil, J.C. Denardin, M. Knobel, Transport and magnetotransport transition of thin Co films grown on Si, Physica Status Solidi a-Applied Research 201(10) (2004) 2361-2365.

- [5] M.Y. He, H.M. Sun, Q.L. He, Topological insulator: Spintronics and quantum computations, *Frontiers of Physics* 14(4) (2019).
- [6] H.B. de Carvalho, M.P.F. de Godoy, R.W.D. Paes, M. Mir, A. Ortiz de Zavallos, F. Iikawa, M.J.S.P. Brasil, V.A. Chitta, W.B. Ferraz, M.A. Boselli, A.C.S. Sabioni, Absence of ferromagnetic order in high quality bulk Co-doped ZnO samples, *J Appl. Phys.* 108(3) (2010) 033914.
- [7] V.M.A. Lage, R.T. da Silva, A. Mesquita, M.P.F. de Godoy, X. Gratens, V.A. Chitta, H.B. de Carvalho, Influence of reducing heat treatment on the structural and magnetic properties of MnO:ZnO ceramics, *Journal of Alloys and Compounds* 863 (2021).
- [8] M.P.F. de Godoy, A. Mesquita, W. Avansi, P.P. Neves, V.A. Chitta, W.B. Ferraz, M.A. Boselli, A.C.S. Sabioni, H.B. de Carvalho, Evidence of defect-mediated magnetic coupling on hydrogenated Co-doped ZnO, *Journal of Alloys and Compounds* 555 (2013) 315-319.
- [9] V.M. de Almeida, A. Mesquita, A.O. de Zavallos, N.C. Mamani, P.P. Neves, X. Gratens, V.A. Chitta, W.B. Ferraz, A.C. Doriguetto, A.C.S. Sabioni, H.B. de Carvalho, Room temperature ferromagnetism promoted by defects at zinc sites in Mn-doped ZnO, *Journal of Alloys and Compounds* 655 (2016) 406-414.
- [10] N.C. Mamani, R.T. da Silva, A.O. de Zavallos, A.A.C. Cotta, W.A.D. Macedo, M.S. Li, M.I.B. Bernardi, A.C. Doriguetto, H.B. de Carvalho, On the nature of the room temperature ferromagnetism in nanoparticulate Co-doped ZnO thin films prepared by EB-PVD, *Journal of Alloys and Compounds* 695 (2017) 2682-2688.
- [11] M.P.F. de Godoy, X. Gratens, V.A. Chitta, A. Mesquita, M.M. de Lima, A. Cantarero, G. Rahman, J.M. Morbec, H.B. de Carvalho, Defect induced room temperature ferromagnetism in high quality Co-doped ZnO bulk samples, *Journal of Alloys and Compounds* 859 (2021) 157772.
- [12] Y. Belghazi, G. Schmerber, S. Colis, J.L. Rehspringer, A. Dinia, Extrinsic origin of ferromagnetism in ZnO and Zn_{0.9}Co_{0.1}O magnetic semiconductor films prepared by sol-gel technique, *Appl. Phys. Lett.* 89(12) (2006) 122504.
- [13] J.M.D. Coey, Dilute magnetic oxides, *Curr. Opin. Solid State Mater. Sci.* 10(2) (2006) 83-92.
- [14] D.C. Kundaliya, S.B. Ogale, S.E. Lofland, S. Dhar, C.J. Metting, S.R. Shinde, Z. Ma, B. Varughese, K.V. Ramanujachary, L. Salamanca-Riba, T. Venkatesan, On the origin of high-temperature ferromagnetism in the low-temperature-processed Mn-Zn-O system, *Nat. Mater.* 3(10) (2004) 709-714.
- [15] M. Tay, Y.H. Wu, G.C. Han, T.C. Chong, Y.K. Zheng, S.J. Wang, Y.B. Chen, X.Q. Pan, Ferromagnetism in inhomogeneous Zn_{1-x}Co_xO thin films, *J Appl. Phys.* 100(6) (2006) 063910.
- [16] J.M.D. Coey, M. Venkatesan, C.B. Fitzgerald, Donor impurity band exchange in dilute ferromagnetic oxides, *Nature Materials* 4(2) (2005) 173-179.
- [17] K.R. Kittilstved, W.K. Liu, D.R. Gamelin, Electronic structure origins of polarity-dependent high-T_C ferromagnetism in oxide-diluted magnetic semiconductors, *Nature Materials* 5(4) (2006) 291-297.
- [18] M. Ivill, S.J. Pearton, S. Rawal, L. Leu, P. Sadik, R. Das, A.F. Hebard, M. Chisholm, J.D. Budai, D.P. Norton, Structure and magnetism of cobalt-doped ZnO thin films, *New Journal of Physics* 10 (2008).
- [19] S. Ramachandran, J. Narayan, J.T. Prater, Effect of oxygen annealing on Mn doped ZnO diluted magnetic semiconductors, *Applied Physics Letters* 88(24) (2006).

- [20] H.S. Hsu, J.C.A. Huang, Y.H. Huang, Y.F. Liao, M.Z. Lin, C.H. Lee, J.F. Lee, S.F. Chen, L.Y. Lai, C.P. Liu, Evidence of oxygen vacancy enhanced room-temperature ferromagnetism in Co-doped ZnO, *Applied Physics Letters* 88(24) (2006).
- [21] T. Tietze, M. Gacic, G. Schutz, G. Jakob, S. Bruck, E. Goering, XMCD studies on Co and Li doped ZnO magnetic semiconductors, *New Journal of Physics* 10 (2008).
- [22] P. Xu, Y. Sun, C. Shi, F. Xu, H. Pan, The electronic structure and spectral properties of ZnO and its defects, *Nuclear Instruments & Methods in Physics Research Section B-Beam Interactions With Materials and Atoms* 199 (2003) 286-290.
- [23] A. Janotti, C.G. Van de Walle, Native point defects in ZnO, *Physical Review B* 76(16) (2007) 165202.
- [24] D.C. Look, J.W. Hemsky, J.R. Sizelove, Residual native shallow donor in ZnO, *Physical Review Letters* 82(12) (1999) 2552-2555.
- [25] H.Y. Zhang, W. Hao, Y.Q. Cao, X.F. Chang, M.X. Xu, X.L. Guo, K. Shen, D.H. Xiang, Q.Y. Xu, Room temperature ferromagnetic Zn_{0.98}Co_{0.02}O powders with improved visible-light photocatalysis, *Rsc Advances* 6(8) (2016) 6761-6767.
- [26] L.R. Shah, H. Zhu, W.G. Wang, B. Ali, T. Zhu, X. Fan, Y.Q. Song, Q.Y. Wen, H.W. Zhang, S.I. Shah, J.Q. Xiao, Effect of Zn interstitials on the magnetic and transport properties of bulk Co-doped ZnO, *Journal of Physics D-Applied Physics* 43(3) (2010).
- [27] N. Khare, M.J. Kappers, M. Wei, M.G. Blamire, J.L. MacManus-Driscoll, Defect-induced ferromagnetism in co-doped ZnO, *Advanced Materials* 18(11) (2006) 1449.
- [28] H.M. Xiong, ZnO Nanoparticles Applied to Bioimaging and Drug Delivery, *Advanced Materials* 25(37) (2013) 5329-5335.
- [29] S.B. Rana, R.P.P. Singh, Investigation of structural, optical, magnetic properties and antibacterial activity of Ni-doped zinc oxide nanoparticles, *Journal of Materials Science-Materials in Electronics* 27(9) (2016) 9346-9355.
- [30] D.J. Norris, A.L. Efros, S.C. Erwin, Doped nanocrystals, *Science* 319(5871) (2008) 1776-1779.
- [31] J.F. Suyver, S.F. Wuister, J.J. Kelly, A. Meijerink, Luminescence of nanocrystalline ZnSe:Mn²⁺, *Physical Chemistry Chemical Physics* 2(23) (2000) 5445-5448.
- [32] R.T. da Silva, A. Mesquita, A.O. de Zevallos, T. Chiamonte, X. Gratens, V.A. Chitta, J.M. Morbec, G. Rahman, V.M. Garcia-Suarez, A.C. Doriguetto, M.I.B. Bernardi, H.B. de Carvalho, Multifunctional nanostructured Co-doped ZnO: Co spatial distribution and correlated magnetic properties, *Physical Chemistry Chemical Physics* 20(30) (2018) 20257-20269.
- [33] G. Gorrasi, A. Sorrentino, Mechanical milling as a technology to produce structural and functional bio-nanocomposites, *Green Chemistry* 17(5) (2015) 2610-2625.
- [34] A.S. Bolokang, F.R. Cummings, B.P. Dhonge, H.M.I. Abdallah, T. Moyo, H.C. Swart, C.J. Arendse, T.F.G. Muller, D.E. Motaung, Characteristics of the mechanical milling on the room temperature ferromagnetism and sensing properties of TiO₂ nanoparticles, *Applied Surface Science* 331 (2015) 362-372.
- [35] S. Kumar, S. Chatterjee, K.K. Chattopadhyay, A.K. Ghosh, Sol-Gel-Derived ZnO:Mn Nanocrystals: Study of Structural, Raman, and Optical Properties, *Journal of Physical Chemistry C* 116(31) (2012) 16700-16708.

- [36] S.B. Rana, Influence of CTAB assisted capping on the structural and optical properties of ZnO nanoparticles, *Journal of Materials Science-Materials in Electronics* 28(18) (2017) 13787-13796.
- [37] R.B.V.D. A.C. Larson, General Structure Analysis System (GSAS), Los Alamos National Laboratory Report LAUR, 1994.
- [38] B. Toby, EXPGUI, a graphical user interface for GSAS, *Journal of Applied Crystallography* 34(2) (2001) 210-213.
- [39] P. Hohenberg, W. Kohn, Inhomogeneous electron gas, *Physical Review B* 136(3B) (1964) B864- B871.
- [40] J.M. Soler, E. Artacho, J.D. Gale, A. Garcia, J. Junquera, P. Ordejon, D. Sanchez-Portal, The SIESTA method for ab initio order-N materials simulation, *Journal of Physics-Condensed Matter* 14(11) (2002) 2745-2779.
- [41] N. Troullier, J.L. Martins, Efficient pseudopotentials for plane-wave calculations, *Physical Review B* 43(3) (1991) 1993-2006.
- [42] J. Han, P. Mantas, A. Senos, Defect chemistry and electrical characteristics of undoped and Mn-doped ZnO, *Journal of the European Ceramic Society* 22(1) (2002) 49-59.
- [43] G.D. Mahan, Intrinsic defects in zno varistors, *Journal of Applied Physics* 54(7) (1983) 3825-3832.
- [44] A.C.S. Sabioni, About the oxygen diffusion mechanism in ZnO, *Solid State Ionics* 170(1-2) (2004) 145-148.
- [45] M. McCluskey, S. Jokela, Defects in ZnO, *Journal of Applied Physics* 106(7) (2009).
- [46] A. Mesquita, F.P. Rhodes, R.T. da Silva, P.P. Neves, A.O. de Zevallos, M.R.B. Andreta, M.M. de Lima, A. Cantarero, I.S. da Silva, M.A. Boselli, X. Gratens, V.A. Chitta, A.C. Doriguetto, W.B. Ferraz, A.C.S. Sabioni, H.B. de Carvalho, Dynamics of the incorporation of Co into the wurtzite ZnO matrix and its magnetic properties, *Journal of Alloys and Compounds* 637 (2015) 407-417.
- [47] P. Bonasewicz, W. Hirschwald, G. Neumann, Influence of surface processes on electrical, photochemical, and thermodynamical properties of zinc-oxide films, *Journal of the Electrochemical Society* 133(11) (1986) 2270-2278.
- [48] M.W. Barsoum, *Fundamentals of ceramics*, Taylor & Francis, New York; London, 2003.
- [49] J. Jiang, L.C. Li, Synthesis of sphere-like Co₃O₄ nanocrystals via a simple polyol route, *Materials Letters* 61(27) (2007) 4894-4896.
- [50] A.C.S. Sabioni, A. Daniel, R. Metz, A.M. Huntz, F. Jomard, First study of oxygen diffusion in a ZnO-based commercial varistor, *Defect and Diffusion Forum* 289-292 (2009) 339-345.
- [51] R.D. Shannon, Revised effective ionic radii and systematic studies of interatomic distances in halides and chalcogenides, *Acta Crystallographica Section A* 32(5) (1976) 751-767.
- [52] S. Kolesnik, B. Dabrowski, J. Mais, Structural and magnetic properties of transition metal substituted ZnO, *Journal of Applied Physics* 95(5) (2004) 2582-2586.
- [53] J. M. Calleja, M. Cardona, Resonant Raman Scattering in ZnO, *Physical Review B* 16(8) (1977) 3753-3761.

- [54] M. Schumm, M. Koerdel, S. Müller, H. Zutz, C. Ronning, J. Stehr, D.M. Hofmann, J. Geurts, Structural impact of Mn implantation on ZnO, *New Journal of Physics* 10(4) (2008) 043004.
- [55] B. Sanches de Lima, P.R. Martínez-Alanis, F. Güell, W.A. dos Santos Silva, M.I.B. Bernardi, N.L. Marana, E. Longo, J.R. Sambrano, V.R. Mastelaro, Experimental and Theoretical Insights into the Structural Disorder and Gas Sensing Properties of ZnO, *ACS Applied Electronic Materials* 3(3) (2021) 1447-1457.
- [56] L.R. Valerio, N.C. Mamani, A.O. de Zevallos, A. Mesquita, M.I.B. Bernardi, A.C. Doriguetto, H.B. de Carvalho, Preparation and structural-optical characterization of dip-coated nanostructured Co-doped ZnO dilute magnetic oxide thin films, *Rsc Advances* 7(33) (2017) 20611-20619.
- [57] P. Koidl, Optical-absorption of Co^{2+} in ZnO, *Physical Review B* 15(5) (1977) 2493-2499.
- [58] K. Wang, Q.B. Yu, Q. Qin, W.J. Duan, Feasibility of a Co Oxygen Carrier for Chemical Looping Air Separation: Thermodynamics and Kinetics, *Chemical Engineering & Technology* 37(9) (2014) 1500-1506.
- [59] M.I. Mendelson, Average grain size in polycrystalline ceramics, *Journal of the American Ceramic Society* 52(8) (1969) 443-446.
- [60] T. Senda, R.C. Bradt, Grain Growth in Sintered ZnO and ZnO-Bi₂O₃ Ceramics, *Journal of the American Ceramic Society* 73(1) (1990) 106-114.
- [61] R.M. German, Chapter Seven - Thermodynamic and Kinetic Treatments, in: R.M. German (Ed.), *Sintering: from Empirical Observations to Scientific Principles*, Butterworth-Heinemann, Boston, 2014, pp. 183-226.
- [62] O.J. Whittemore, J.A. Varela, Initial sintering of ZnO, *Journal of the American Ceramic Society* 64(11) (1981) C154-C155.
- [63] S.-D. Shin, C.-S. Sone, J.-H. Han, D.-Y. Kim, Effect of Sintering Atmosphere on the Densification and Abnormal Grain Growth of ZnO, *Journal of the American Ceramic Society* 79(2) (1996) 565-567.
- [64] J. Han, P.Q. Mantas, A.M.R. Senos, Grain growth in Mn-doped ZnO, *Journal of the European Ceramic Society* 20(16) (2000) 2753-2758.
- [65] G. Hardal, B.Y. Price, The Effect of TiO₂ and B₂O₃ Additions on the Grain Growth of ZnO, *Metallurgical and Materials Transactions a-Physical Metallurgy and Materials Science* 48A(4) (2017) 2090-2098.
- [66] S. Roy, T.K. Roy, D. Das, Grain growth kinetics of Er₂O₃ doped ZnO-V₂O₅ based varistor ceramics, *Ceramics International* 45(18) (2019) 24835-24850.

SUPPLEMENTARY DATA

5 **A comprehensive study on the processing Co:ZnO ceramics: defect
engineering and grain growth kinetics**

R. T. da Silva^a, J. M. Morbec^{b‡}, G. Rahman^{c†}, and H. B. de Carvalho^{d*}

10 ^a *Universidade Federal de Ouro Preto – UFOP, 35400-000 Ouro Preto, MG, Brazil.*

^b *School of Chemical and Physical Sciences, Keele University, Keele ST5 5BG, United Kingdom*

^c *Department of Physics, Quaid-i-Azam University, 45320 Islamabad, Pakistan.*

^d *Universidade Federal de Alfenas - UNIFAL, 37130-000 Alfenas, Brazil.*

15 *Corresponding Authors:*

‡ j.morbec@keele.ac.uk

† gulrahman@qau.edu.pk.

* hugo.carvalho@unifal-mg.edu.br.

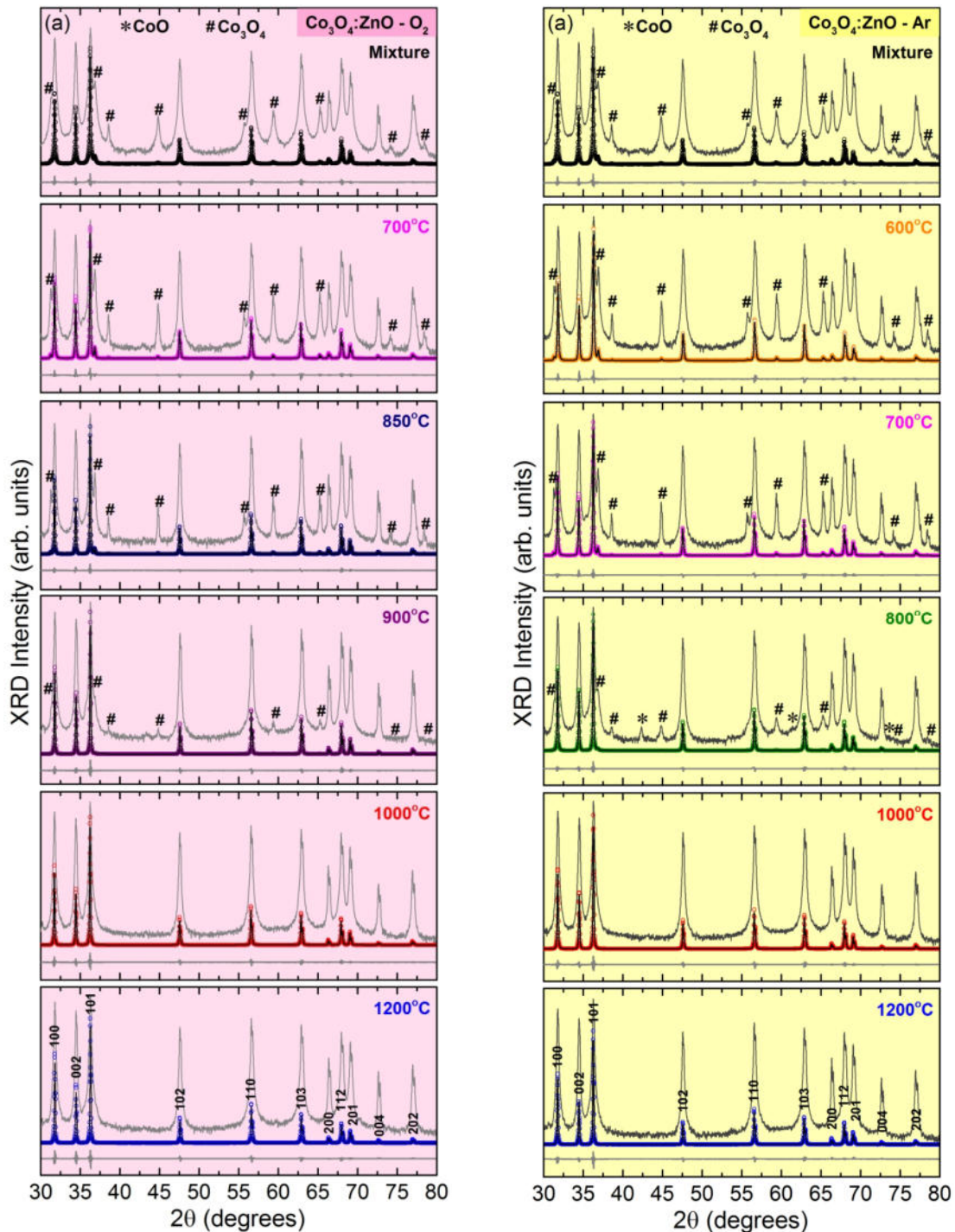


Figure S1. Refined XRD diffractograms of $\text{Co}_3\text{O}_4:\text{ZnO}$ samples (8 at.%) synthesized at different temperatures in atmosphere of (a) oxygen and (b) argon. Each figure shows the observed pattern (symbols) and in a log scale (solid gray line), Rietveld calculated pattern (solid line), and the goodness of the fit or residual pattern (at the bottom). Diffraction peak associated with Co_3O_4 were indicated by the symbol (#).

Table S1 - Elemental occupation factor for the Zn, Co (effective concentration, x_E) and O present in the $\text{Co}_3\text{O}_4\text{:ZnO}$ wurtzite structure and the fractions of the ZnO, CoO e Co_3O_4 obtained through Rietveld refinement.

	Sample	Zn	Co	O	$f. \text{ZnO}$	$f. \text{CoO}$	$f. \text{Co}_3\text{O}_4$	
$\text{Co}_3\text{O}_4\text{:ZnO}$	Oxygen	Mixture	1.000(1)	-	0.980(5)	0.9221	-	0.0778
		600 °C	0.998(1)	0.002(1)	0.981(4)	0.9227	-	0.0773
		700 °C	0.990(1)	0.010(1)	0.978(5)	0.9301	-	0.0699
		800 °C	0.982(1)	0.018(1)	0.986(4)	0.9375	-	0.0625
		850 °C	0.962(1)	0.039(1)	0.986(4)	0.9571	-	0.0428
		900 °C	0.925(1)	0.075(1)	0.985(4)	0.9954	-	0.0046
		1000 °C	0.926(1)	0.080(1)	0.992(4)	1.000	-	-
		1200 °C	0.922(1)	0.080(1)	0.991(5)	1.000	-	-
	Argon	Mixture	1.000(1)	-	0.980(5)	0.9221	-	0.0778
		600 °C	0.992(1)	0.008(1)	0.987(4)	0.9280	-	0.0720
		700 °C	0.975(1)	0.026(1)	0.983(4)	0.9451	-	0.0549
		800 °C	0.935(1)	0.065(1)	0.981(4)	0.9831	-	0.0169
		1000 °C	0.921(1)	0.081(1)	0.984(4)	1.000	-	-
		1200 °C	0.919(1)	0.079(1)	0.972(5)	1.000	-	-

5

Table S2 - Structural data (a and c) for the $\text{Co}_3\text{O}_4\text{:ZnO}$ samples obtained through the Rietveld refinement. V is the cell volume, χ^2 is the square of the goodness-of-fit indicator, and R_{Bragg} is the refinement quality parameter.

	Sample	a (Å)	c (Å)	V (Å ³)	χ^2	R_{Bragg}	
$\text{Co}_3\text{O}_4\text{:ZnO}$	Oxygen	Mixture	3.25095(1)	5.20885(3)	47.675(1)	6.9	4.6
		600 °C	3.25105(1)	5.20868(3)	47.677(1)	3.7	2.9
		700 °C	3.25142(1)	5.20855(3)	47.686(1)	4.0	4.7
		800 °C	3.25186(1)	5.20736(2)	47.688(1)	3.2	2.8
		850 °C	3.25229(1)	5.20737(2)	47.701(1)	2.5	3.1
		900 °C	3.25295(1)	5.20579(2)	47.706(1)	4.3	3.2
		1000 °C	3.25359(1)	5.20482(2)	47.716(1)	4.2	2.2
		1200 °C	3.25288(1)	5.20709(3)	47.716(1)	6.6	3.6
	Argon	Mixture	3.25095(1)	5.20885(3)	47.675(1)	6.9	4.6
		600 °C	3.25118(1)	5.20877(3)	47.681(1)	4.1	5.4
		700 °C	3.25168(1)	5.20792(2)	47.688(1)	3.0	2.6
		800 °C	3.25253(2)	5.20689(3)	47.706(1)	3.7	2.6
		1000 °C	3.25353(1)	5.20502(2)	47.716(1)	4.7	2.3
		1200 °C	3.25304(1)	5.20663(3)	47.716(1)	5.2	5.0

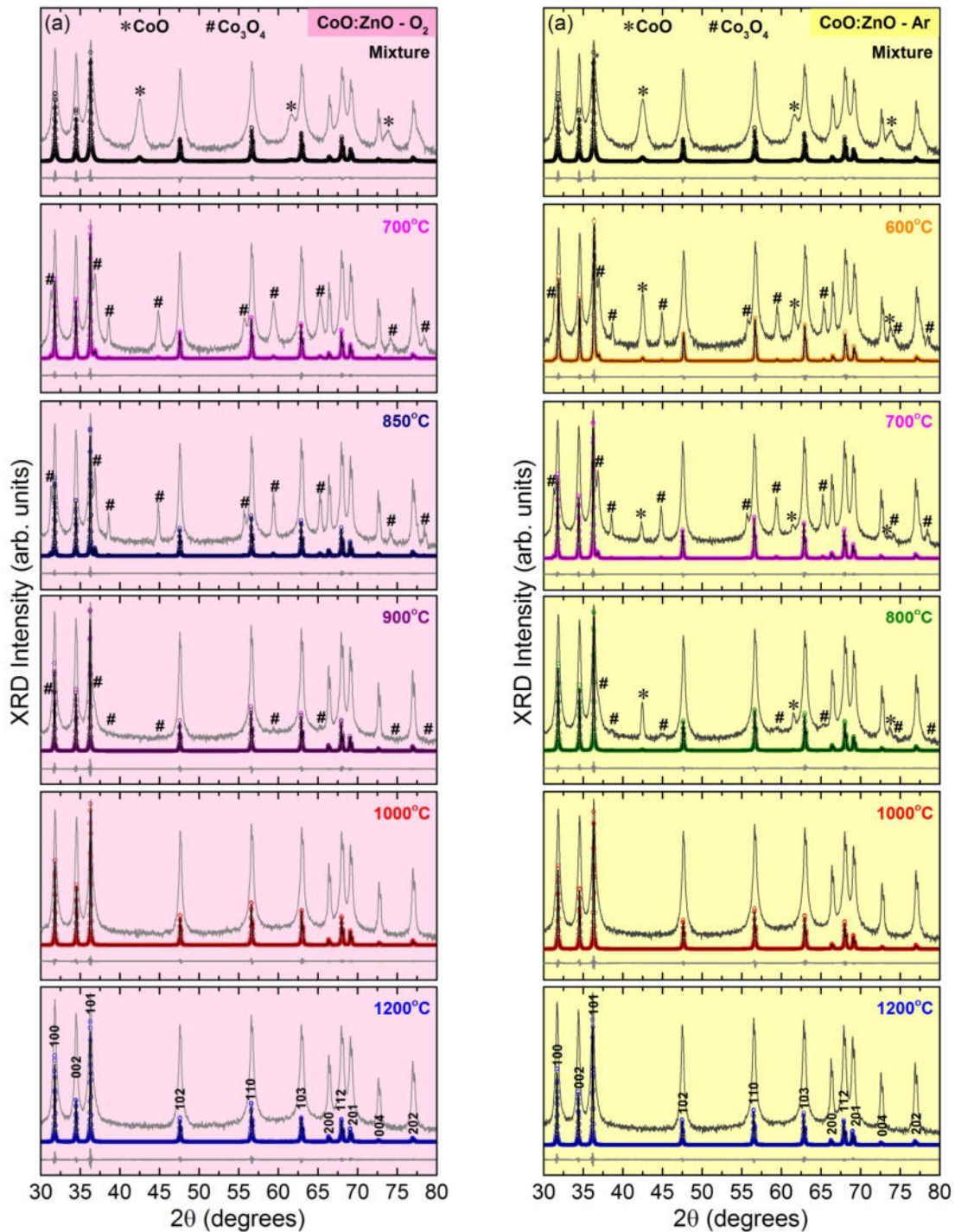


Figure S2. Refined XRD diffractograms of **CoO:ZnO** samples (8 at.%) synthesized at different temperatures in atmosphere of (a) oxygen and (b) argon. Each figure shows the observed pattern (symbols) and in a log scale (solid gray line), Rietveld calculated pattern (solid line), and the goodness of the fit or residual pattern (at the bottom). Diffraction peaks associated with CoO and Co_3O_4 were indicated by the symbol (*) and (#), respectively.

Table S3 - Elemental occupation factor for the Zn, Co (effective concentration, x_E) and O present in the **CoO:ZnO** wurtzite structure and the fractions of the ZnO, CoO e Co₃O₄ obtained through Rietveld refinement.

	Sample	Zn	Co	O	<i>f.</i> ZnO	<i>f.</i> CoO	<i>f.</i> Co ₃ O ₄	
CoO:ZnO	Oxygen	Mixture	1.000(1)	-	0.985(7)	0.9258	0.0742	-
		600 °C	0.998(1)	0.002(1)	0.981(4)	0.9225	-	0.0775
		700 °C	0.992(1)	0.008(1)	0.987(5)	0.9283	-	0.0717
		800 °C	0.981(1)	0.019(1)	0.984(4)	0.9389	-	0.0611
		850 °C	0.960(1)	0.040(1)	0.981(4)	0.9583	-	0.0417
		900 °C	0.922(1)	0.078(1)	0.978(4)	0.9987	-	0.0013
		1000 °C	0.921(1)	0.080(1)	0.986(4)	1.000	-	-
		1200 °C	0.919(1)	0.079(1)	0.995(4)	1.000	-	-
	Argon	Mixture	1.000(1)	-	0.985(7)	0.9258	0.0742	-
		600 °C	0.996(1)	0.007(1)	0.972(5)	0.9285	0.0327	0.0388
		700 °C	0.977(1)	0.023(1)	0.982(4)	0.9425	0.0064	0.0510
		800 °C	0.935(1)	0.067(1)	0.985(4)	0.9878	0.0122	-
		1000 °C	0.921(1)	0.078(1)	0.977(4)	1.000	-	-
		1200 °C	0.920(1)	0.077(1)	0.978(4)	1.000	-	-

5

Table S4 - Structural data (*a* and *c*) for the **CoO:ZnO** samples obtained through the Rietveld refinement. *V* is the cell volume, χ^2 is the square of the goodness-of-fit indicator, and R_B is the refinement quality parameter.

	Sample	<i>a</i> (Å)	<i>c</i> (Å)	<i>V</i> (Å ³)	χ^2	R_{Bragg}	
CoO:ZnO	Oxygen	Mixture	3.25094(2)	5.20837(1)	47.674(1)	5.8	6.8
		600 °C	3.25098(1)	5.20866(3)	47.674(1)	4.2	2.8
		700 °C	3.25129(1)	5.20818(3)	47.679(1)	4.3	5.2
		800 °C	3.25185(1)	5.20732(2)	47.688(1)	5.3	4.8
		850 °C	3.25205(1)	5.20789(2)	47.699(1)	3.7	5.5
		900 °C	3.25314(1)	5.20553(2)	47.709(1)	5.2	2.7
		1000 °C	3.25376(1)	5.20429(2)	47.716(1)	3.2	2.0
		1200 °C	3.25293(1)	5.20690(3)	47.715(1)	6.3	3.5
	Argon	Mixture	3.25094(2)	5.20837(1)	47.674(1)	5.8	6.8
		600 °C	3.25108(1)	5.20850(3)	47.676(1)	2.7	5.2
		700 °C	3.25157(1)	5.20766(2)	47.683(1)	3.4	2.5
		800 °C	3.25269(1)	5.20679(2)	47.708(1)	3.6	2.4
	1000 °C	3.25356(1)	5.20487(3)	47.715(1)	4.8	2.4	
	1200 °C	3.25323(1)	5.20604(2)	47.716(1)	4.7	2.9	

10

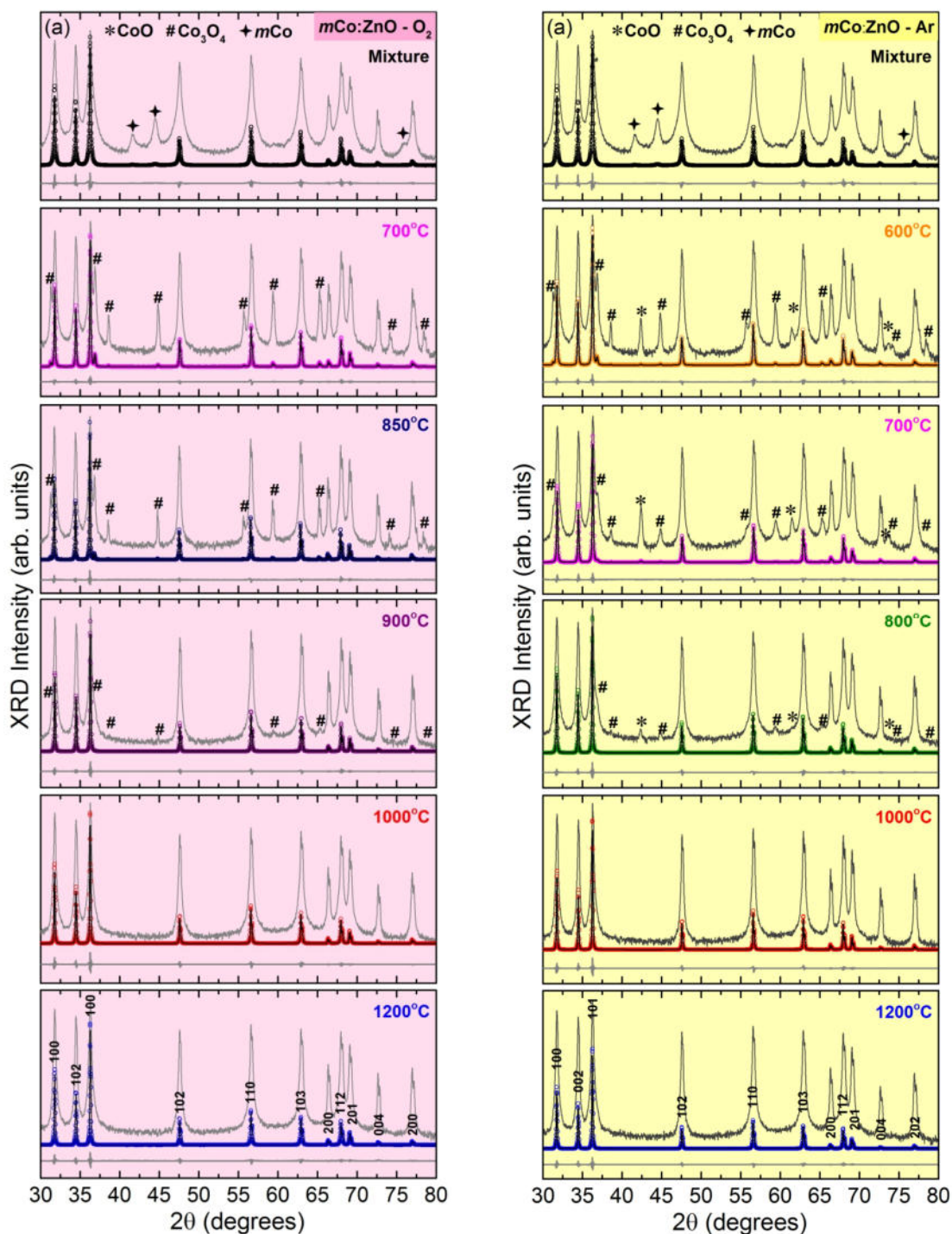


Figure S3 - Refined XRD diffractograms of *mCo:ZnO* samples (8 at.%) synthesized at different temperatures in atmosphere of (a) oxygen and (b) argon. Each figure shows the observed pattern (symbols) and in a log scale (solid gray line), Rietveld calculated pattern (solid line), and the goodness of the fit or residual pattern (at the bottom). Diffraction peaks associated with metallic Co, CoO and Co_3O_4 were indicated by the symbol (+), (*) and (#), respectively.

Table S1 - Elemental occupation factor for the Zn, Co (effective concentration, x_E) and O present in the $m\text{Co}:\text{ZnO}$ wurtzite structure and the fractions of the ZnO, CoO, Co₃O₄ and metallic Co obtained through Rietveld refinement.

	Sample	Zn	Co	O	<i>f.</i> ZnO	<i>f.</i> CoO	<i>f.</i> Co ₃ O ₄	<i>f.</i> Co
<i>m</i> CoO:ZnO	Mixture	0.997(1)	-	0.977(6)	0.9426	-	-	0.0573
	600 °C	0.997(1)	0.005(1)	0.978(5)	0.9236	-	0.0764	
	700 °C	0.990(1)	0.010(1)	0.977(5)	0.9305	-	0.0695	
	800 °C	0.984(1)	0.016(1)	0.986(4)	0.9371	-	0.0629	
	850 °C	0.960(1)	0.040(1)	0.987(4)	0.9591	-	0.0409	
	900 °C	0.922(1)	0.078(1)	0.984(4)	0.9986	-	0.0014	
	1000 °C	0.920(1)	0.080(1)	0.992(5)	1.000	-	-	
	1200 °C	0.921(1)	0.080(1)	0.992(5)	1.000	-	-	
	Mixture	0.997(1)	-	0.977(6)	0.9426	-	-	0.0573
	500 °C	0.996(1)	0.004(1)	0.977(4)	0.9267	0.0113	0.0589	0.0029
	600 °C	0.991(1)	0.011(1)	0.973(4)	0.9318	0.0096	0.0586	-
	700 °C	0.959(1)	0.042(1)	0.986(4)	0.9593	0.0195	0.0211	-
	800 °C	0.929(1)	0.071(1)	0.984(4)	0.9904	0.0064	0.0032	-
	1000 °C	0.920(1)	0.079(1)	0.974(4)	1.000	-	-	
1200 °C	0.921(1)	0.080(1)	0.971(4)	1.000	-	-		

Table S6 - Elemental occupation factor for the Zn, Co (effective concentration, x_E) and O present in the $m\text{Co}:\text{ZnO}$ wurtzite structure and the fractions of the ZnO, CoO, Co₃O₄ and metallic Co obtained through Rietveld refinement.

	Sample	<i>a</i> (Å)	<i>c</i> (Å)	<i>V</i> (Å ³)	χ^2	<i>R</i> _{Bragg}
<i>m</i> CoO:ZnO	Mixture	3.25105(2)	5.20886(5)	47.677(1)	8.4	4.6
	600 °C	3.25108(1)	5.20856(3)	47.677(1)	4.8	7.1
	700 °C	3.25137(1)	5.20817(3)	47.682(1)	6.4	7.5
	800 °C	3.25202(1)	5.20671(2)	47.687(1)	5.3	7.2
	850 °C	3.25248(1)	5.20685(2)	47.702(1)	3.0	3.1
	900 °C	3.25319(1)	5.20532(2)	47.708(1)	4.4	2.3
	1000 °C	3.25358(1)	5.20490(3)	47.716(1)	5.6	2.3
	1200 °C	3.25328(1)	5.20586(3)	47.716(1)	4.7	3.5
	Mixture	3.25105(2)	5.20886(5)	47.677(1)	8.4	4.6
	500 °C	3.25107(1)	5.20868(3)	47.677(1)	4.6	4.7
	600 °C	3.25130(1)	5.20873(3)	47.684(1)	4.1	4.4
	700 °C	3.25190(1)	5.20756(2)	47.691(1)	3.3	2.1
	800 °C	3.25269(1)	5.20656(2)	47.705(1)	4.2	2.2
	1000 °C	3.25356(1)	5.20491(2)	47.716(1)	4.7	2.7
1200 °C	3.25355(1)	5.20508(3)	47.717(1)	4.1	2.6	

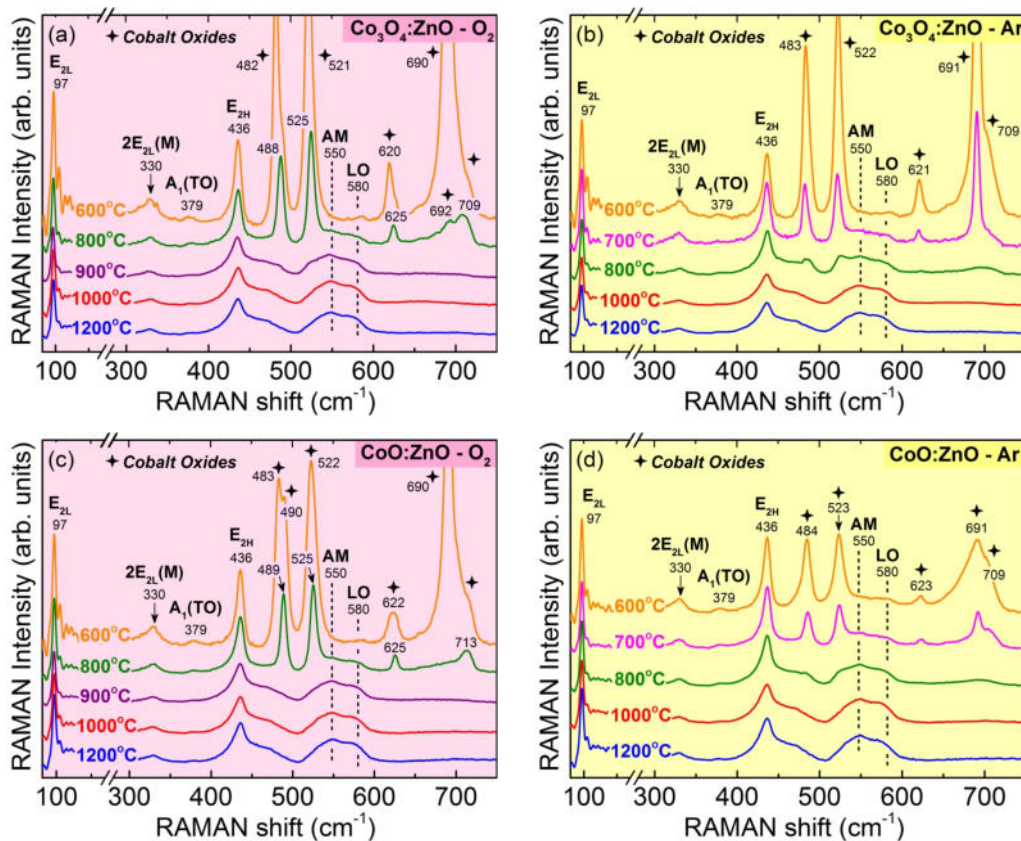


Figure S4. Raman scattering spectra obtained at room temperature for the samples (a) Co₃O₄:ZnO in O₂; (b) Co₃O₄:ZnO in Ar; (c) CoO:ZnO in O₂ and (d) CoO:ZnO in Ar. The spectra were acquired at room temperature and are normalized by integrated area of the E_{2H} vibrational mode obtained by gaussian fit of the spectra.

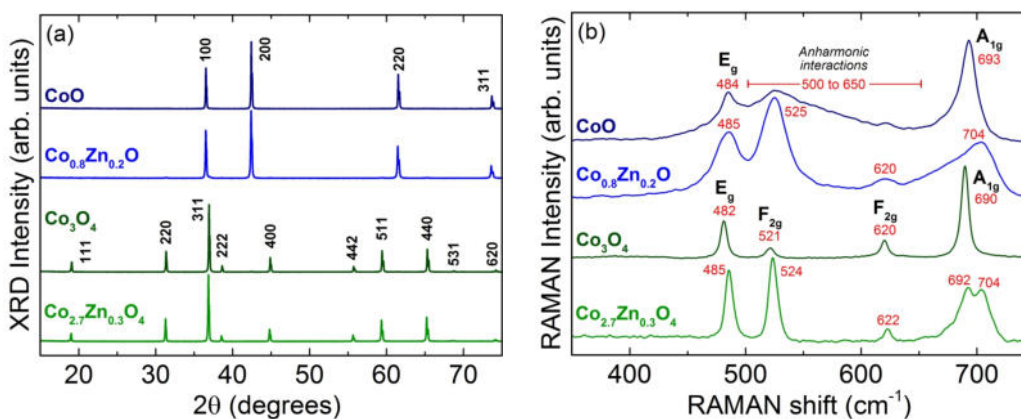


Figure S5. (a) X-ray diffraction patterns and (b) Raman scattering spectra obtained at room temperature for the CoO, Co_{0.8}Zn_{0.2}O (20 at.% Zn-doped CoO), Co₃O₄, and Co_{0.24}Zn_{0.6}O (10 at.% Zn-doped Co₃O₄).

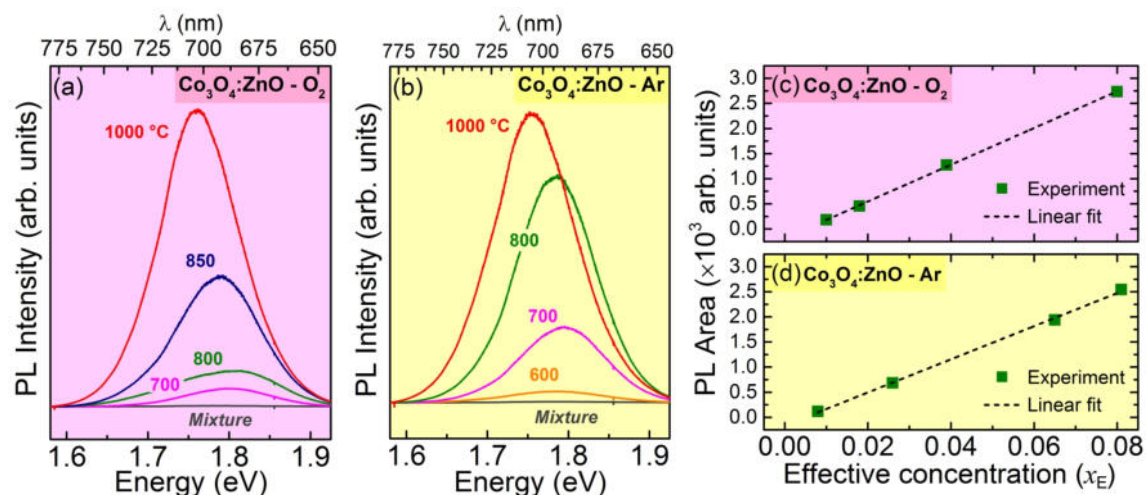


Figure S6. Room temperature PL spectra for part of the $\text{Co}_3\text{O}_4:\text{ZnO}$ set of samples prepared in (a) oxygen (O_2) and (b) argon (Ar) atmospheres. It was used a 532 nm laser for excitation with optical power density of $50 \text{ kW}/\text{cm}^2$. Integrated area underneath the spectra plotted as a function of the calculated effective cobalt concentration (x_E) for the samples prepared (c) O_2 and in (d) Ar .

10

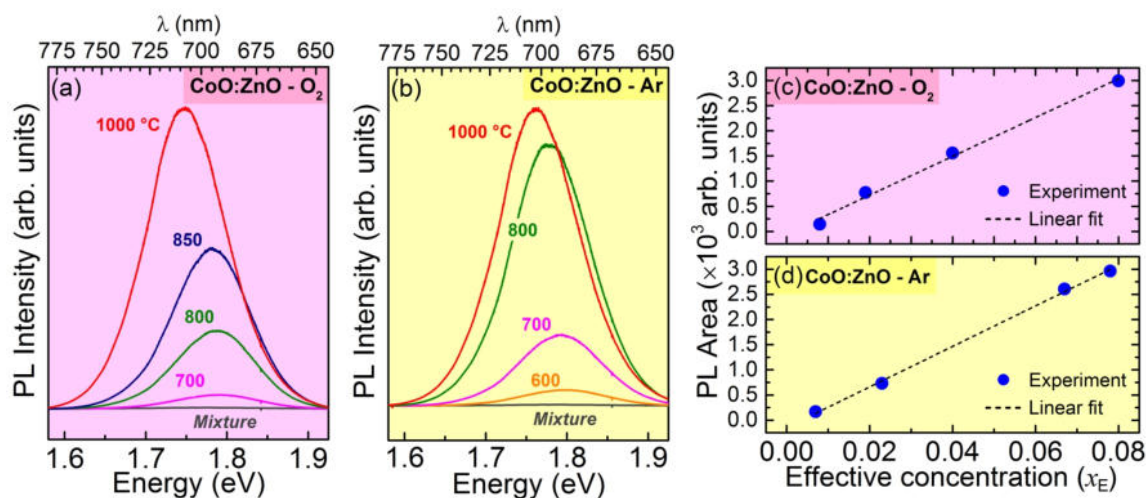


Figure S7. Room temperature PL spectra for part of the $\text{CoO}:\text{ZnO}$ set of samples prepared in (a) oxygen (O_2) and (b) argon (Ar) atmospheres. It was used a 532 nm laser for excitation with optical power density of $50 \text{ kW}/\text{cm}^2$. Integrated area underneath the spectra plotted as a function of the calculated effective cobalt concentration (x_E) for the samples prepared (c) O_2 and in (d) Ar .

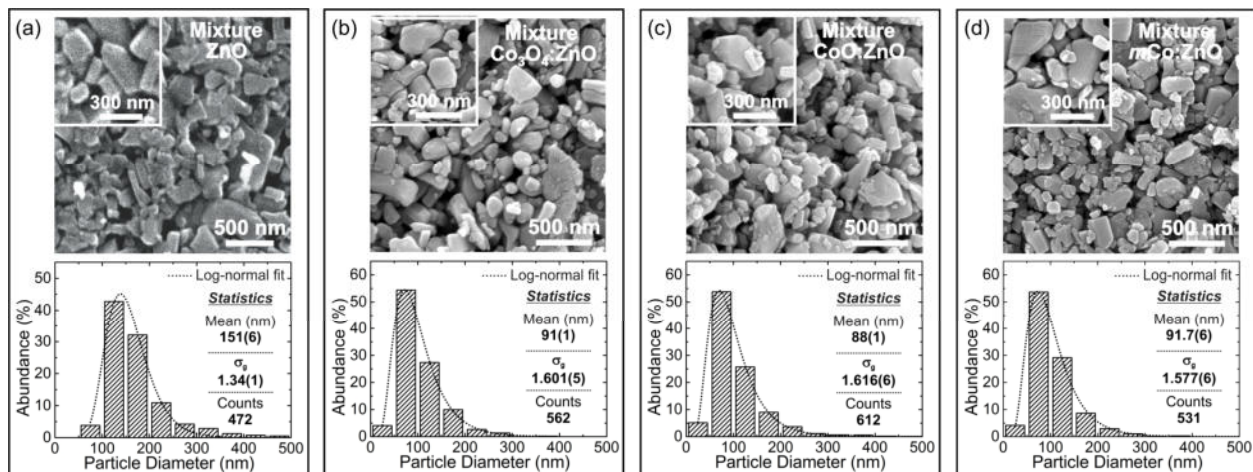


Figure S8. Representative SEM micrographs and obtained grain size statistical histograms for the powder mixtures (a) ZnO pure, (b) $\text{Co}_3\text{O}_4:\text{ZnO}$, (c) $\text{CoO}:\text{ZnO}$ and (d) $m\text{Co}:\text{ZnO}$, before the heat treatments.

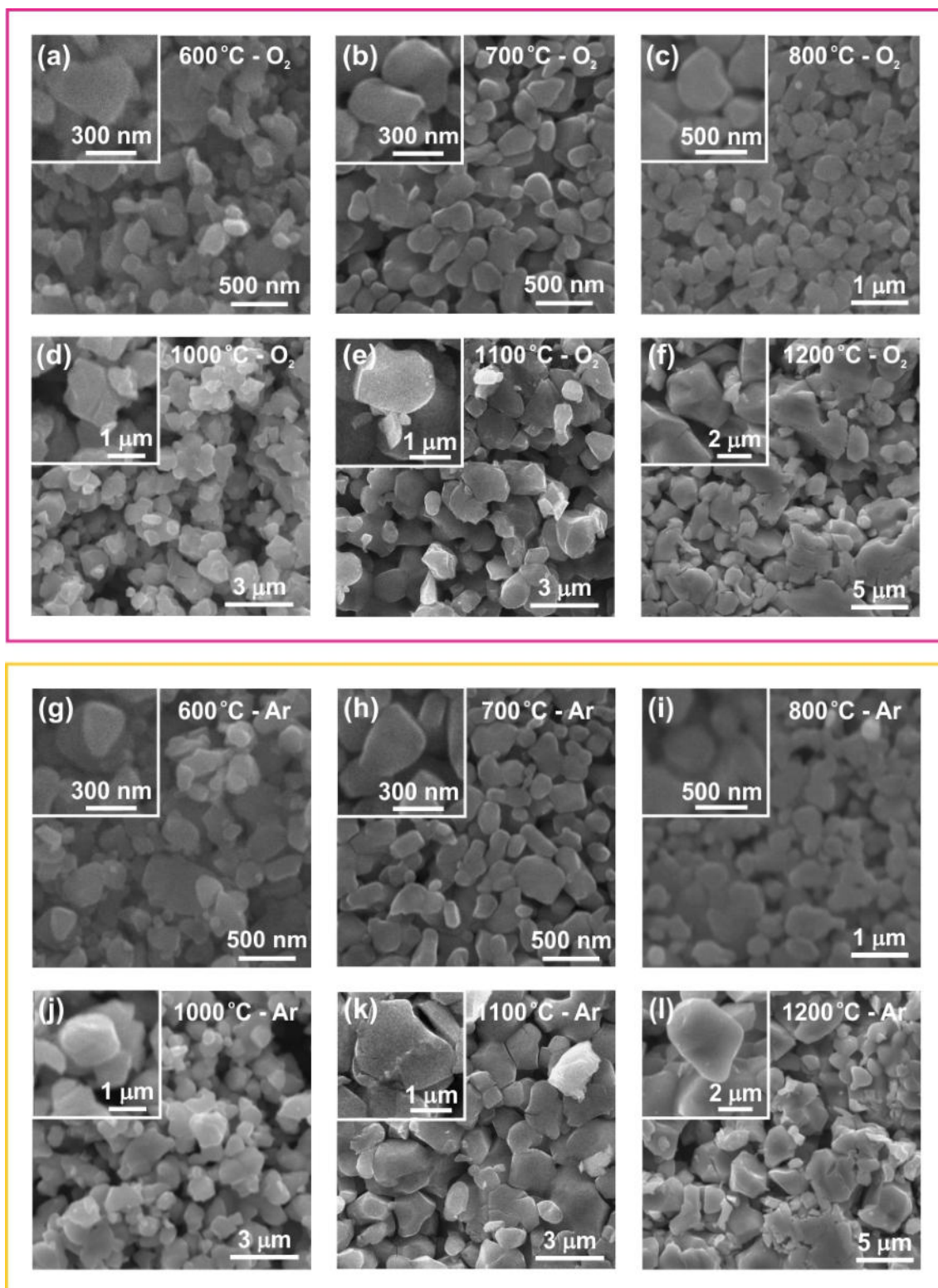


Figure S9 - Representative images by scanning electron microscopy of the surfaces of **ZnO** samples heat treated in O₂ at (a) 600 °C, (b) 700 °C, (c) 800 °C, (d) 1000 °C, (e) 1100 °C, (f) 1200 °C, and in Ar at (g) 600 °C, (h) 700 °C, (i) 800 °C, (j) 1000 °C, (k) 1100 °C, and (l) 1200 °C.

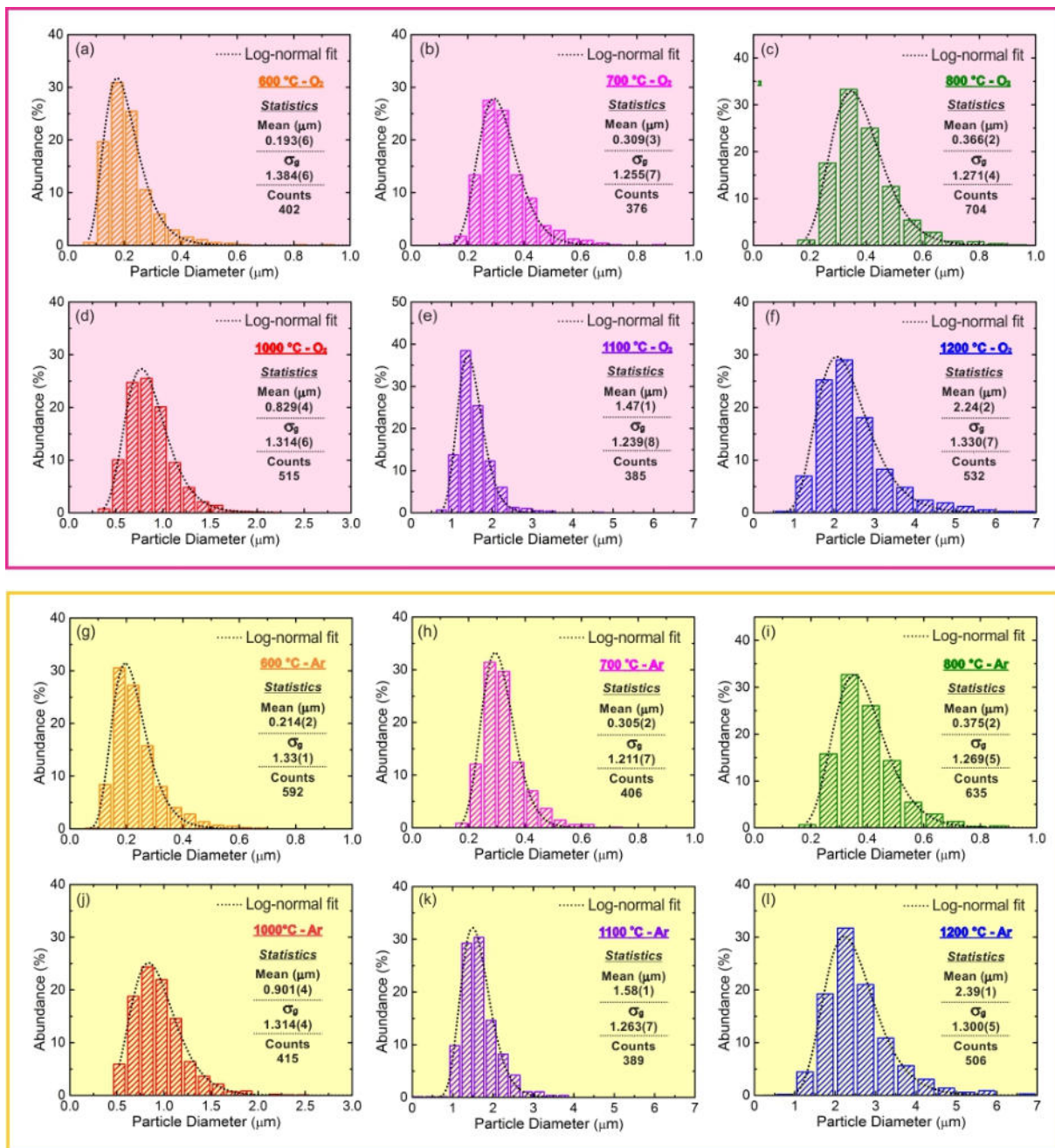


Figure S10 - Particle size distribution histograms of the **ZnO** samples heat treated in O₂ at (a) 600 °C, (b) 700 °C, (c) 800 °C, (d) 1000 °C, (e) 1100 °C, (f) 1200 °C, and in Ar at (g) 600 °C, (h) 700 °C, (i) 800 °C, (j) 1000 °C, (k) 1100 °C, and (l) 1200 °C. The distribution statistic obtained after log-normal fit is also presented in the panels.

Table S7 - Particle size distribution analyses of the **ZnO** samples. L is the mean value of the particle diameter and σ_g is the geometric standard deviation obtained by the log-normal fit of particle size distribution histograms for each sample. N is the total number of counted particles.

		Sample	L (μm)	σ_g	N
ZnO	Oxygen	Mixture	0.151(6)	1.34(1)	472
		600 °C	0.193(1)	1.384(6)	402
		700 °C	0.309(3)	1.255(7)	376
		800 °C	0.366(2)	1.271(4)	704
		1000 °C	0.829(4)	1.314(6)	515
		1100 °C	1.47(1)	1.239(8)	385
		1200 °C	2.24(2)	1.330(7)	532
		Mixture	0.151(6)	1.34(1)	472
	Argon	600 °C	0.214(2)	1.33(1)	592
		700 °C	0.305(2)	1.211(7)	406
		800 °C	0.375(2)	1.269(5)	635
		1000 °C	0.901(4)	1.314(4)	415
		1100 °C	1.58(1)	1.263(7)	389
		1200 °C	2.39(1)	1.300(5)	506

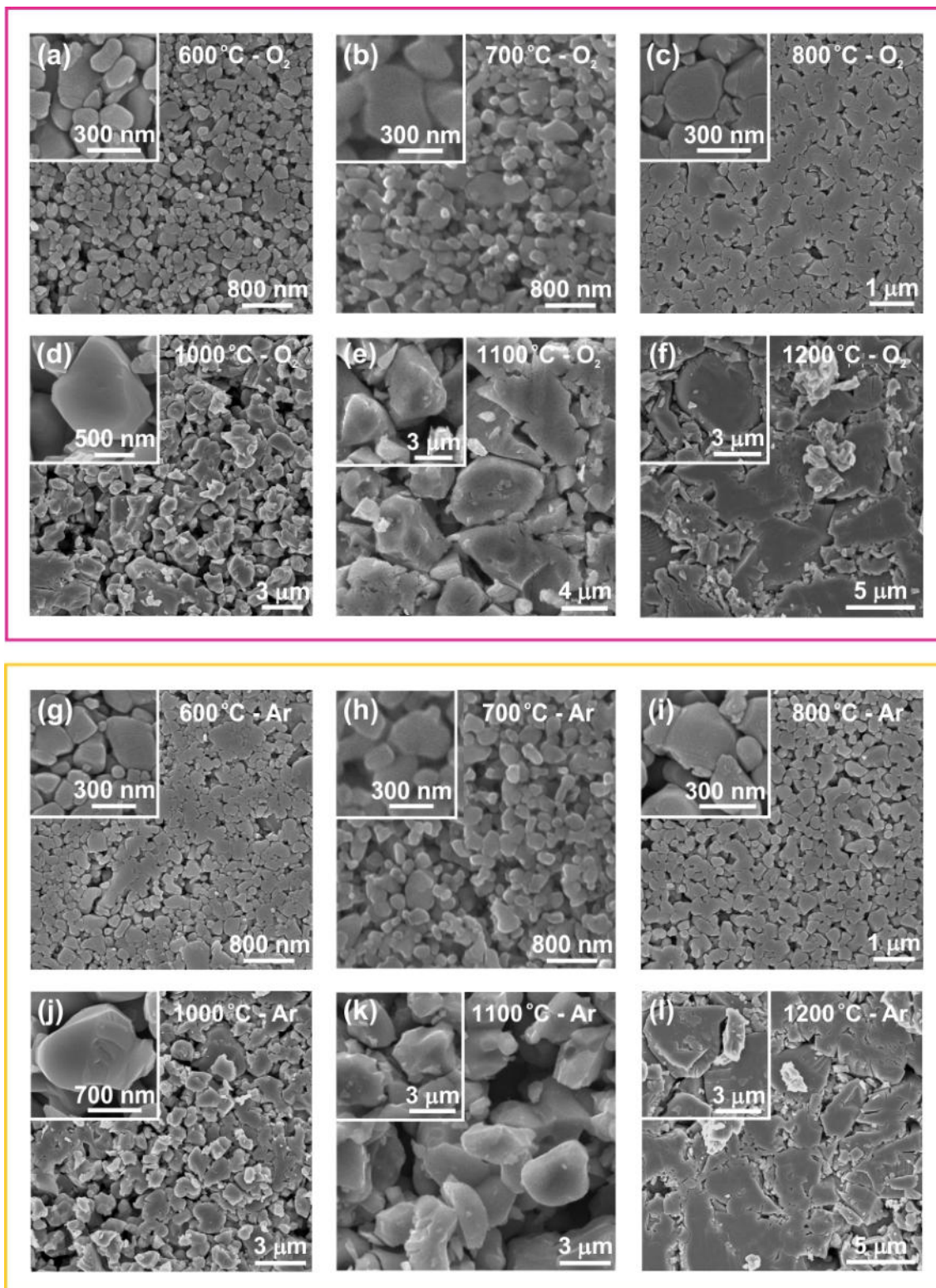


Figure S11 - Representative images by scanning electron microscopy of the surfaces of $\text{Co}_3\text{O}_4:\text{ZnO}$ samples heat treated in O_2 at (a) 600 °C, (b) 700 °C, (c) 800 °C, (d) 1000 °C, (e) 1100 °C, (f) 1200 °C, and in Ar at (g) 600 °C, (h) 700 °C, (i) 800 °C, (j) 1000 °C, (k) 1100 °C, and (l) 1200 °C.

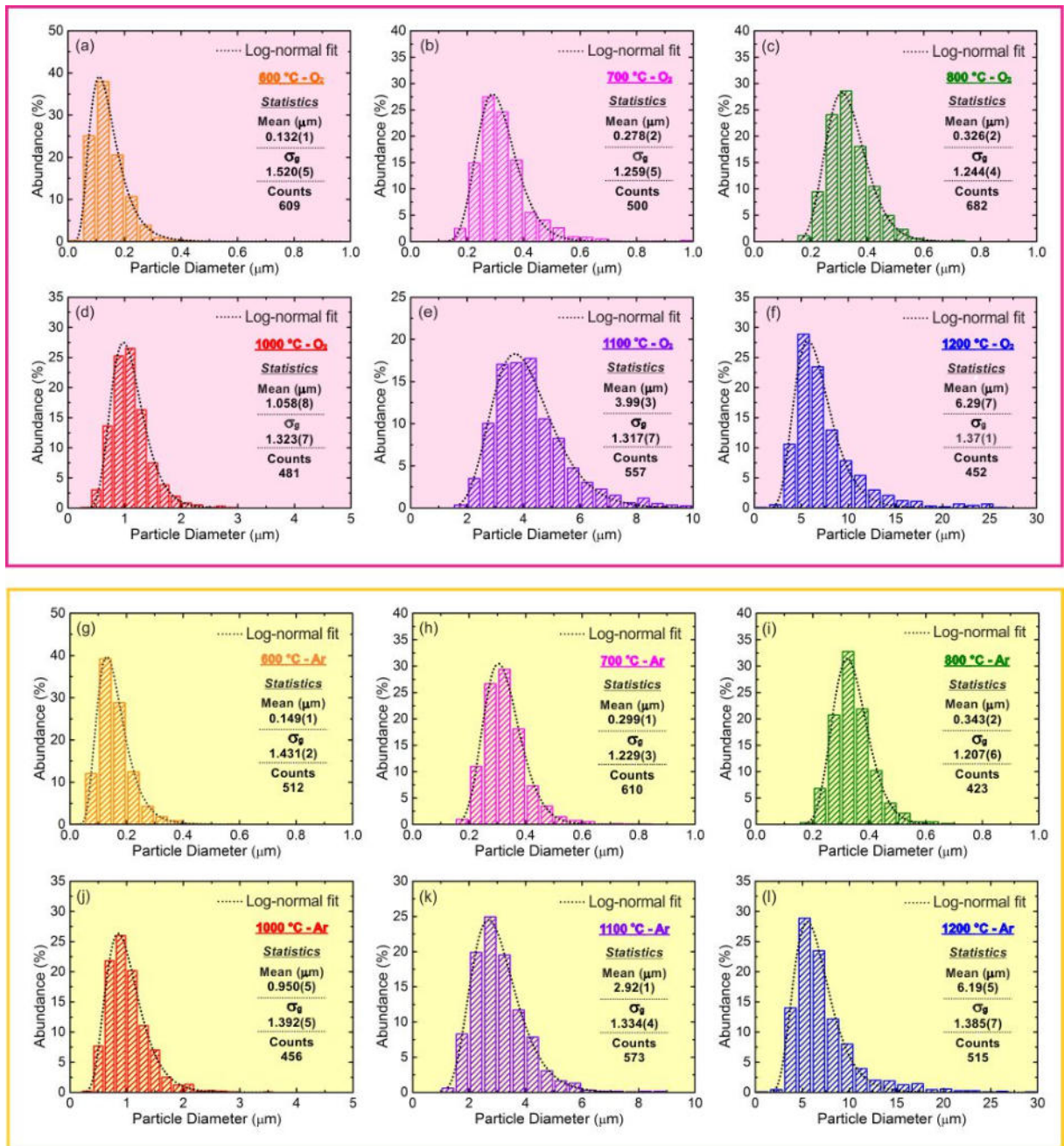


Figure S12 - Particle size distribution histograms of the $\text{Co}_3\text{O}_4:\text{ZnO}$ samples heat treated in O_2 at (a) 600 °C, (b) 700 °C, (c) 800 °C, (d) 1000 °C, (e) 1100 °C, (f) 1200 °C, and in Ar at (g) 600 °C, (h) 700 °C, (i) 800 °C, (j) 1000 °C, (k) 1100 °C, and (l) 1200 °C. The distribution statistic obtained after log-normal fit is also presented in the panels.

Table S8 - Particle size distribution analyses of the **Co₃O₄:ZnO** samples. L is the mean value of the particle diameter and σ_g is the geometric standard deviation obtained by the log-normal fit of particle size distribution histograms for each sample. N is the total number of counted particles.

		Sample	$L(\mu\text{m})$	σ_g	N
Co₃O₄:ZnO	<i>Oxygen</i>	Mixture	0.091(1)	1.601(5)	562
		600 °C	0.132(1)	1.520(5)	609
		700 °C	0.278(2)	1.259(5)	500
		800 °C	0.326(2)	1.244(4)	682
		1000 °C	1.058(8)	1.323(7)	481
		1100 °C	3.99(3)	1.317(7)	557
		1200 °C	6.29(7)	1.37(1)	452
		<i>Argon</i>	Mixture	0.091(1)	1.601(5)
	600 °C		0.149(1)	1.431(2)	512
	700 °C		0.299(1)	1.229(3)	610
	800 °C		0.343(2)	1.207(6)	423
	1000 °C		0.950(5)	1.392(5)	456
	1100 °C		2.92(1)	1.334(4)	573
	1200 °C		6.19(5)	1.385(7)	515

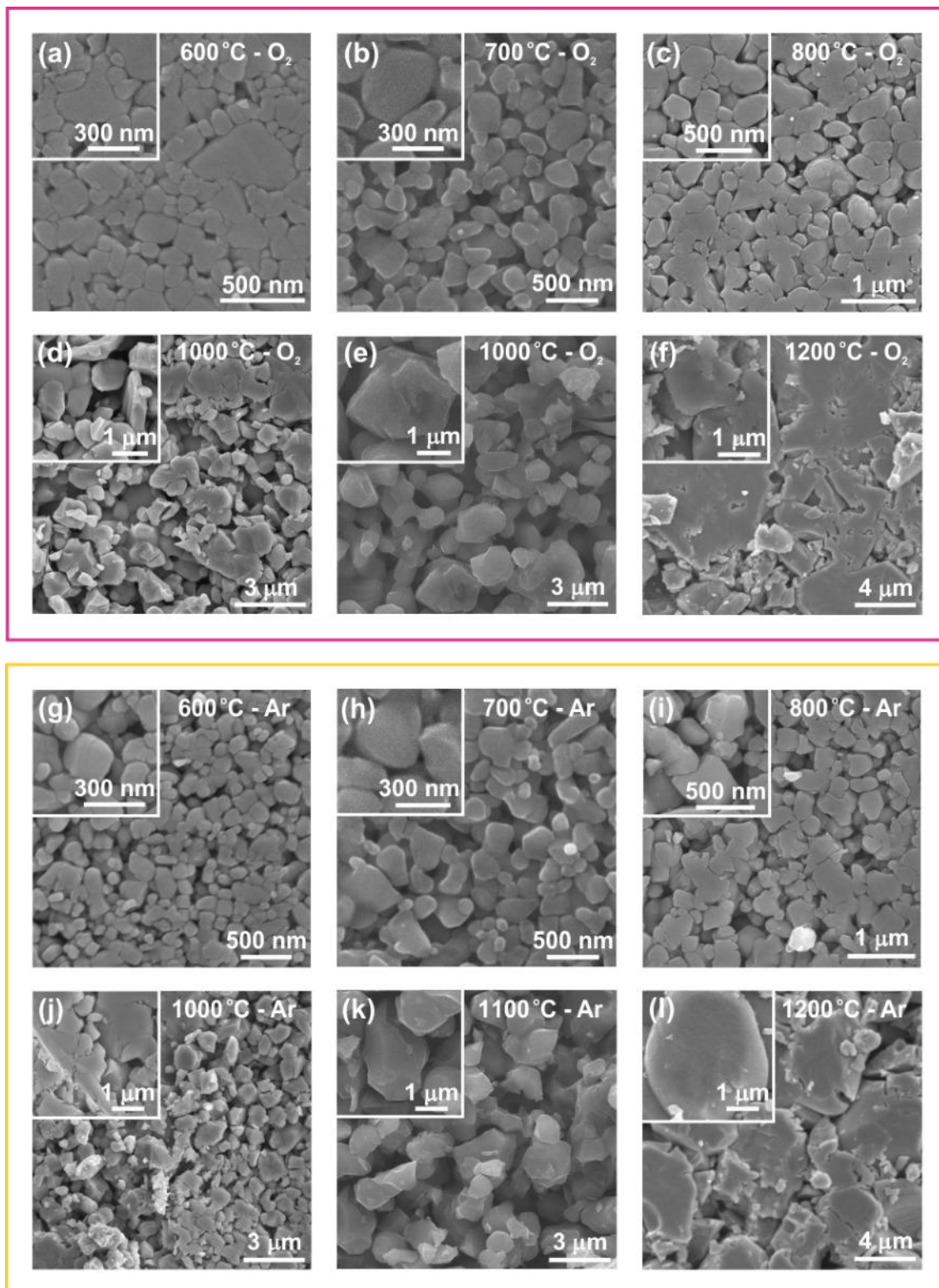


Figure S13 - Representative images by scanning electron microscopy of the surfaces of **CoO:ZnO** samples heat treated in O₂ at (a) 600 °C, (b) 700 °C, (c) 800 °C, (d) 1000 °C, (e) 1100 °C, (f) 1200 °C, and in Ar at (g) 600 °C, (h) 700 °C, (i) 800 °C, (j) 1000 °C, (k) 1100 °C, and (l) 1200 °C.

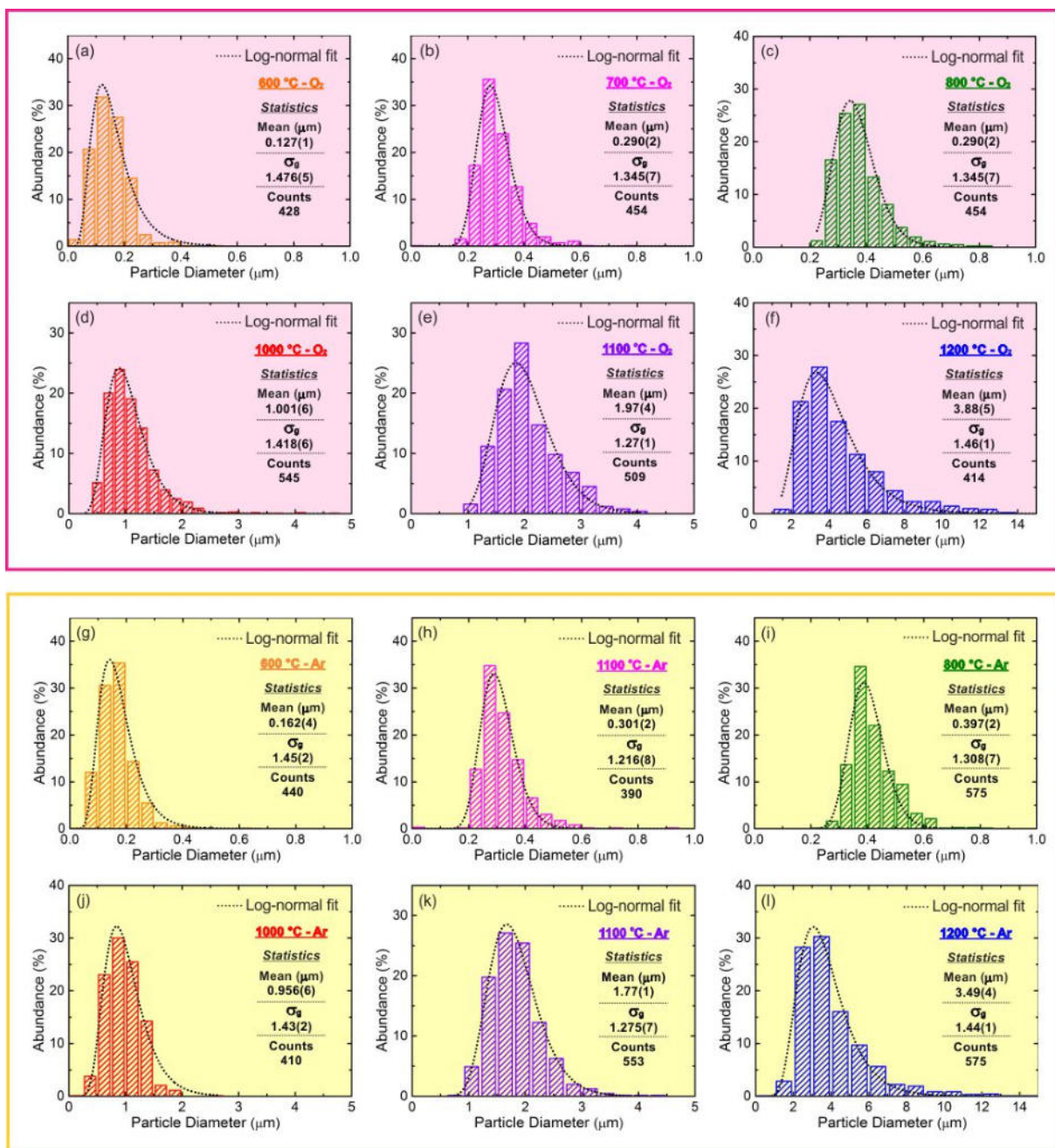


Figure S14 - Particle size distribution histograms of the **CoO:ZnO** samples heat treated in O₂ at (a) 600 °C, (b) 700 °C, (c) 800 °C, (d) 1000 °C, (e) 1100 °C, (f) 1200 °C, and in Ar at (g) 600 °C, (h) 700 °C, (i) 800 °C, (j) 1000 °C, (k) 1100 °C, and (l) 1200 °C. The distribution statistic obtained after log-normal fit is also presented in the panels.

Table S9 - Particle size distribution analyses of the **CoO:ZnO** samples. L is the mean value of the particle diameter and σ_g is the geometric standard deviation obtained by the log-normal fit of particle size distribution histograms for each sample. N is the total number of counted particles.

		Sample	L (μm)	σ_g	N
CoO:ZnO	Oxygen	Mixture	0.087(1)	1.51(1)	612
		600 °C	0.147(1)	1.56(3)	428
		700 °C	0.299(2)	1.217(5)	430
		800 °C	0.356(3)	1.222(9)	454
		1000 °C	1.001(6)	1.418(6)	545
		1100 °C	1.97(4)	1.27(1)	509
		1200 °C	3.88(5)	1.46(1)	414
		Argon	Mixture	0.088(1)	1.616(5)
	600 °C		0.162(4)	1.45(2)	440
	700 °C		0.301(2)	1.216(8)	390
	800 °C		0.397(2)	1.308(7)	402
	1000 °C		0.956(6)	1.43(2)	410
	1100 °C		1.77(1)	1.275(7)	553
	1200 °C		3.49(4)	1.44(1)	575

5

10

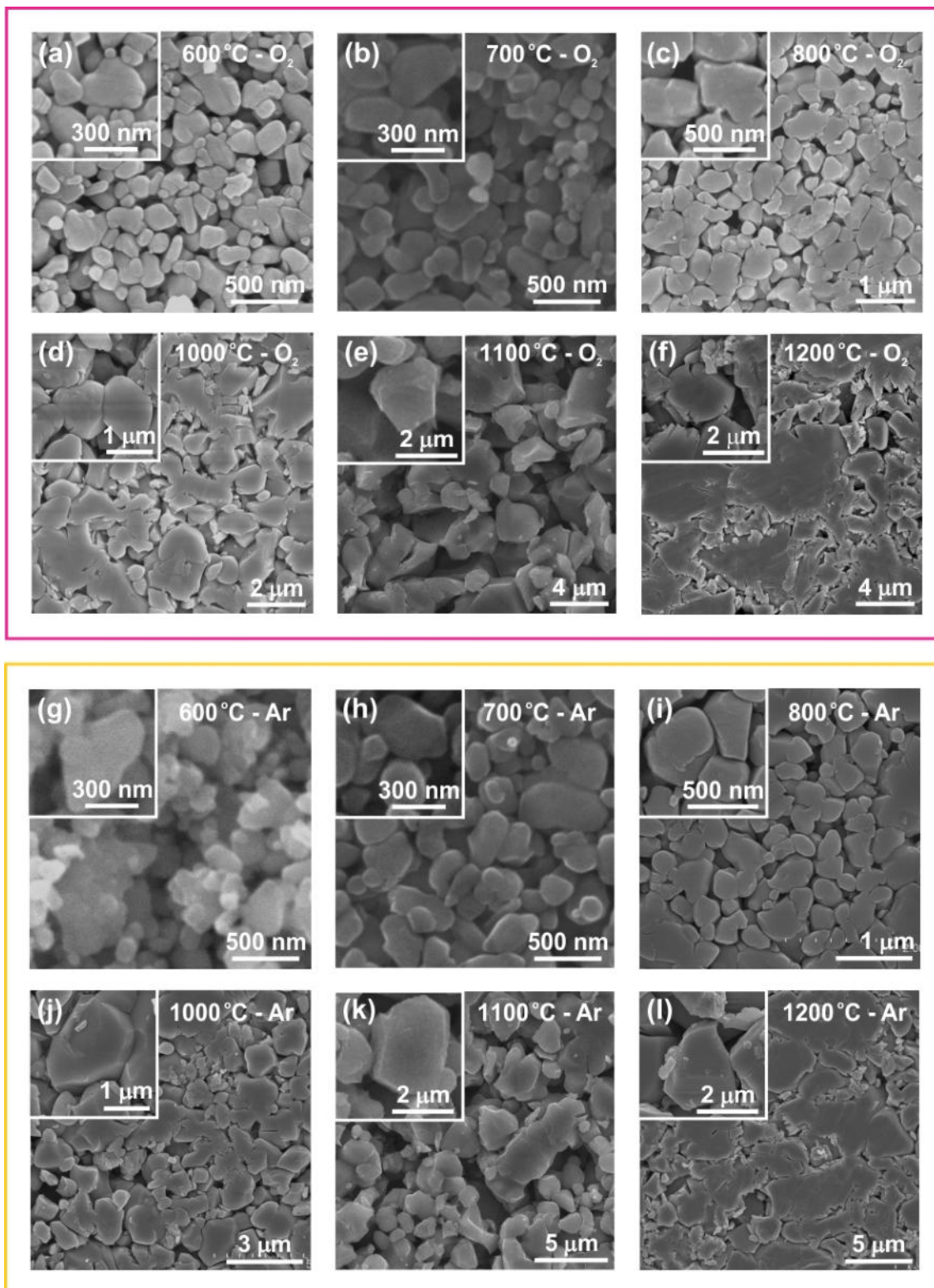


Figure S15 - Representative images by scanning electron microscopy of the surfaces of $m\text{Co:ZnO}$ samples heat treated in O_2 at (a) 600 °C, (b) 700 °C, (c) 800 °C, (d) 1000 °C, (e) 1100 °C, (f) 1200 °C, and in Ar at (g) 600 °C, (h) 700 °C, (i) 800 °C, (j) 1000 °C, (k) 1100 °C, and (l) 1200 °C.

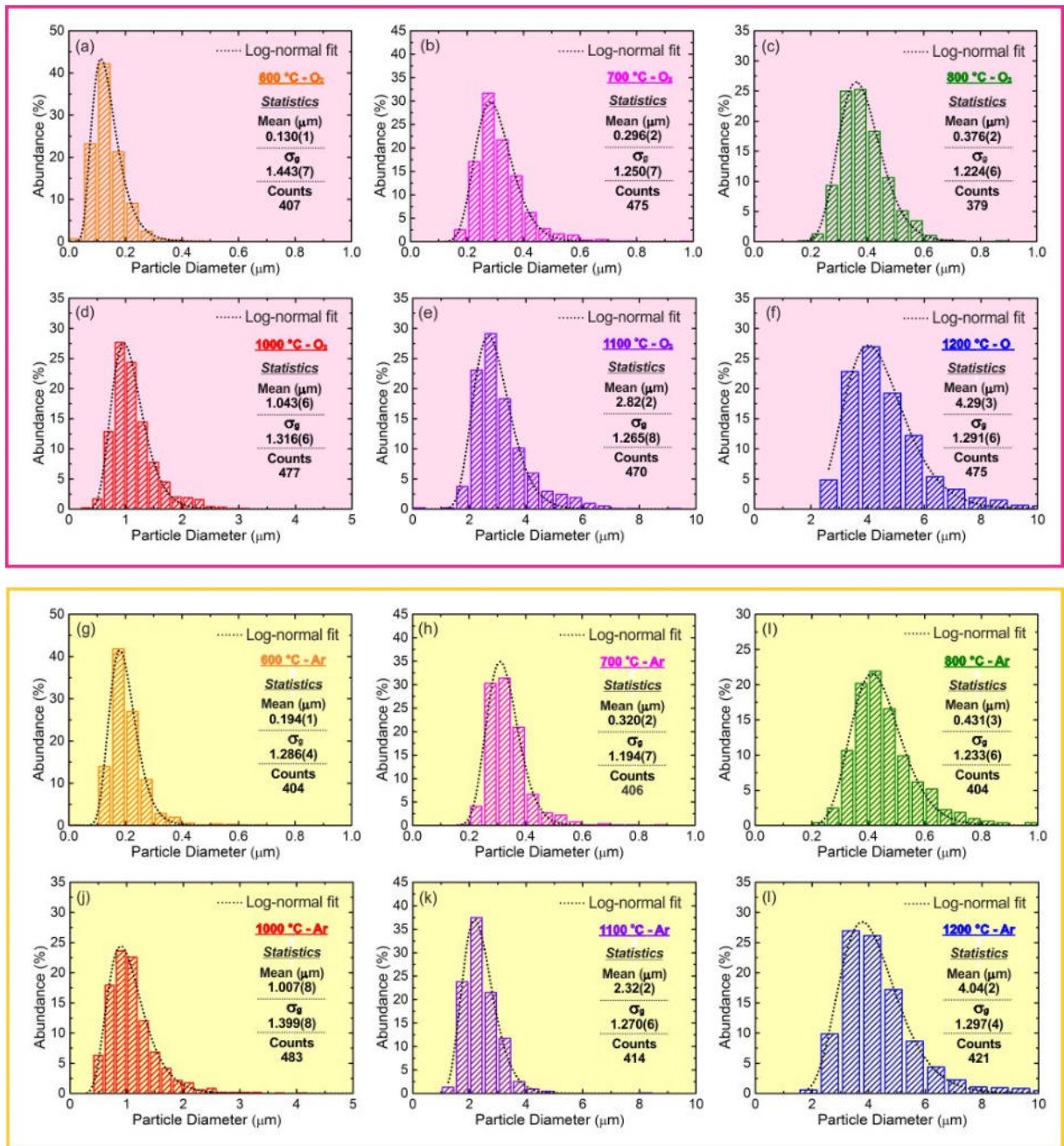


Figure S16 - Particle size distribution histograms of the *m*CoO:ZnO samples heat treated in O₂ at (a) 600 °C, (b) 700 °C, (c) 800 °C, (d) 1000 °C, (e) 1100 °C, (f) 1200 °C, and in Ar at (g) 600 °C, (h) 700 °C, (i) 800 °C, (j) 1000 °C, (k) 1100 °C, and (l) 1200 °C. The distribution statistic obtained after log-normal fit is also presented in the panels.

Table S10 - Particle size distribution analyses of the *mCoO:ZnO* samples. *L* is the mean value of the particle diameter and σ_g is the geometric standard deviation obtained by the log-normal fit of particle size distribution histograms for each sample. *N* is the total number of counted particles.

		Sample	<i>L</i> (μm)	σ_g	<i>N</i>
<i>mCo:ZnO</i>	<i>Oxygen</i>	Mixture	0.0917(6)	1.477(6)	531
		600 °C	0.130(1)	1.443(7)	407
		700 °C	0.296(2)	1.250(7)	475
		800 °C	0.376(2)	1.224(6)	379
		1000 °C	1.043(6)	1.316(6)	477
		1100 °C	2.82(2)	1.265(8)	470
		1200 °C	4.29(3)	1.291(6)	475
		<i>Argon</i>	Mixture	0.0917(6)	1.477(6)
	600 °C		0.194(1)	1.286(4)	404
	700 °C		0.320(2)	1.194(7)	406
	800 °C		0.431(3)	1.233(7)	404
	1000 °C		1.007(8)	1.399(8)	483
	1100 °C		2.32(2)	1.270(6)	414
	1200 °C		4.04(2)	1.297(4)	421

5

10

15

20

25

30

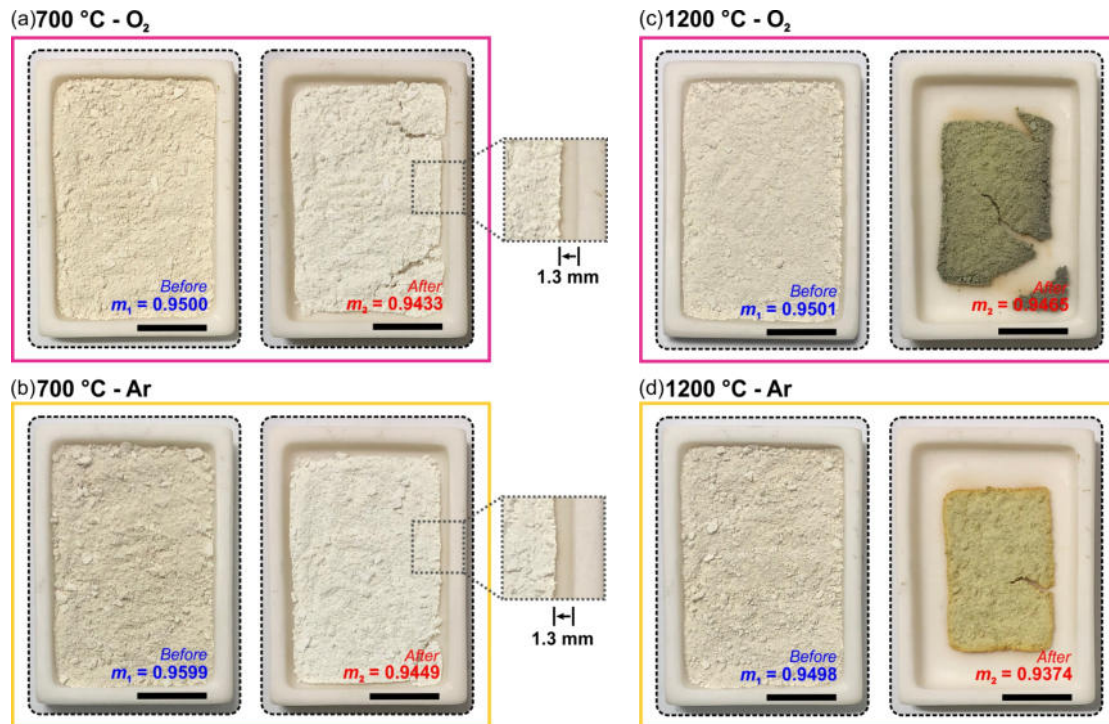


Figure S17. Representative micrographs for the pure ZnO samples before and after the heat treatments in O₂ and Ar at the temperatures of 700 °C and 1200 °C. A relatively small shrinkage is observed for the heat treatment at 700 °C, while an evident densification occurs at 1200 °C.

5

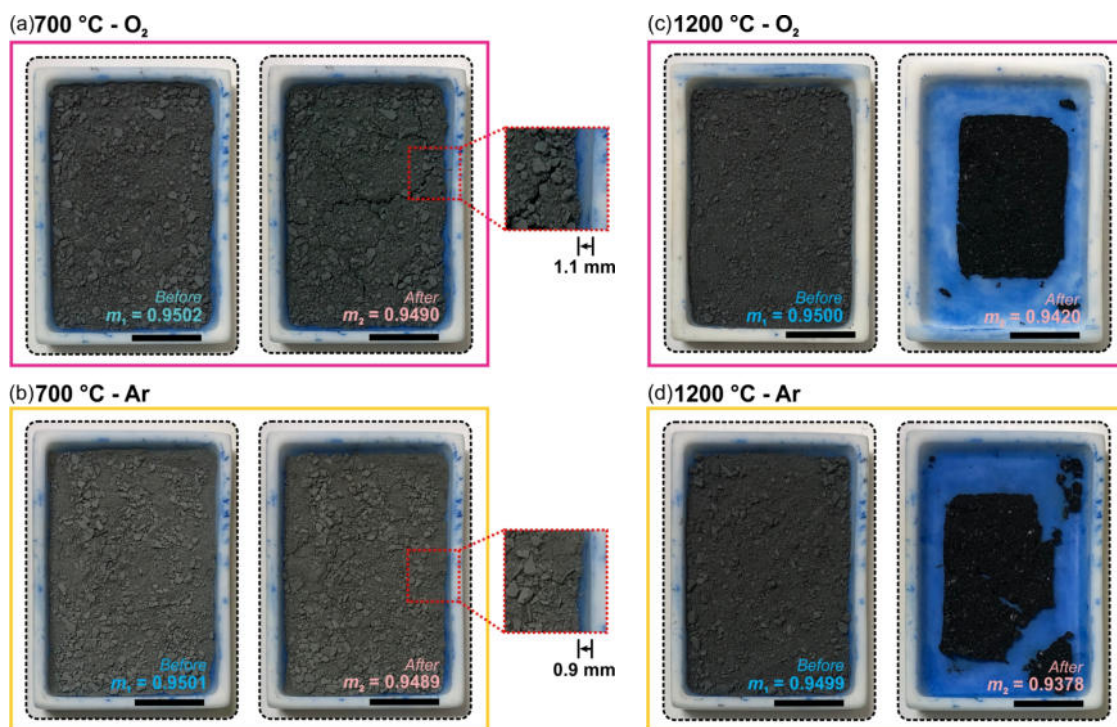


Figure S18. Representative micrographs for the *m*Co:ZnO samples before and after the heat treatments in O₂ and Ar at the temperatures of 700 °C and 1200 °C. A relatively small shrinkage is observed for the heat treatment at 700 °C, while an evident densification occurs at 1200 °C.

10

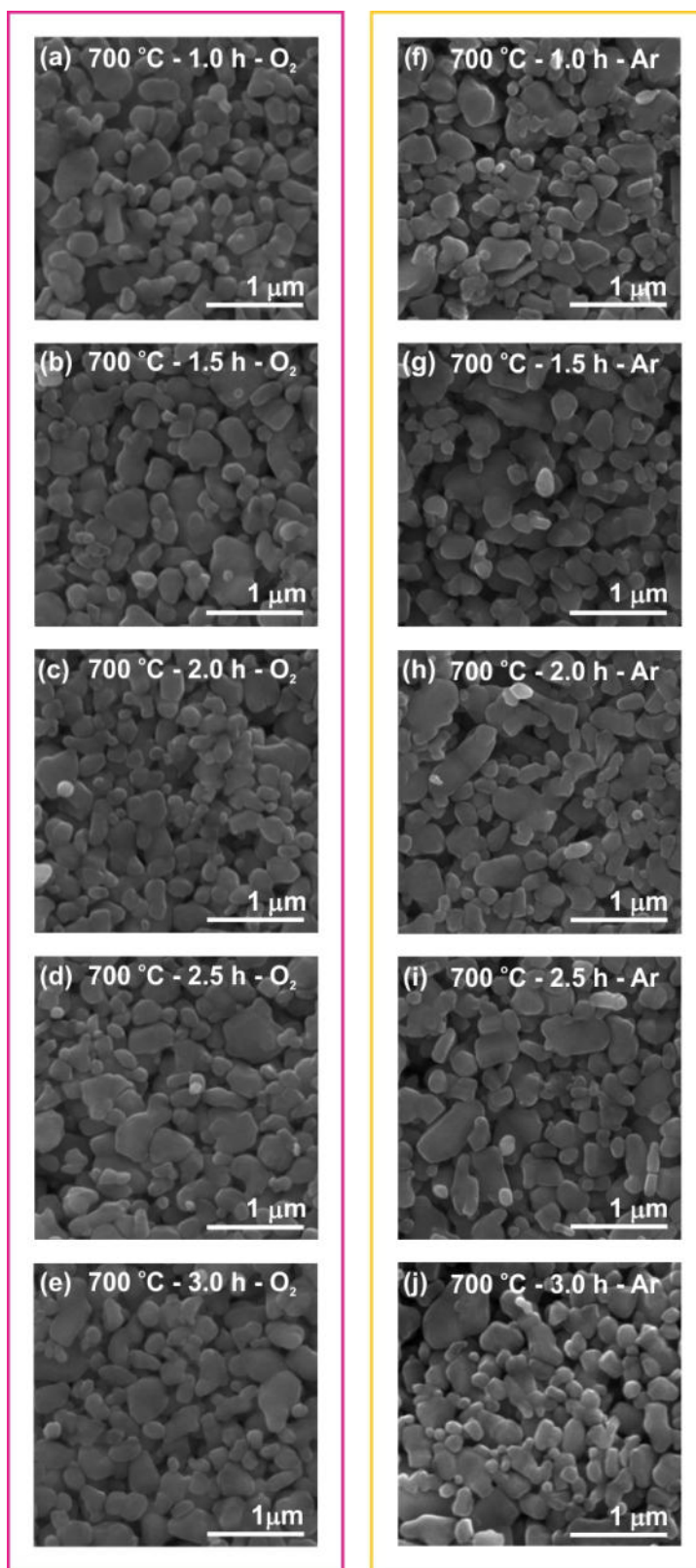


Figure S19 - Representative images by scanning electron microscopy of the surfaces of **ZnO** samples heat treated at **700 °C** in **O₂** for (a) 1.0 h , (b) 1.5 h, (c) 2.0 h, (d) 2.5 h, (e) 3.0 h, and in **Ar** for (f) 1.0 h, (g) 1.5 h, (h) 2.0 h, (i) 2.5 h, and (j) 3.0 h.

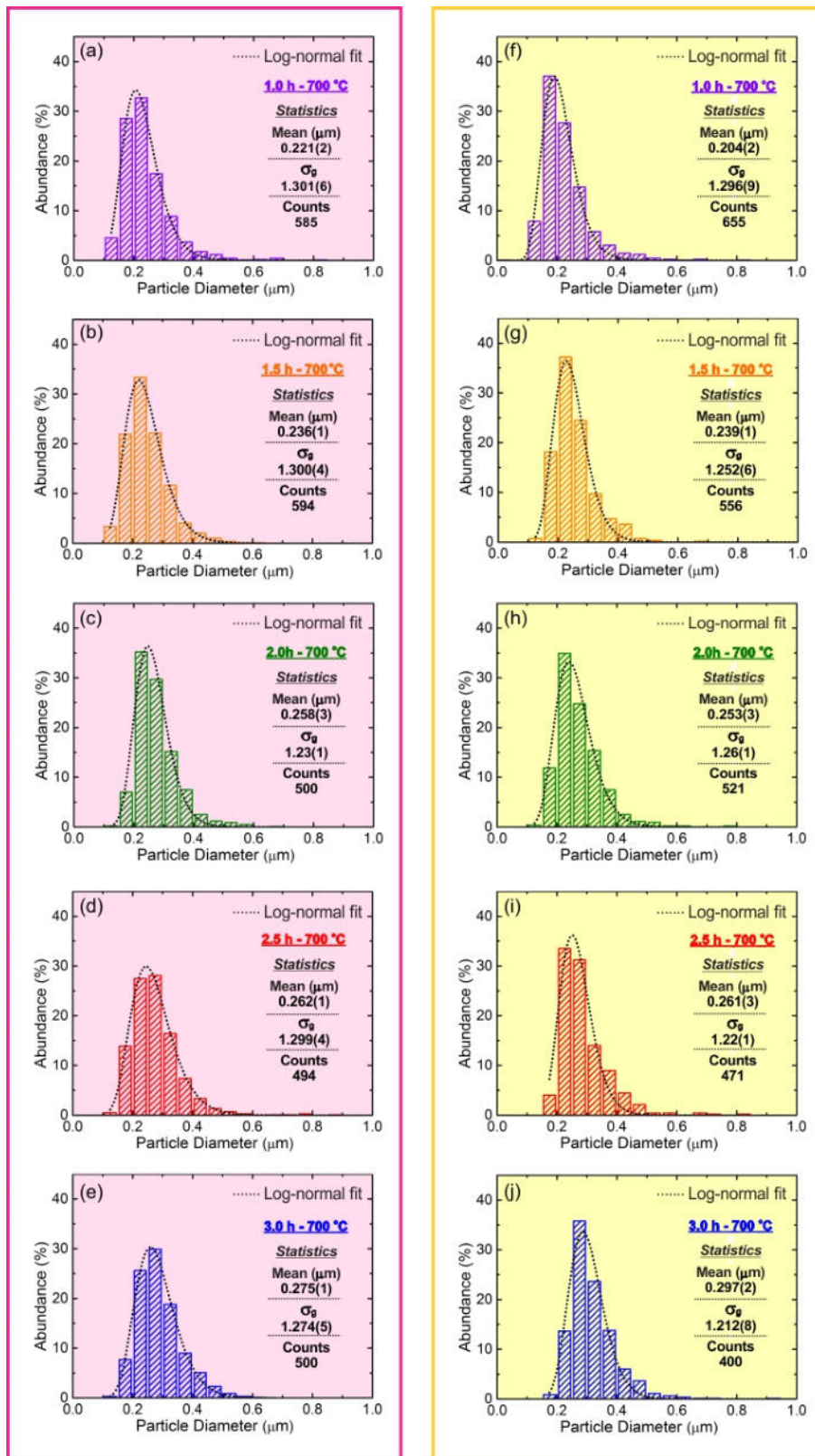


Figure S20 - Particle size distribution histograms of the **ZnO** samples heat treated at **700 °C** in **O₂** for (a) 1.0 h, (b) 1.5 h, (c) 2.0 h, (d) 2.5 h, (e) 3.0 h, and in **Ar** for (f) 1.0 h, (g) 1.5 h, (h) 2.0 h, (i) 2.5 h, and (j) 3.0 h. The lines in the panels correspond to the log-normal fit.

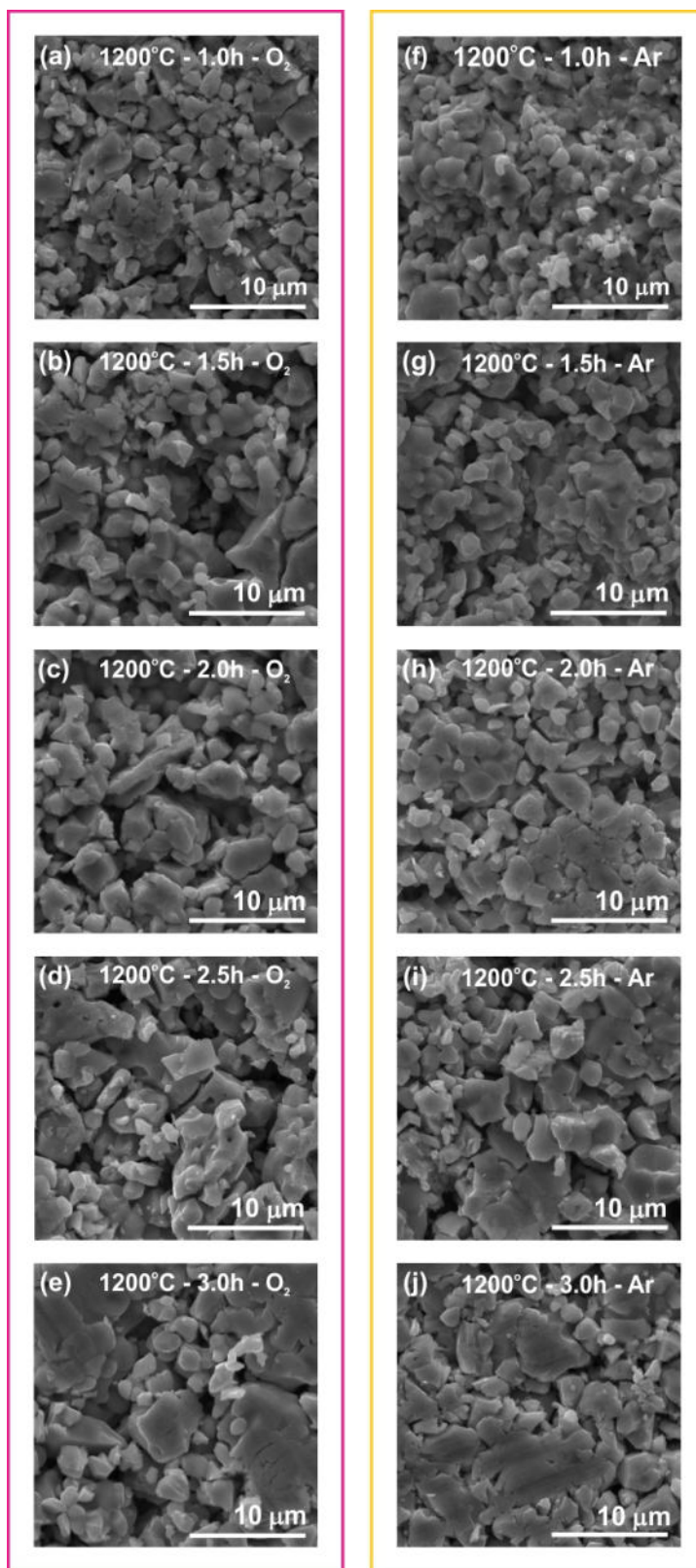


Figure S21 - Representative images by scanning electron microscopy of the surfaces of **ZnO** samples heat treated at **1200 °C** in O₂ for (a) 1.0 h , (b) 1.5 h, (c) 2.0 h, (d) 2.5 h, (e) 3.0 h, and in Ar for (f) 1.0 h, (g) 1.5 h, (h) 2.0 h, (i) 2.5 h, and (j) 3.0 h.

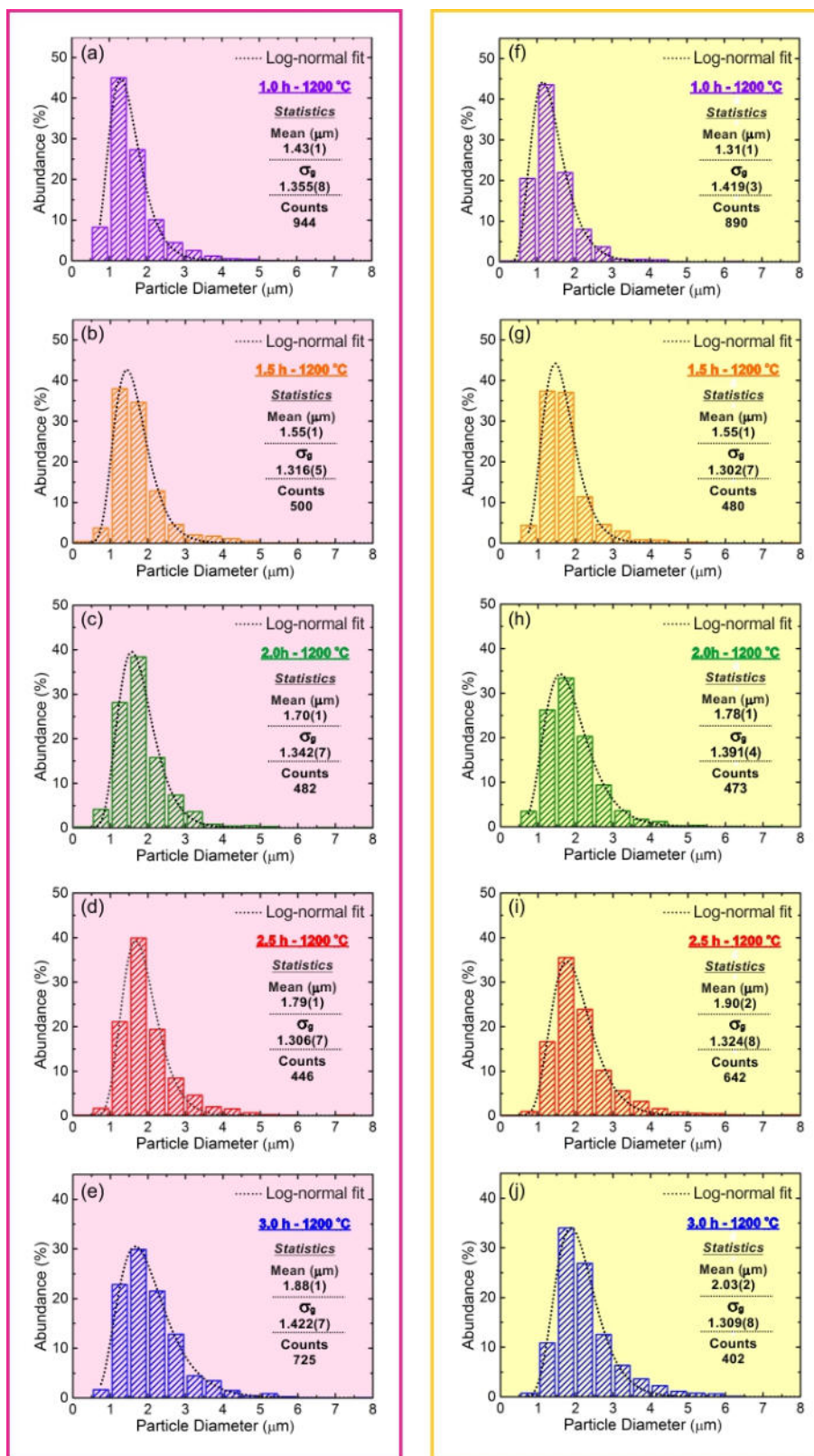


Figure S22 - Particle size distribution histograms of the ZnO samples heat treated at 1200 °C in O₂ for (a) 1.0 h, (b) 1.5 h, (c) 2.0 h, (d) 2.5 h, (e) 3.0 h, and in Ar for (f) 1.0 h, (g) 1.5 h, (h) 2.0 h, (i) 2.5 h, and (j) 3.0 h. The line in the panels correspond to the log-normal fit.

Table S11 - Particle size distribution analyses of the **ZnO** samples heat treated at **700 °C** at different times. L is the mean value of the particle diameter and σ_g is the geometric standard deviation obtained by the log-normal fit of particle size distribution histograms for each sample. N is the total number of counted particles.

		Sample	L (μm)	σ_g	N
ZnO – 700 °C	Oxygen	1.0h	0.221(2)	1.301(6)	585
		1.5h	0.236(1)	1.300(4)	594
		2.0h	0.258(3)	1.23(1)	500
		2.5h	0.262(1)	1.299(4)	494
		3.0h	0.275(1)	1.274(5)	500
	Argon	1.0h	0.204(2)	1.296(9)	655
		1.5h	0.239(1)	1.252(6)	556
		2.0h	0.253(3)	1.26(1)	521
		2.5h	0.261(3)	1.22(1)	471
		3.0h	0.297(2)	1.212(8)	400

5

Table S12 - Particle size distribution analyses of the **ZnO** samples heat treated at **1200 °C** at different times. L is the mean value of the particle diameter and σ_g is the geometric standard deviation obtained by the log-normal fit of particle size distribution histograms for each sample. N is the total number of counted particles.

		Sample	L (μm)	σ_g	N
ZnO – 1200 °C	Oxygen	1.0h	1.43(1)	1.355(8)	944
		1.5h	1.55(1)	1.316(5)	500
		2.0h	1.70(1)	1.342(7)	482
		2.5h	1.79(1)	1.306(7)	446
		3.0h	1.88(1)	1.422(7)	725
	Argon	1.0h	1.31(1)	1.419(3)	890
		1.5h	1.55(1)	1.302(7)	480
		2.0h	1.78(1)	1.391(4)	473
		2.5h	1.90(2)	1.324(8)	642
		3.0h	2.03(2)	1.309(8)	402

10

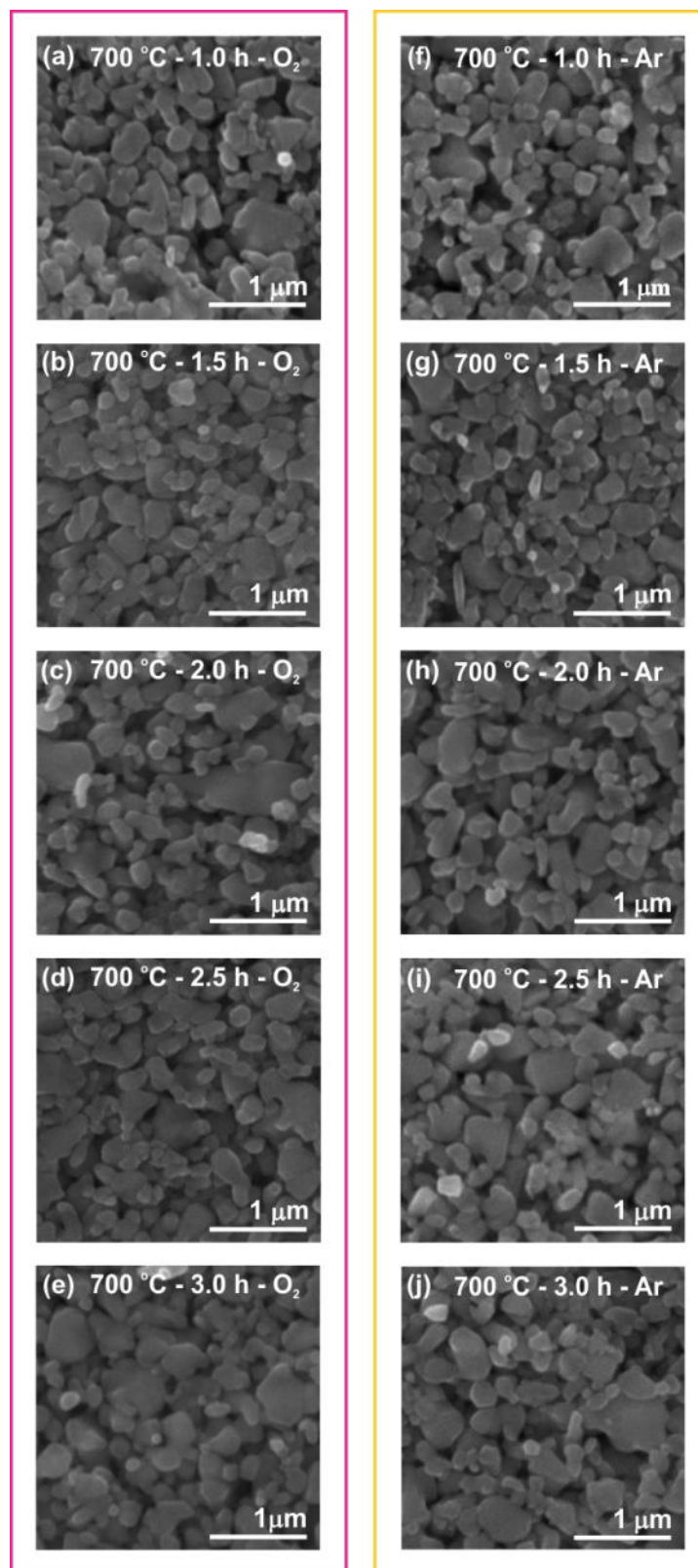


Figure S23 - Representative images by scanning electron microscopy of the surfaces of $\text{Co}_3\text{O}_4:\text{ZnO}$ samples heat treated at $700\text{ }^\circ\text{C}$ in O_2 for (a) 1.0 h , (b) 1.5 h, (c) 2.0 h, (d) 2.5 h, (e) 3.0 h, and in Ar for (f) 1.0 h, (g) 1.5 h, (h) 2.0 h, (i) 2.5 h, and (j) 3.0 h.

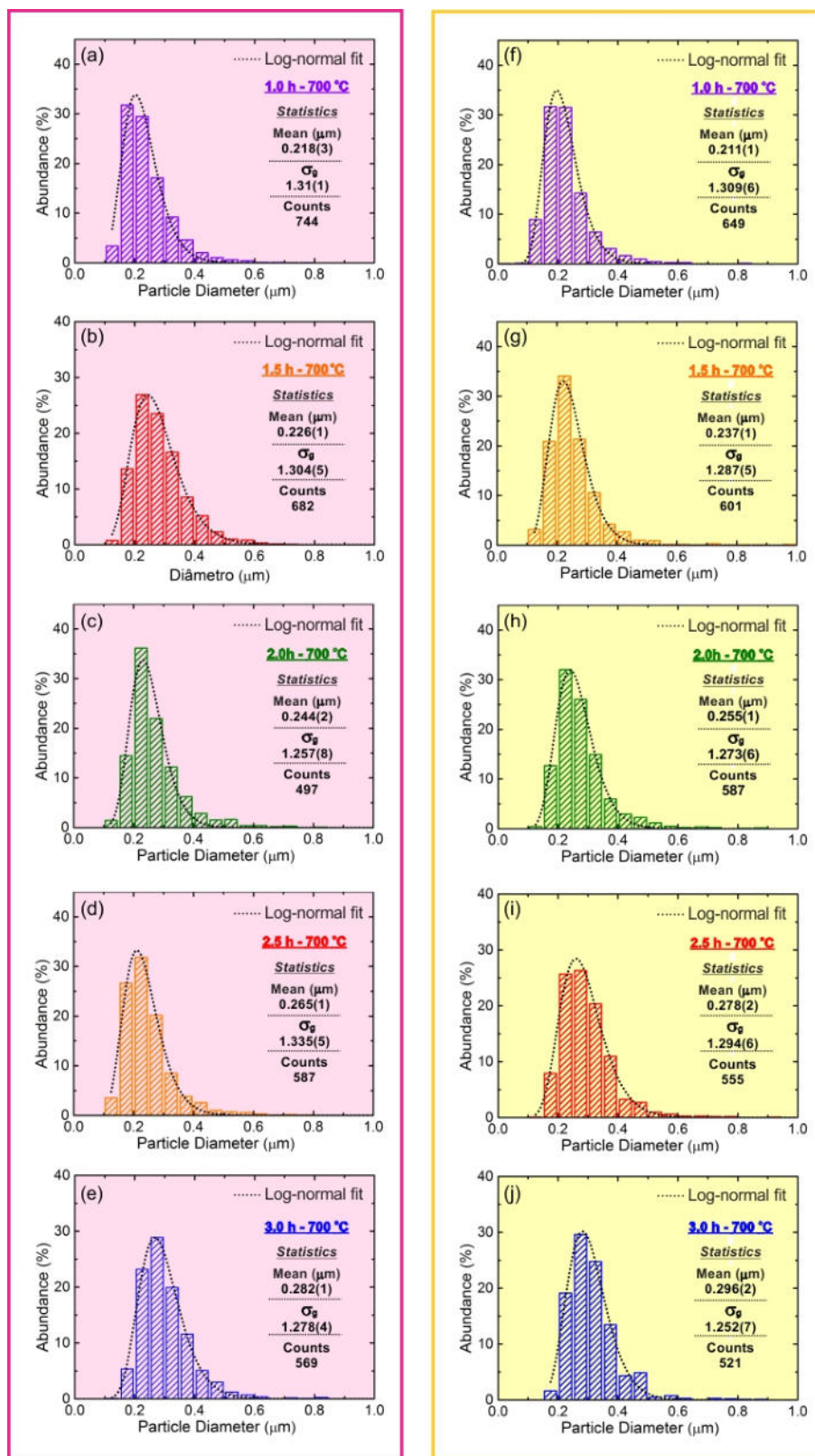


Figure S24 - Particle size distribution histograms of the $\text{Co}_3\text{O}_4:\text{ZnO}$ samples heat treated at 700 °C in O_2 for (a) 1.0 h, (b) 1.5 h, (c) 2.0 h, (d) 2.5 h, (e) 3.0 h, and in Ar for (f) 1.0 h, (g) 1.5 h, (h) 2.0 h, (i) 2.5 h, and (j) 3.0 h. The line in the panels correspond to the log-normal fit.

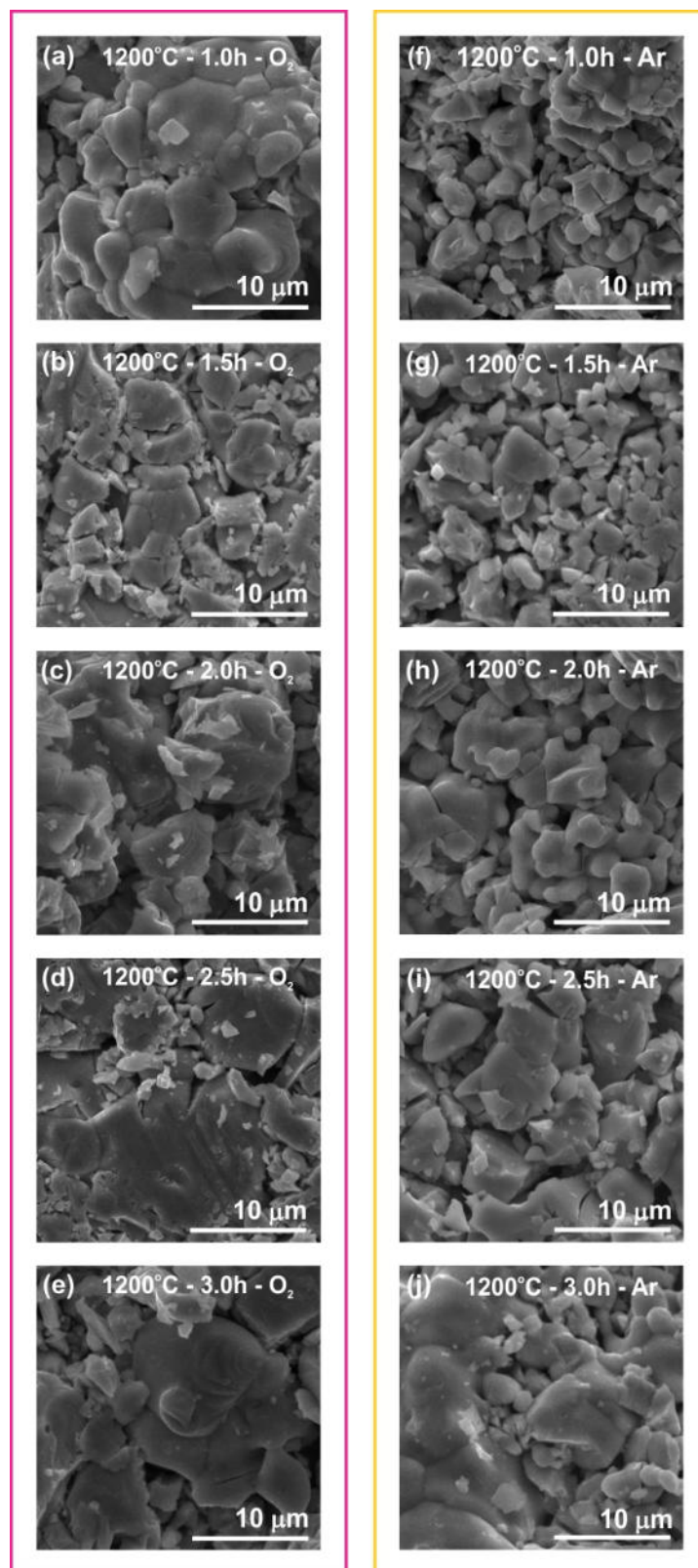


Figure S25 - Representative images by scanning electron microscopy of the surfaces of $Co_3O_4:ZnO$ samples heat treated at 1200 °C in O_2 for (a) 1.0 h, (b) 1.5 h, (c) 2.0 h, (d) 2.5 h, (e) 3.0 h, and in Ar for (f) 1.0 h, (g) 1.5 h, (h) 2.0 h, (i) 2.5 h, and (j) 3.0 h.

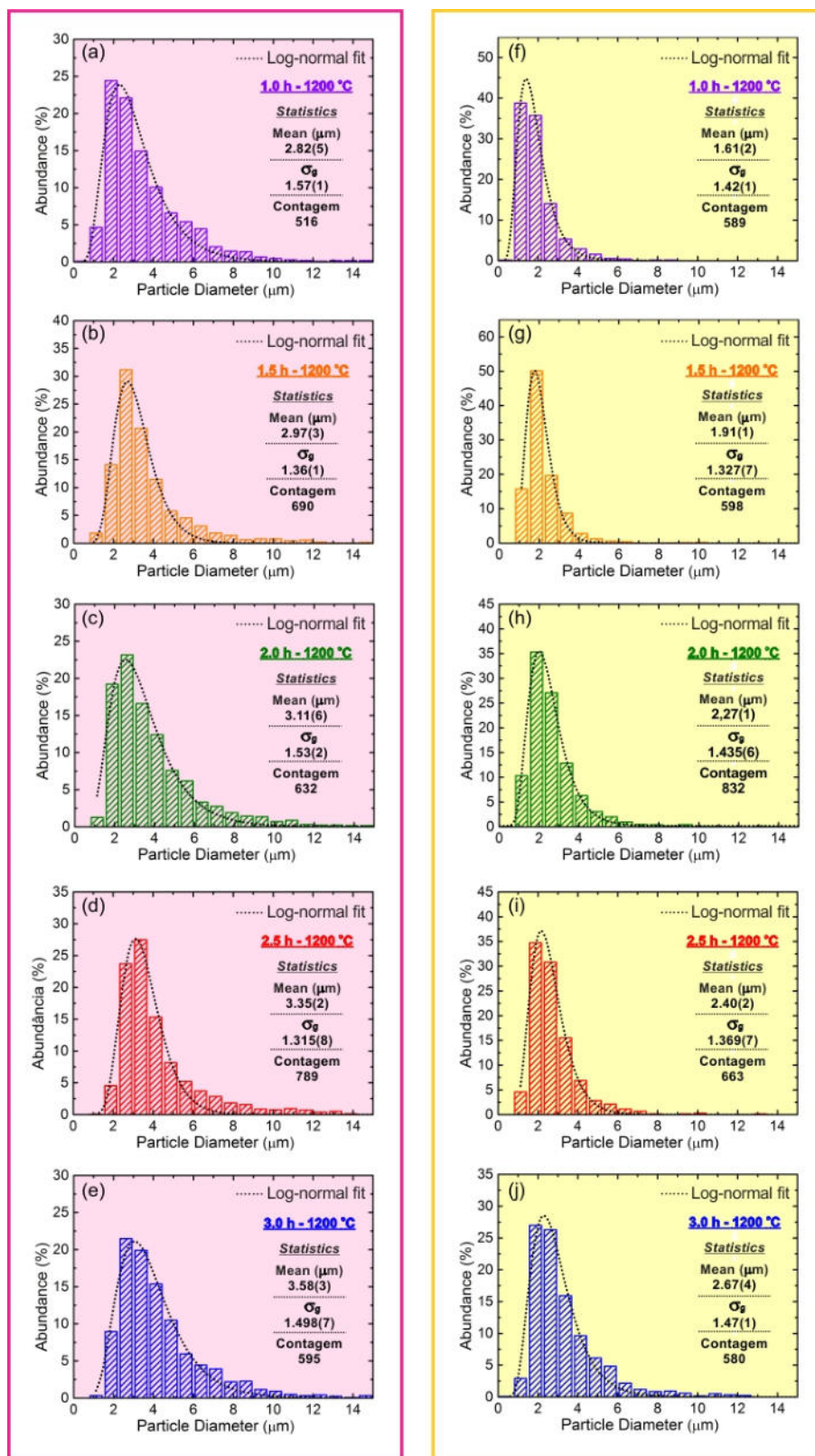


Figure S26 - Particle size distribution histograms of the $\text{Co}_3\text{O}_4:\text{ZnO}$ samples heat treated at $1200\text{ }^\circ\text{C}$ in O_2 for (a) 1.0 h, (b) 1.5 h, (c) 2.0 h, (d) 2.5 h, (e) 3.0 h, and in Ar for (f) 1.0 h, (g) 1.5 h, (h) 2.0 h, (i) 2.5 h, and (j) 3.0 h. The line in the panels correspond to the log-normal fit.

Table S13 - Particle size distribution analyses of the $\text{Co}_3\text{O}_4:\text{ZnO}$ samples heat treated at $700\text{ }^\circ\text{C}$ at different times. L is the mean value of the particle diameter and σ_g is the geometric standard deviation obtained by the log-normal fit of particle size distribution histograms for each sample. N is the total number of counted particles.

		Sample	L (μm)	σ_g	N
$\text{Co}_3\text{O}_4:\text{ZnO} - 700\text{ }^\circ\text{C}$	Oxygen	1.0h	0.218(3)	1.31(1)	744
		1.5h	0.226(1)	1.304(5)	682
		2.0h	0.244(2)	1.257(8)	497
		2.5h	0.265(1)	1.335(5)	587
		3.0h	0.282(1)	1.278(4)	569
	Argon	1.0h	0.211(1)	1.309(6)	649
		1.5h	0.237(1)	1.287(5)	601
		2.0h	0.255(1)	1.273(6)	587
		2.5h	0.278(2)	1.294(6)	555
		3.0h	0.296(2)	1.252(7)	521

5

Table S14 - Particle size distribution analyses of the $\text{Co}_3\text{O}_4:\text{ZnO}$ samples heat treated at $1200\text{ }^\circ\text{C}$ at different times. L is the mean value of the particle diameter and σ_g is the geometric standard deviation obtained by the log-normal fit of particle size distribution histograms for each sample. N is the total number of counted particles.

		Sample	L (μm)	σ_g	N
$\text{Co}_3\text{O}_4:\text{ZnO} - 1200\text{ }^\circ\text{C}$	Oxygen	1.0h	2.82(5)	1.57(1)	516
		1.5h	2.97(3)	1.36(1)	690
		2.0h	3.11(6)	1.53(2)	632
		2.5h	3.35(2)	1.315(8)	789
		3.0h	3.58(3)	1.498(7)	595
	Argon	1.0h	1.61(2)	1.42(1)	589
		1.5h	1.91(1)	1.327(7)	598
		2.0h	2.27(1)	1.435(6)	832
		2.5h	2.40(2)	1.369(7)	663
		3.0h	2.67(4)	1.47(1)	580

10

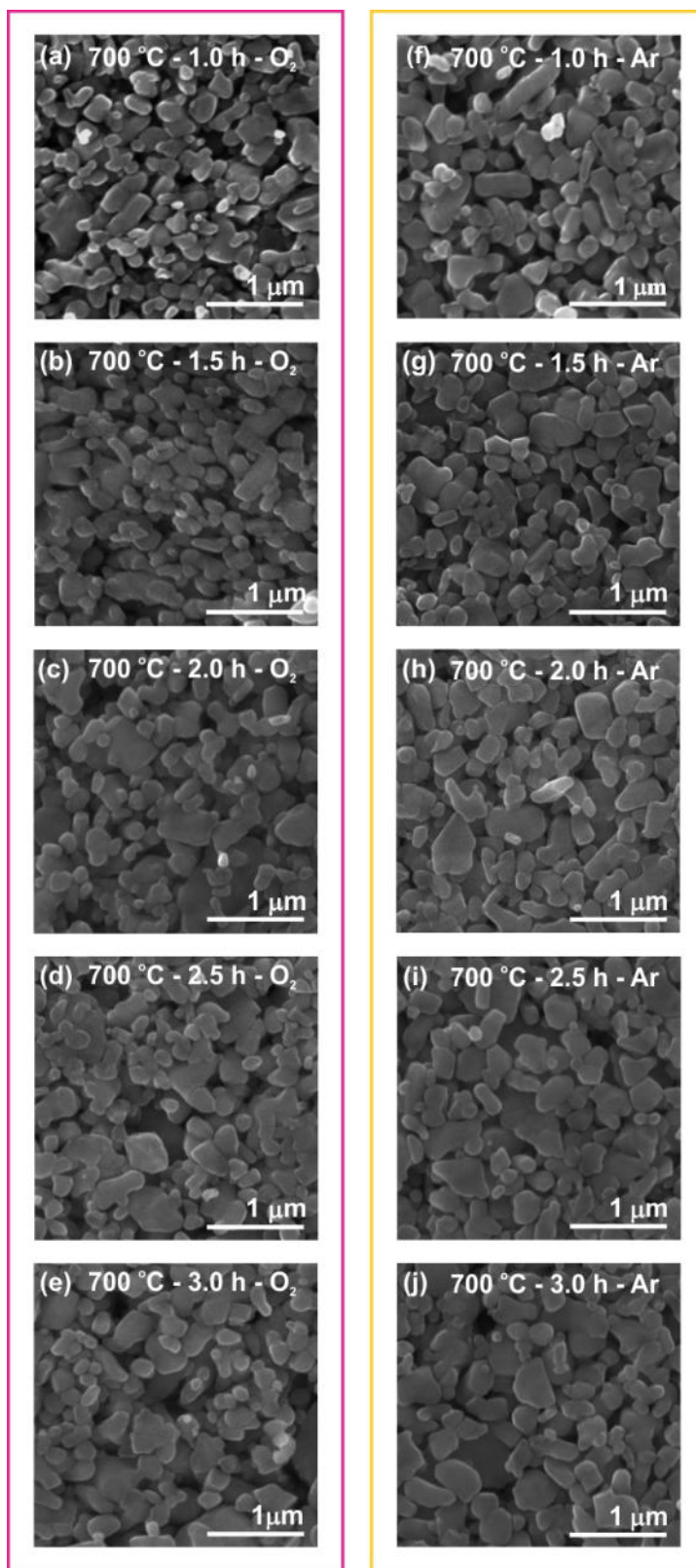


Figure S27 - Representative images by scanning electron microscopy of the surfaces of **CoO:ZnO** samples heat treated at **700 °C** in O_2 for (a) 1.0 h , (b) 1.5 h, (c) 2.0 h, (d) 2.5 h, (e) 3.0 h, and in Ar for (f) 1.0 h, (g) 1.5 h, (h) 2.0 h, (i) 2.5 h, and (j) 3.0 h.

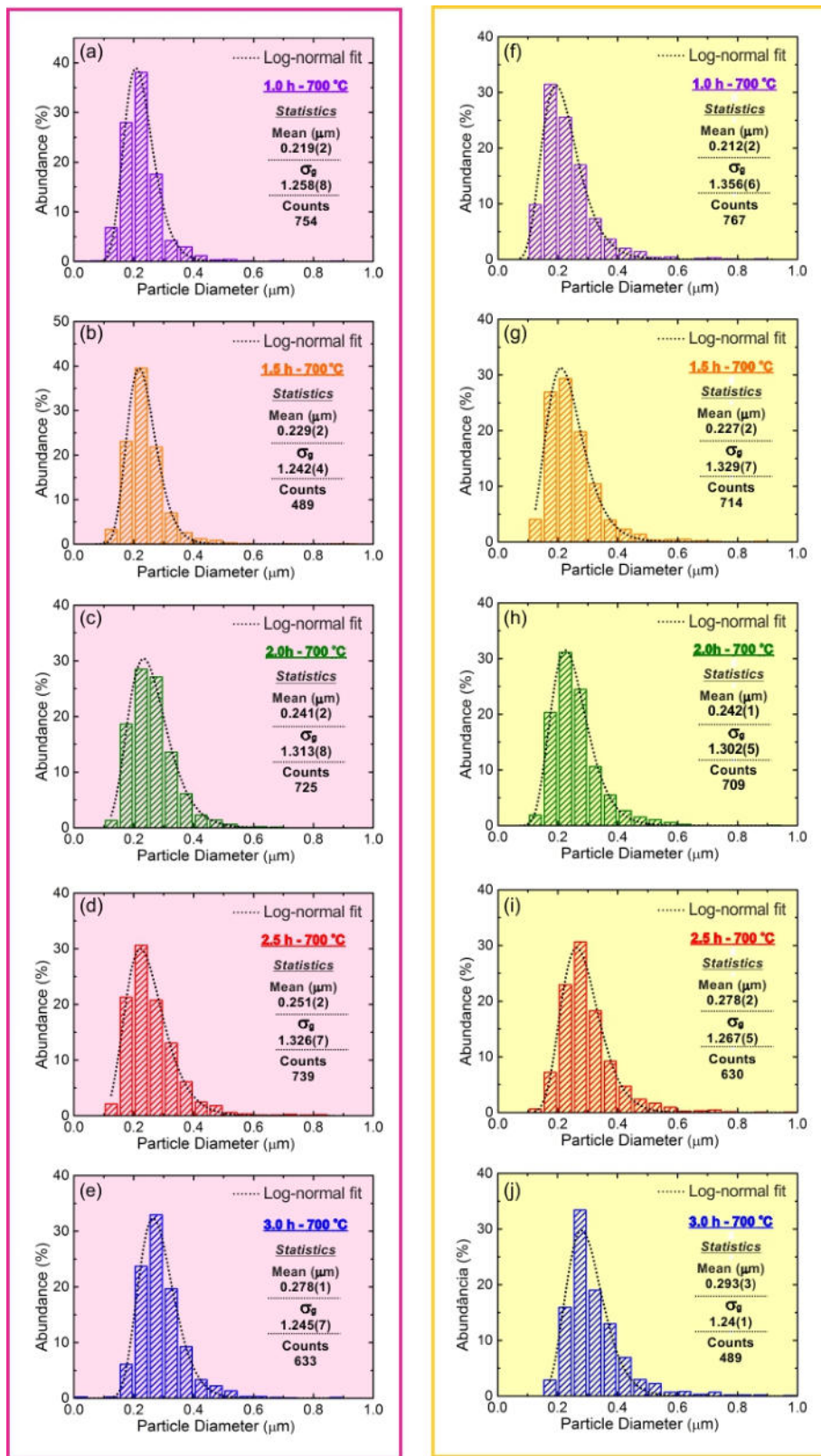


Figure S28 - Particle size distribution histograms of the **CoO:ZnO** samples heat treated at **700 °C** in **O₂** for (a) 1.0 h, (b) 1.5 h, (c) 2.0 h, (d) 2.5 h, (e) 3.0 h, and in **Ar** for (f) 1.0 h, (g) 1.5 h, (h) 2.0 h, (i) 2.5 h, and (j) 3.0 h. The line in the panels correspond to the log-normal fit.

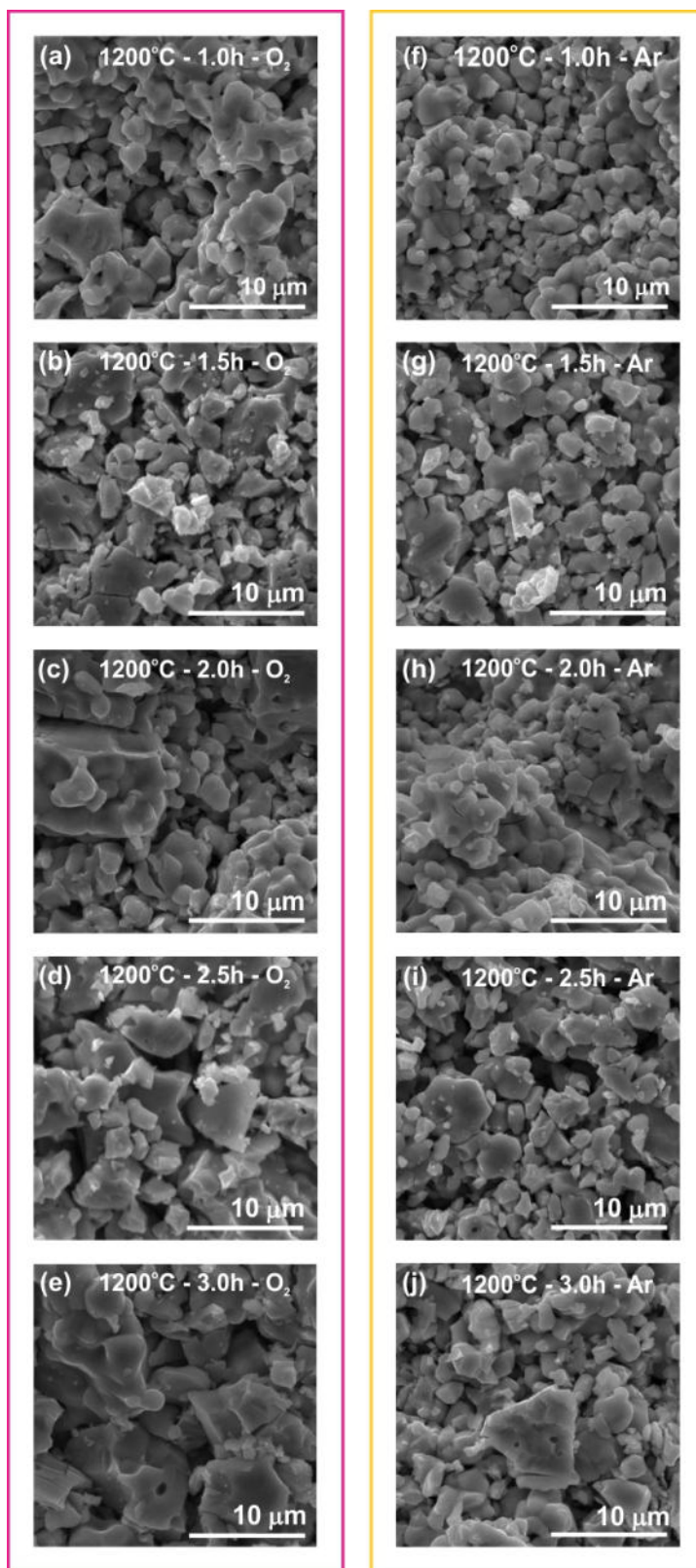


Figure S29 - Representative images by scanning electron microscopy of the surfaces of $\text{CoO}:\text{ZnO}$ samples heat treated at 1200°C in O_2 for (a) 1.0 h, (b) 1.5 h, (c) 2.0 h, (d) 2.5 h, (e) 3.0 h, and in Ar for (f) 1.0 h, (g) 1.5 h, (h) 2.0 h, (i) 2.5 h, and (j) 3.0 h.

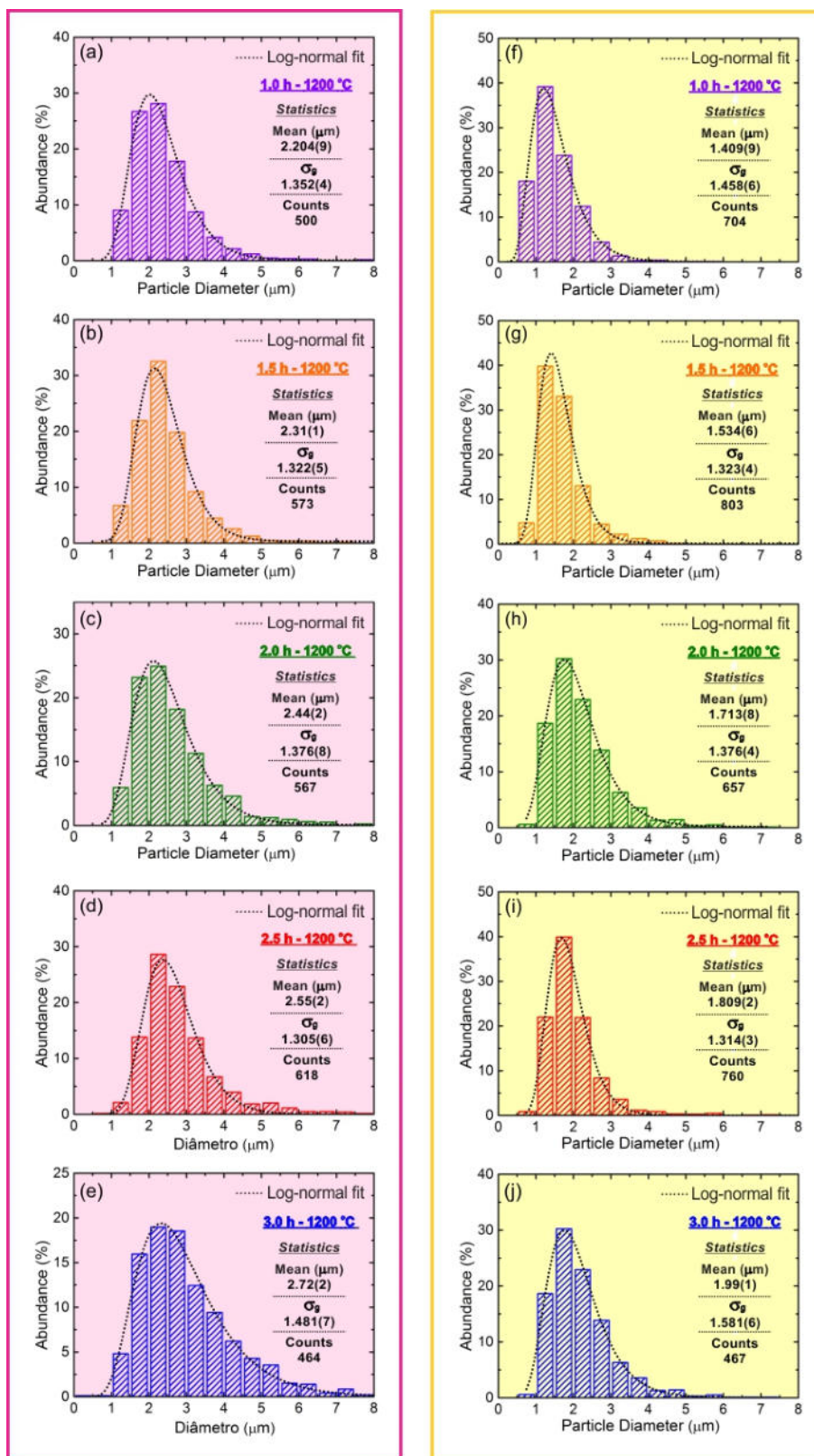


Figure S30 - Particle size distribution histograms of the CoO:ZnO samples heat treated at 1200 °C in O₂ for (a) 1.0 h , (b) 1.5 h, (c) 2.0 h, (d) 2.5 h, (e) 3.0 h, and in Ar for (f) 1.0 h, (g) 1.5 h, (h) 2.0 h, (i) 2.5 h, and (j) 3.0 h. The line in the panels correspond to the log-normal fit.

Table S15 - Particle size distribution analyses of the **CoO:ZnO** samples heat treated at **700 °C** at different times. L is the mean value of the particle diameter and σ_g is the geometric standard deviation obtained by the log-normal fit of particle size distribution histograms for each sample. N is the total number of counted particles.

5

		Sample	L (μm)	σ_g	N
CoO:ZnO - 700 °C	Oxygen	1.0h	0.219(2)	1.258(8)	754
		1.5h	0.229(1)	1.242(4)	707
		2.0h	0.241(2)	1.313(8)	725
		2.5h	0.251(2)	1.326(7)	739
		3.0h	0.278(1)	1.245(5)	633
	Argon	1.0h	0.212(2)	1.356(6)	767
		1.5h	0.227(2)	1.329(7)	714
		2.0h	0.242(1)	1.302(5)	709
		2.5h	0.278(2)	1.267(5)	630
		3.0h	0.293(3)	1.24(1)	489

Table S16 - Particle size distribution analyses of the **CoO:ZnO** samples heat treated at **1200 °C** at different times. L is the mean value of the particle diameter and σ_g is the geometric standard deviation obtained by the log-normal fit of particle size distribution histograms for each sample. N is the total number of counted particles.

10

		Sample	L (μm)	σ_g	N
CoO:ZnO - 1200 °C	Oxygen	1.0h	2.204(9)	1.352(4)	500
		1.5h	2.31(1)	1.322(5)	573
		2.0h	2.44(2)	1.376(8)	580
		2.5h	2.55(2)	1.305(6)	618
		3.0h	2.72(2)	1.481(7)	467
	Argon	1.0h	1.409(9)	1.458(6)	704
		1.5h	1.534(6)	1.323(4)	803
		2.0h	1.713(8)	1.376(4)	657
		2.5h	1.809(2)	1.314(3)	760
		3.0h	1.99(1)	1.581(6)	491

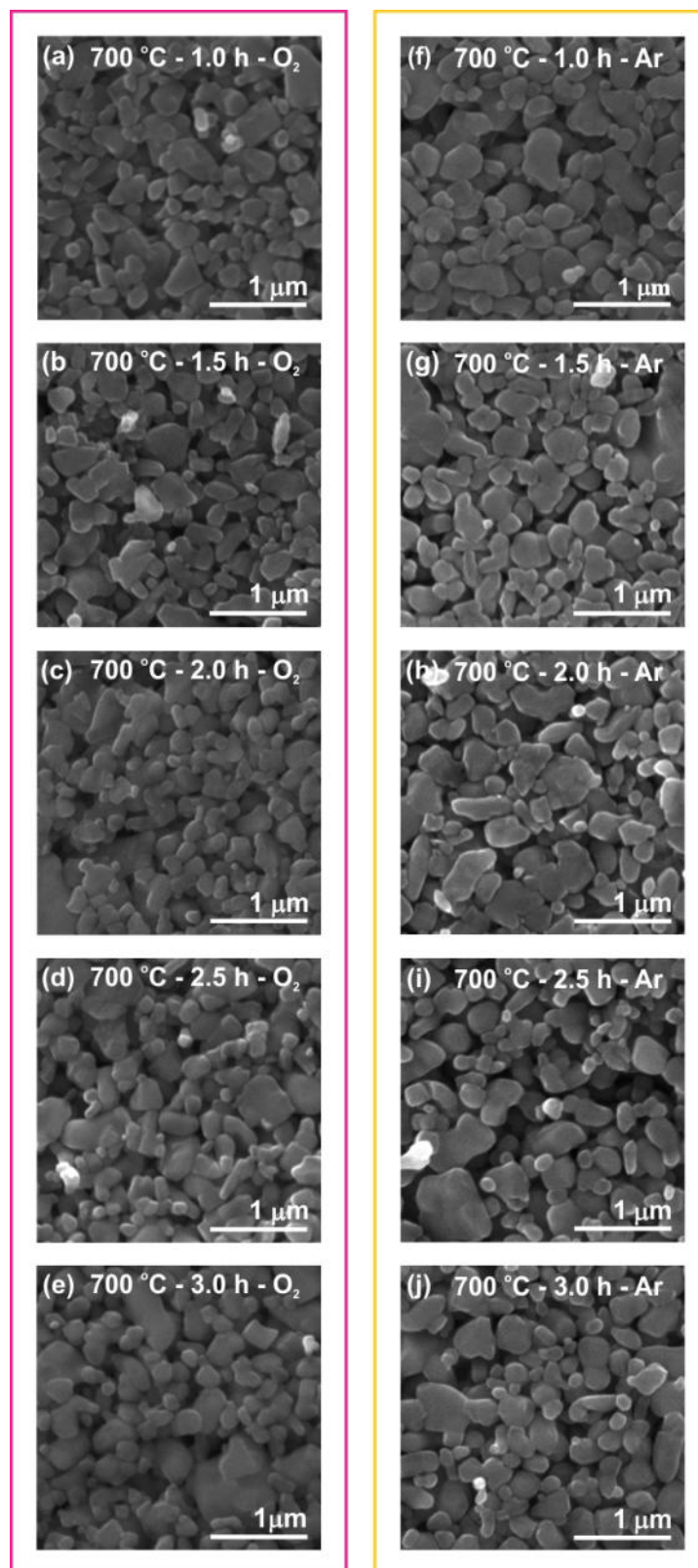


Figure S31 - Representative images by scanning electron microscopy of the surfaces of *mCo:ZnO* samples heat treated at 700 °C in O₂ for (a) 1.0 h , (b) 1.5 h, (c) 2.0 h, (d) 2.5 h, (e) 3.0 h, and in Ar for (f) 1.0 h, (g) 1.5 h, (h) 2.0 h, (i) 2.5 h, and (j) 3.0 h.

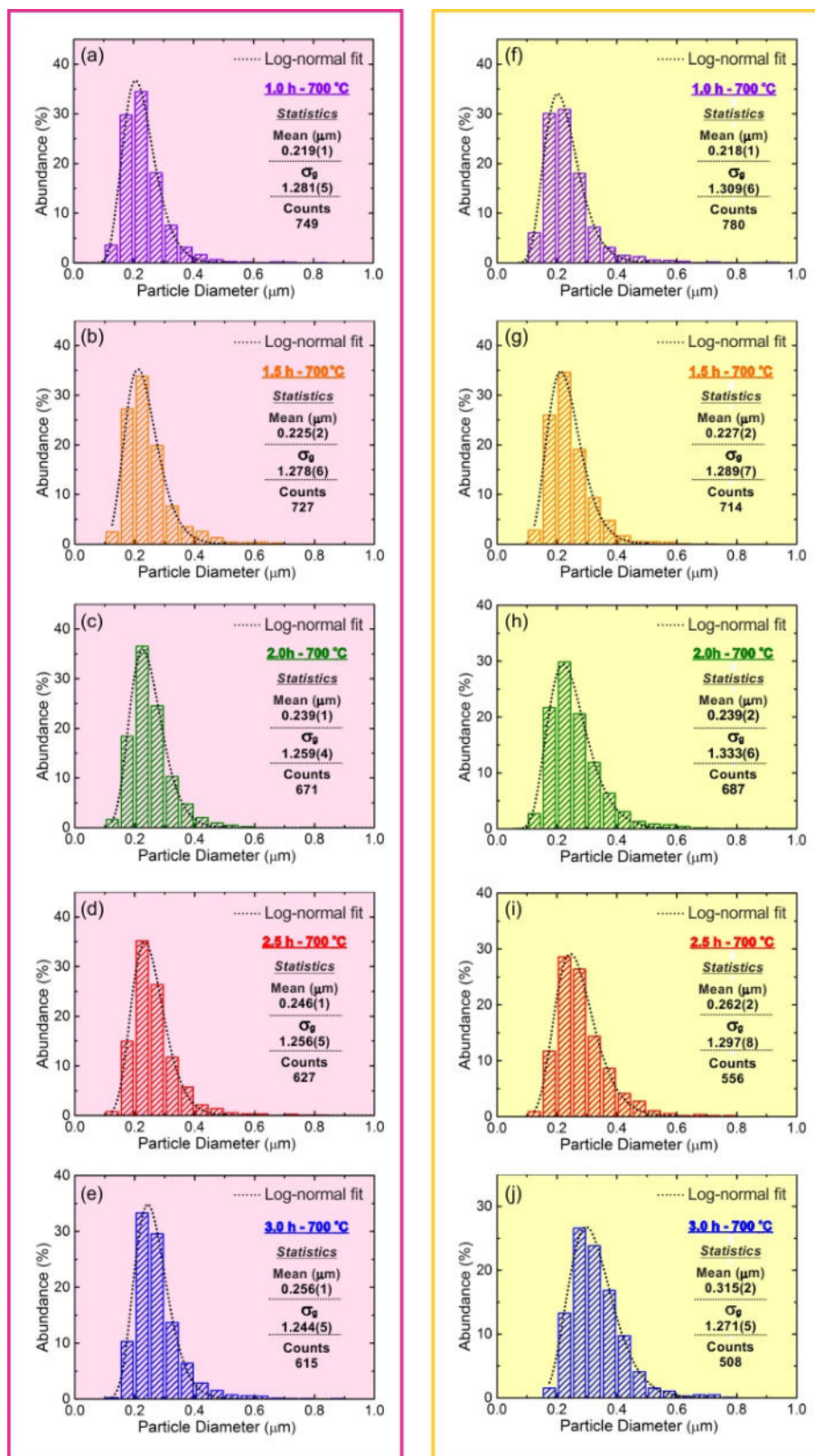


Figure S32 - Particle size distribution histograms of the $m\text{Co:ZnO}$ samples heat treated at $700\text{ }^\circ\text{C}$ in O_2 for (a) 1.0 h, (b) 1.5 h, (c) 2.0 h, (d) 2.5 h, (e) 3.0 h, and in Ar for (f) 1.0 h, (g) 1.5 h, (h) 2.0 h, (i) 2.5 h, and (j) 3.0 h. The line in the panels correspond to the log-normal fit.

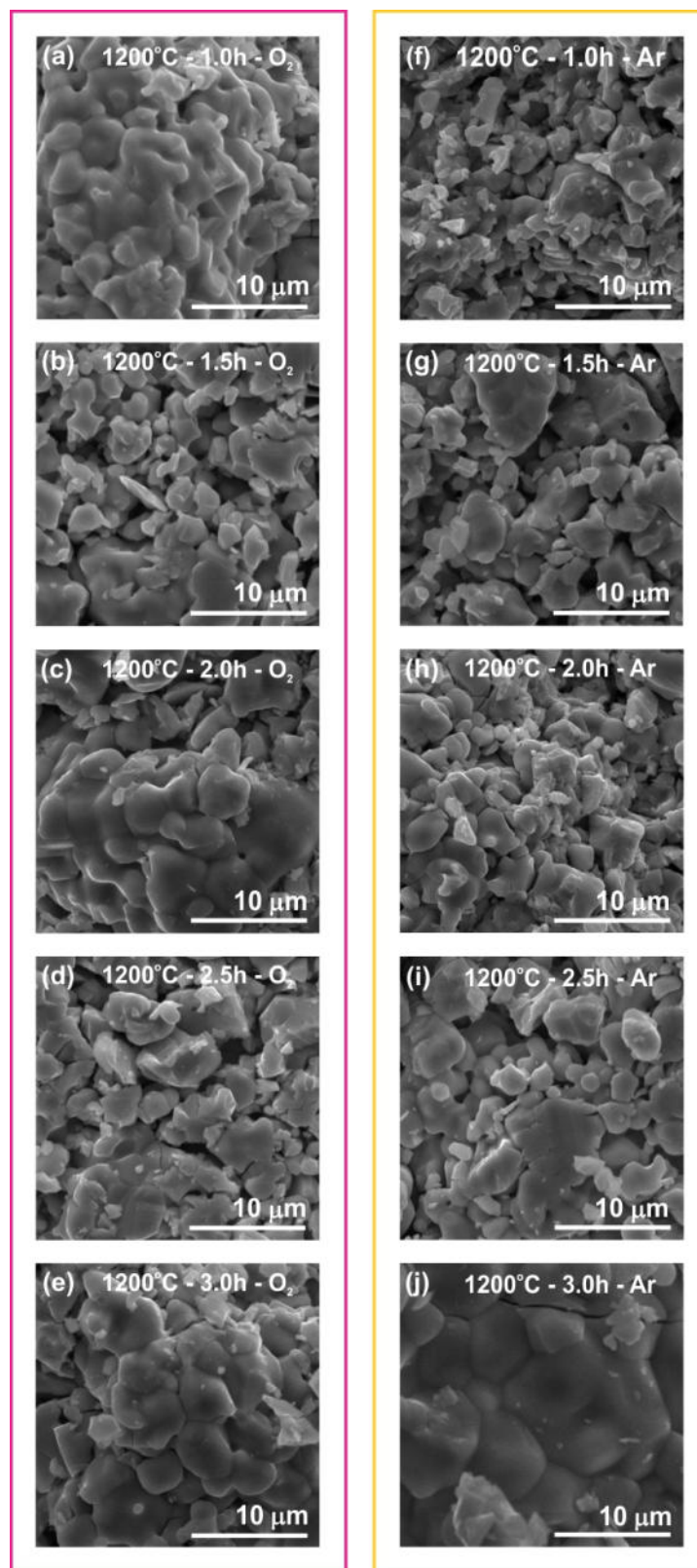


Figure S33 - Representative images by scanning electron microscopy of the surfaces of *mCo:ZnO* samples heat treated at 1200 °C in O₂ for (a) 1.0 h , (b) 1.5 h, (c) 2.0 h, (d) 2.5 h, (e) 3.0 h, and in Ar for (f) 1.0 h, (g) 1.5 h, (h) 2.0 h, (i) 2.5 h, and (j) 3.0 h.

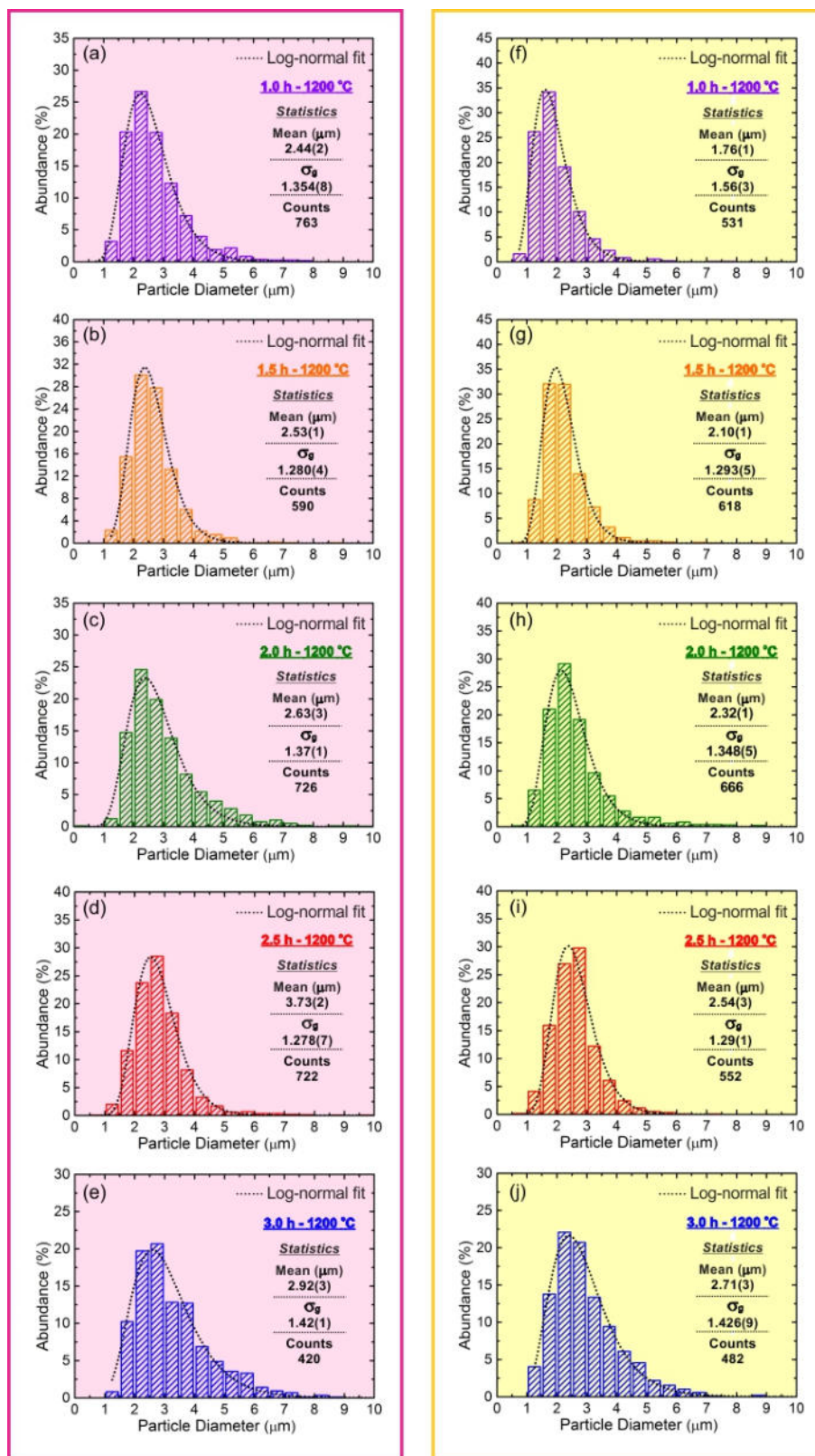


Figure S34 - Particle size distribution histograms of the $m\text{Co:ZnO}$ samples heat treated at $1200\text{ }^\circ\text{C}$ in O_2 for (a) 1.0 h, (b) 1.5 h, (c) 2.0 h, (d) 2.5 h, (e) 3.0 h, and in Ar for (f) 1.0 h, (g) 1.5 h, (h) 2.0 h, (i) 2.5 h, and (j) 3.0 h. The line in the panels correspond to the log-normal fit.

Table S17 - Particle size distribution analyses of the *mCo:ZnO* samples heat treated at 700 °C at different times. L is the mean value of the particle diameter and σ_g is the geometric standard deviation obtained by the log-normal fit of particle size distribution histograms for each sample. N is the total number of counted particles.

		Sample	L (μm)	σ_g	N
<i>mCo:ZnO</i> – 700 °C	Oxygen	1.0h	0.219(1)	1.281(5)	749
		1.5h	0.225(2)	1.278(6)	727
		2.0h	0.239(1)	1.259(4)	671
		2.5h	0.246(1)	1.256(5)	627
		3.0h	0.256(1)	1.244(5)	615
	Argon	1.0h	0.218(1)	1.309(4)	780
		1.5h	0.227(2)	1.289(7)	714
		2.0h	0.239(2)	1.333(6)	687
		2.5h	0.262(2)	1.297(8)	556
		3.0h	0.315(2)	1.271(5)	508

Table S18 - Particle size distribution analyses of the *mCo:ZnO* samples heat treated at 1200 °C at different times. L is the mean value of the particle diameter and σ_g is the geometric standard deviation obtained by the log-normal fit of particle size distribution histograms for each sample. N is the total number of counted particles.

		Sample	L (μm)	σ_g	N
<i>mCo:ZnO</i> – 1200 °C	Oxygen	1.0h	2.44(2)	1.354(8)	763
		1.5h	2.53(1)	1.280(4)	590
		2.0h	2.63(3)	1.37(1)	726
		2.5h	2.73(2)	1.278(7)	722
		3.0h	2.92(3)	1.42(1)	420
	Argon	1.0h	1.76(1)	1.56(3)	531
		1.5h	2.10(1)	1.293(6)	618
		2.0h	2.32(1)	1.348(5)	666
		2.5h	2.54(3)	1.29(1)	552
		3.0h	2.71(3)	1.426(9)	482